

# Boundary-layer height detection with a ceilometer at a coastal site in western Denmark

**Hannesdóttir, Ásta; Peña, Alfredo; Gryning, Sven-Erik; Hansen, Aksel Walle**

*Publication date:*
2013

*Document Version*
Publisher's PDF, also known as Version of record

DTU Wind Energy Master Thesis M-0039

# Boundary-layer height detection with a ceilometer at a coastal site in western Denmark

**Ásta Hannesdóttir**

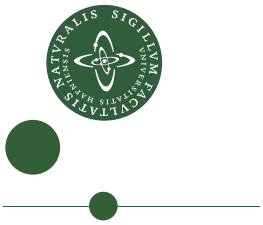

DET NATURVIDENSKABELIGE FAKULTET
KØBENHAVNS UNIVERSITET

DTU Wind Energy
Department of Wind Energy

DTU Wind Energy, Risø Campus,
Technical University of Denmark, Roskilde, Denmark

June 2013

**Author:** Ásta Hannesdóttir
**Title:** Boundary-layer height detection with a ceilometer at a coastal site in western Denmark
**Department:** Niels Bohr Institute and DTU Wind Energy
**Supervisors:** Alfredo Peña, DTU Wind Energy, Risø
Sven-Erik Gryning, DTU Wind Energy, Risø
Aksel Walløe Hansen, University of Copenhagen

**DTU Wind Energy Master Thesis M-0039**
**June 14, 2013**

**Abstract**

One year of data from ceilometer measurements is used to estimate the atmospheric boundary-layer height at the coastal site Høvsøre in western Denmark. The atmospheric boundary-layer height is a fundamental parameter for the evaluation of the wind speed profile, and an essential parameter in atmospheric transport- and dispersion models. A new method of filtering clouds from the ceilometer data is presented. This allows for the inclusion of more than half of the data in the subsequent analysis, as the presence of clouds would otherwise complicate the boundary-layer height estimations. The boundary-layer height is estimated with four different detection methods implemented in an automated detection algorithm. Two of the detection methods used have been modified and are shown to improve the detections under certain circumstances.
Comparisons of boundary-layer height estimates from ceilometer data are made with those from turbulence measurements of a wind lidar and the two methods are in good agreement. It is found that detecting the boundary-layer height from turbulence kinetic energy considerations with the wind lidar is not recommendable for detecting the boundary-layer height during the presence of clouds.
The boundary-layer height estimates are then used to analyse the daily evolution of the boundary layer and to perform monthly and annual frequency distributions of the boundary-layer height. For westerly winds bi-modal distributions are often found, which may be separated by different criteria, while for easterly winds it is seldom possible. The ceilometer data shows potential to be used to perform extensive studies of the boundary layer.

**Pages:** 76
**Tables:** 14
**Figures:** 56
**References:** 47

Technical University of Denmark
Frederiksborgvej 399
4000 Roskilde
Denmark
Tel. +4546775024
bcar@dtu.dk
www.vindenergi.dk

# Contents

# 1 Introduction

The study of our Earth and its atmosphere has led to an understanding that the atmosphere is far from homogeneous, but instead complex and dynamical. The atmospheric boundary layer (ABL) may be defined as the lowest part of the troposphere, where the atmospheric flow is directly influenced by the surface, and responds to changes in the surface forcings within an hour or less Stull (1988). It is an important factor in understanding the lowest part of the atmosphere, and in many different branches of atmospheric research it is used for modelling and experimental considerations. Similarly the height of the ABL, called the boundary-layer height (BLH) separates the turbulent ABL from the free atmosphere (FA) above, and is an essential parameter in defining the ABL. As transport of many quantities such as pollutants, energy, water vapor and aerosols is governed by the dynamics of wind, the BLH plays an important role in both theoretical and numerical meteorological studies, e.g.

- When working with wind energy and the placement of wind turbines, wind profile models are applied, where the BLH is an important parameter of the vertical wind speed profile (Peña et al., 2010).
- Pollution dispersion models. The BLH is a necessary parameter in models simulating turbulent diffusion and transport of pollutants in the atmosphere (Seibert et al., 1998).
- Improvement of mesoscale numerical weather prediction models to predict the BLH at a regional scale (Gryning and Batchvarova, 2002).

Despite the importance of the BLH, it does not have an exact definition, or straightforward method of measurement. It is a parameter hard to define, and cannot always be inferred from a simple equation, especially not in convective conditions (Batchvarova and Gryning, 1991). Synoptic weather, vertical wind shear and stability conditions at the surface all influence the value of the BLH, which may vary significantly in time and space.

Also, as the BLH is often found in the range of hundreds of meters to kilometers, conventional instruments such as radio sondes and masts often lack either the temporal or spatial resolution to provide sufficient data for determining the BLH satisfactorily.

Remote sensors such as lidar are therefore a valuable tool in measuring the BLH. Even so, a remote sensor cannot measure all meteorological conditions. Therefore, when studying the atmospheric BLH, it may be advantageous to include different methods and approaches for a complete picture of the key atmospheric processes.

The method for BLH detection in this thesis is primarily by use of a ceilometer, which will be presented in detail in section 3. A major advantage of using remote sensors such as a ceilometer, is that it measures continuously and over a large vertical range. In contrast to radio sondes which are limited by the rate of release and masts being limited by their height.

In this study a new BLH detection method is described and a new efficient way of handling complications arising in the presence of clouds is presented and tested. For the first time a detailed analysis of frequency distributions of BLH estimates is performed on data from an entire year of measurements at the measuring site Høvsøre. Further, the BLH and its relation to specific conditions of wind, temperature and season is investigated.

## 1.1 Thesis contents

The content of this thesis is as follows. In Section 2 the relevant theoretical background of boundary-layer studies is presented. Section 3 describes the measuring site and the instrumentation used for the observations in this thesis. Different methods of BLH detection are presented in Section 4. In this section is also introduced two new approaches in data processing. The first is an addition to one of the existing methods of BLH detection. The second is a simple method of filtering clouds from the ceilometer data. In Section 5 the results of the investigations are presented, and a discussion of these is given in Section 6. A brief summary of the main conclusions is given in Section 7 along with possible outlooks.

# 2 Theory

## 2.1 Introduction to the atmospheric boundary layer

One of the most important features of the ABL is the continuous turbulence in the whole region, which is mostly produced by vertical wind shear and buoyancy. Turbulence mixes quantities like humidity, temperature and aerosols in the ABL, transmitting them from the surface through the ABL to the rest of the atmosphere.

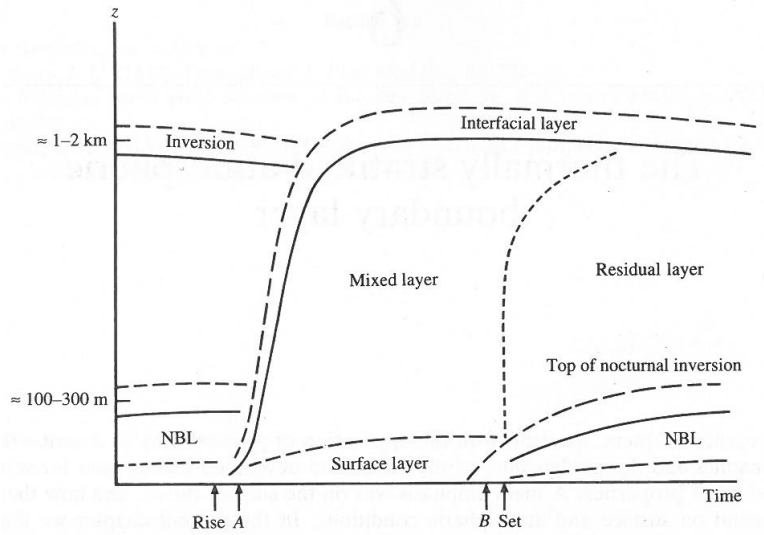


*Figure 1*: Vertical cross section of the ideal ABL structure over land during summer in cloud free conditions. NBL is the nocturnal boundary layer. Figure from Garratt (1992).

The daily evolution of the ABL over land on a clear day in a high pressure region may be seen in Figure 1. The structure of the ABL turbulence is strongly influenced by the surface heating and cooling. The surface layer is seen in the figure as the lowest part of the ABL, its height is approximately 10% of the ABL height. In the surface layer the mean fluxes of momentum, heat and moisture are near constant. The vertical wind gradient is large and the wind speed in the surface layer may be expressed with a logarithmic wind profile under neutral atmospheric conditions[1] (Larsen, 2009; Stull, 1988).

In the morning shortly after sunrise, the convective ABL starts to form (indicated by marker A in Figure 1). The sun heats the surface leading to thermal instability and convection in the surface layer. Above the convective surface layer the mixed layer (ML) is formed. The ML is dominated by convective motion and buoyant turbulence generation including large turbulent eddies. Mean vertical profiles of potential temperature, humidity and horizontal wind are nearly constant within the ML as seen in Figure 2(a). Potential temperature is defined as the temperature an air parcel would have if it were brought adiabatically to a reference pressure (usually 1000 mb). Aerosols that often originate from the surface get mixed through the convective ABL as well. At the top of the ML is a strong capping inversion called the interfacial layer (Wyngaard, 2010; Garratt, 1992) or the entrainment zone (Gryning

[1] i.e. when the heat flux is negligible

and Batchvarova, 1994; Stull, 1988). This capping inversion prevents turbulent motion from beneath the interfacial layer to penetrate far into the free atmosphere.

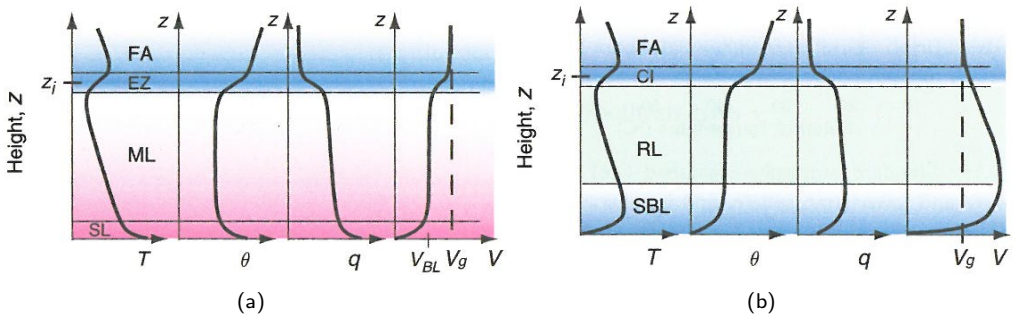


*Figure 2*: Typical vertical profiles of temperature ($T$), potential temperature ($\theta$), specific humidity ($q$) and wind speed ($V$) during daytime (a) and nighttime (b). Abbreviations: free atmosphere (FA), entrainment zone (EZ), mixed layer (ML), surface layer (SL), capping inversion (CI), residual layer (RL), stable boundary layer (SBL), geostrophic wind speed $V_g$. Figure from Stull (2006).

In the evening right before sunset, the stable boundary layer (SBL)[2] starts to form (indicated by marker B in Figure 1), when the surface cools down as a result of radiative cooling. The SBL may also form when warm air is advected over a cooler surface. Turbulence is much weaker than compared with turbulence in the convective ABL and turbulent eddies are smaller. Turbulence is mechanically generated by wind shear and may result in a well mixed stable layer. However stability tends to dampen turbulence generation, and the strength of the turbulence depends on the specific conditions. Above the SBL is the residual layer, where turbulence is decaying and residual heat, moisture and aerosols that were mixed during the afternoon are still present. In Figure 2(b) a sharp increase in the potential temperature is seen directly above the surface, reaching constant values towards the top of the SBL. This indicates that stability is highest near the surface, gradually decreasing towards neutral conditions at the top of the SBL. Winds may increase with height in the SBL, becoming supergeostrophic at the top of the SBL. This is often referred to as a nocturnal jet.

## 2.2 Entrainment

Turbulent entrainment is a process that mixes warm (in a potential temperature sense) and dry air from the FA into the ML. Warm thermals from the surface rise through the ML during free convection and gain momentum. As the thermals reach the free atmosphere they penetrate a short distance due to their momentum. Then they become negatively buoyant in the warm air and sink back to the ML. While these thermals overshoot in the inversion layer, warm quasi-nonturbulent air from the free atmosphere is pushed down in to the ML. This air mixes with the turbulent ML air and the result is mixed-layer growth and entrainment of less turbulent free atmospheric air into the ML (Stull, 1988).

The instantaneous top of the ML is quite sharp and has a varying height in space. Averaging in time, space or an ensemble produces a much thicker interfacial layer as seen in Figure 2(a). The interfacial layer is often defined with horizontal or temporal averaging and the depth of the layer is often 10–30% of the whole CBL depth, but may be much thicker especially in the morning. What characterizes the interfacial layer is a strong positive temperature lapse rate, often significant vertical wind shear, and sharp decreases in aerosol content and specific humidity (Seibert et al., 1998).

[2] often called the nocturnal boundary layer

## 2.3 Flow and scales

There is a rough scale of proportionality between time and spatial scales for atmospheric flow processes, i.e. large scale atmospheric motions are associated with large time scales and small scale motions, like turbulence, are associated with small time scales (Larsen, 2009). Large weather systems with spatial scales of about 1000 km may last for weeks. Microscale or boundary-layer meteorology is the study of atmospheric phenomena with time scales less than an hour and spatial scales smaller than 3 km (Stull, 1988).

Turbulence in the ABL may be imagined as swirling motions of localized vorticity, called eddies. The largest eddies, produced by convective motion, may have a spatial scale as the depth of the ABL. Aside from thermals of rising (or sinking) air, wind shear continuously produces eddies. These large eddies, superimposed on the mean flow, interact with the mean shear and other eddies producing new smaller eddies, that then cascade to even smaller eddies, and so on. The smallest eddies are only a few millimetres in size and will eventually transform into heat by the molecular friction in the air (Larsen, 2009). This mechanism is commonly referred to as the energy cascade.

The turbulent wind flow in the ABL is often described by a mean flow and perturbation flow. Turbulence causes wind measurements to show a fluctuating part, regardless of the time resolution of the measurements. To separate the wind in a mean and a turbulent part a time average has to be performed. This time averaging may span an interval on the order of minutes to an hour, the exact value depending on the specific quantity to be recorded. The turbulent part of the horizontal wind may be found by subtracting the mean wind from the instantaneous wind

$$u' = U - \overline{U} \tag{1}$$

where $u'$ is the turbulent wind component, $U$ is the instantaneous wind component and $\overline{U}$ is the mean wind component. The mean and turbulent parts of all other atmospheric variables may be found in the same manner.

By definition, the turbulent part of the wind field will always average to zero. A common measure of the turbulent part and the dispersion of data about the mean is the unbiased variance,

$$\sigma^2{}_u = \frac{1}{N-1}\sum_{i=1}^{N}(U_i - \bar{U})^2 = \overline{u'^2}. \tag{2}$$

Here $\sigma^2{}_u$ is the unbiased variance of the wind velocity. The summation is over all N wind velocity measurements $u_i$ in the time averaging interval.

## 2.4 Turbulence kinetic energy

If the three cartesian wind components, $U, V$ and $W$ are known, it is possible to calculate the total kinetic energy per unit mass of the flow field, $\frac{1}{2}(U^2 + V^2 + W^2)$. When a time average is made the kinetic energy can be separated into a mean and a turbulent part, where the turbulent part is:

$$\bar{e} = \frac{1}{2}(\overline{u'^2} + \overline{v'^2} + \overline{w'^2}). \tag{3}$$

Here $u'$, $v'$ and $w'$ represent the perturbation wind components, and $\bar{e}$ is the mean turbulence kinetic energy (TKE). The physical processes that produce and dissipate turbulence in the ABL may be investigated by looking at the TKE budget equation. When assuming horizontal homogeneity, aligning the coordinate system parallel with the mean horizontal wind and neglecting subsidence a simplified version of the TKE budget equation has the form:

$$\frac{\partial \bar{e}}{\partial t} = \frac{g}{\overline{\theta}_v}\overline{w'\theta'_v} - \overline{u'w'}\frac{\partial \overline{U}}{\partial z} - \frac{\partial}{\partial z}\overline{w'e} - \frac{1}{\bar{\rho}}\frac{\partial}{\partial z}\overline{w'p'} - \varepsilon \quad (4)$$

where $\theta_v$ is the virtual potential temperature, $g$ is the gravitational constant and $p'$ is the pressure perturbation. The virtual potential temperature, $\theta_v$, is the temperature an moist parcel of air would have, if it was dry and still have the same density. As moist air is less dense than dry air, and therefore more buoyant, the $\theta_v$ of moist air is higher than the potential temperature of the same parcel (the dry air parcel would have to be warmer to have the same density). An explanation for each term in the TKE budget is given as follows:

$\frac{\partial \bar{e}}{\partial t}$ This first term describes the local change in TKE with time.

$\frac{g}{\overline{\theta}_v}\overline{w'\theta'_v}$ The buoyancy production or consumption term, depending on the sign of the heat flux. A positive contribution of this term represents the efficiency of thermals in turbulence generation. This term gives a large contribution to the TKE budget on a sunny day over land, or when cold air is advected over a warm surface. In a positively buoyant cloud there is also a large generation of turbulence. In situations with static stability, there will be consumption of TKE, and convective motion is suppressed. This is typically observed at night over land or at the top of the ML (Stull, 1988).

$\overline{u'w'}\frac{\partial \overline{U}}{\partial z}$ The third term represents interaction between mean wind vertical shear and turbulent momentum flux. This term is most often positive in the ABL as momentum flux tends to have opposite sign of the mean wind shear. The largest contribution to the TKE budget from this term is in the surface layer when winds are strong, as the horizontal wind decreases to zero at the surface, resulting in a high mean vertical wind shear.

$\frac{\partial}{\partial z}\overline{w'e}$ This fourth term is the vertical turbulent flux divergence. This is not a consumption or production term, but represents vertical transport by turbulent eddies.

$\frac{1}{\bar{\rho}}\frac{\partial}{\partial z}\overline{w'p'}$ The fifth term is a pressure correlation term and describes how pressure perturbations, most often caused by gravity or buoyancy waves, shift TKE. This term is generally difficult to measure because of the small size of the pressure perturbations.

$\varepsilon$ The last term is the viscous dissipation rate of TKE. Contributions from this term arise as the smallest eddies transform their energy to heat at a molecular level.

The above mentioned TKE budget equation is somewhat simplified, for example horizontal advection of TKE by the mean wind and all horizontal divergences of the other terms are neglected. However this equation still gives a good summation of what processes generate and consume TKE in the ABL, and how TKE changes with time. The derivation of the TKE budget[3] may be found in Stull (1988).

## 2.5 The Obukhov Length

The Obukhov length is stability parameter that is used as a scaling parameter in the surface layer (Obukhov, 1946).

The Obukhov length may be derived from the TKE budget equation assuming horizontal homogeneity and using Monin-Obukhov similarity hypothesis (Wyngaard, 2010). In the surface layer mean fluxes are assumed near constant, so the vertical turbulent flux divergence and pressure correlation terms may be neglected. Furthermore, assuming steady state, i.e $\partial \bar{\mathrm{e}}/\partial \mathrm{t} = 0$ and that viscous dissipation of TKE may be neglected, leads to a TKE budget as follows

[3]The TKE budget equation may be derived by applying the conservation of momentum with a Boussinesq approximation for the turbulent flow. This is then multiplied by $2u'_i$, and terms are rewritten with rules of calculus. Applying Reynolds averaging and neglecting small terms leads to the prognostic equation for wind velocity variance, which finally is divided by two.

$$\frac{g}{\overline{\theta}_v}\overline{w'\theta'_v} = \overline{u'w'}\frac{\partial\overline{U}}{\partial z}. \tag{5}$$

If the coordinate system is aligned with the mean horizontal wind, $\overline{\mathrm{u'w'}}$ may be replaced by the friction velocity $-\mathrm{u}_*^2$. The von Kármán constant, $k$, is defined to scale the friction velocity in a fully turbulent region near a surface:

$$k = \frac{u_*}{z\partial\overline{U}/\partial z}. \tag{6}$$

The vertical wind shear $\partial\overline{U}/\partial z$ in equation 5 may be replaced with $u_*/kz$ and z expressed as $L$, the Obukhov length:

$$L = -\frac{u_*^3\theta_v}{kg\overline{w'\theta'_v}} \tag{7}$$

where the von Kármán constant has been found experimentally to be approximately $k = 0.4$. The Obukhov length may be understood physically as being the height above the ground where the buoyancy produced turbulence and mechanically produced turbulence are equal. It can be seen in equation (7) that the sign of $L$ depends of the sign of $\overline{w'\theta'_v}$ which again depends on the stability conditions. In unstable conditions the temperature near the surface decreases with height and heat will be transported upwards by turbulence and $\overline{w'\theta'_v}$ will therefore be positive. Therefore $L$ is a measure for stability in the surface layer. It is common to calculate the inverse Obukhov length $1/L$. For stable conditions $1/L$ is positive, whereas $1/L$ is negative for unstable conditions and $1/L$ approaches zero for neutral conditions.

## 2.6 The marine boundary layer

As mentioned in Section 1 the measuring site of Høvsøre is placed in a coastal region, less than two kilometers inland from the North Sea. As the wind direction is often westerly, the marine ABL is advected over the coastline at Høvsøre.

There are some important differences between marine ABL and that over land. The air within the surface layer over the sea is generally more humid, compared with that over land (except at nighttime close to the surface), with relative humidity (RH) often exceeding 75%. Because of these high humidities, cloud formation is frequent and extensive over oceanic regions (Stull, 2006).

The diurnal variation in sea-surface temperature is much less than that of the ground, because of the large heat capacity of the oceanic mixed layer. A comparison of the heat capacity of a typical atmospheric mixed layer (1000 m depth) and an oceanic mixed layer (100 m depth) gives the ratio ∼1/350 (Garratt, 1992). The relatively slow temperature change of the sea surface leads to a boundary layer with different stability conditions and diurnal cycle than over land. The marine BLH changes relatively slowly, and changes mainly because of advection of different air masses over the sea surface and synoptic and mesoscale vertical processes (Stull, 1988). As the marine air mass is advected over the coastline, the change in surface conditions affects the land air mass. This affected air mass is known as the internal boundary layer, with a height that is dependent on the downwind distance from the coast. This distance is called fetch, and in the case of Høvsøre is ∼ 1.7 km. When there is a temperature difference between the sea surface and land surface, the modified air is called a thermal internal boundary layer (TIBL). The height of the TIBL has been shown to be proportional to the square root of the fetch, i.e.

$$h_b = a\sqrt{x} \tag{8}$$

where $h_b$ is the height of the TIBL, $x$ is the fetch, measured in meters, and $a$ is a constant of proportionality, found to be in the range 2-5. In the case of Høvsøre, this gives an expected height of the TIBL of ∼ 80-200 m. It can take up to 50 km for the internal boundary layer to reach a full depth (Garratt, 1992).

## 2.7 Boundary-layer clouds

The presence of clouds greatly influences boundary-layer dynamics and the surface weather. Many cloud types are an essential feature of the ABL and cannot be separated from boundary-layer studies. These clouds are mainly the low clouds, limited in their vertical extent. They may be seen in Figure 3 as cumulus, stratocumulus, stratus and fog. Clouds that have large vertical extent cannot be treated as an intrinsic part of the ABL.

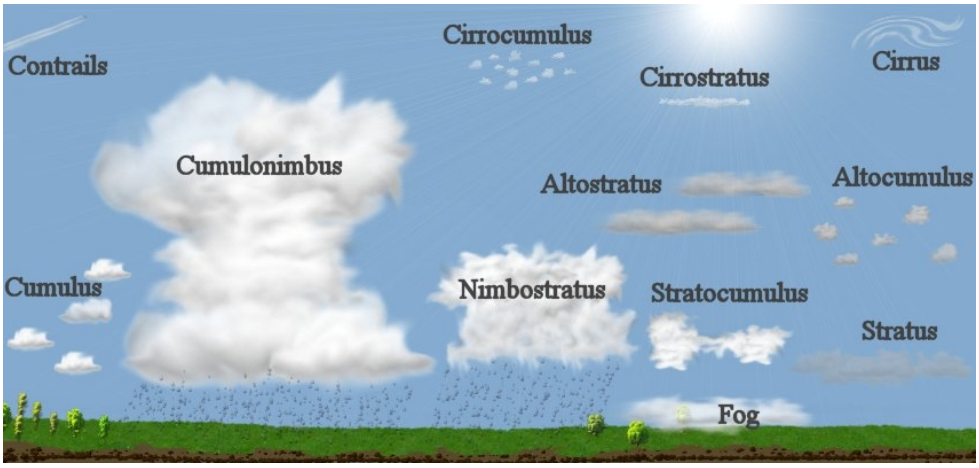


*Figure 3*: Main cloud types. Figure from Klaus (2005).

Clouds are often ignored or omitted in boundary-layer studies, because they complicate the boundary-layer dynamics. Clouds change the distribution of the incoming short wave radiation and outgoing long wave radiation and phase changes of water in a cloud causes heat release or consumption. In the absence of clouds, changes of turbulent structure and mean variables are mainly controlled by surface fluxes and large scale conditions. In the presence of clouds surface fluxes may be important, but radiative fluxes relating to the cloud have a large impact on the turbulence production and evolution in the ABL (Garratt, 1992).

Clouds form at the top of the ML. Air parcels that overshoot by thermals into the interfacial layer are adiabatically cooled. As an air parcel cools the water vapour starts to condensate at its lifting condensation level and latent heat is released. If the parcel has enough momentum and overshoots high enough the potential temperature, $\theta$ of the parcel gets higher than that of the environment. Then the parcel reaches the level of free convection and is positively buoyant. The parcel continues to rise until it is again cooler than the environment. In this way air is drawn up from the ML to the cloud layer. The lifetime of a cloud is controlled by its dynamics and interactions with its environment. When studying clouds it is often convenient to use the equivalent potential temperature $\theta_e$, instead of the virtual potential temperature $\theta_v$. This is because $\theta_e$ is a conserved variable within the cloud, while $\theta_v$ is not. The equivalent potential temperature is the temperature a parcel of air would have if all water vapour within it would condense.

Fog can form at the bottom of a stable boundary layer. At night the air close to the ground cools due to radiative cooling. It can cool down below the dew point temperature and reach saturation. A fog layer that does not develop further, where only the air close to the ground is saturated, is called mist and is usually only 1–5 m thick. The mist can develop into fog if radiative cooling continues and becomes larger at the top of the fog layer than at the surface. This deepens the fog layer and thermals generated by the cooling at the top of the fog layer sink and mix the fog layer. Warm and humid air flowing over a cold surface may also result in fog formation.

**The cloud topped boundary layer**

When a cloud layer and a ML are fully coupled, the idealized profiles of $\theta_e$, $\theta_v$ and the total water mixing ratio, q, will look like in Figure 4. The total water mixing ratio and the equivalent potential temperature are constant with height. This indicates that when a cloud layer and the ML are turbulently fully coupled, the cloud is an essential part of the ML. The $\theta_v$ profile follows the moist adiabatic in the cloud layer.

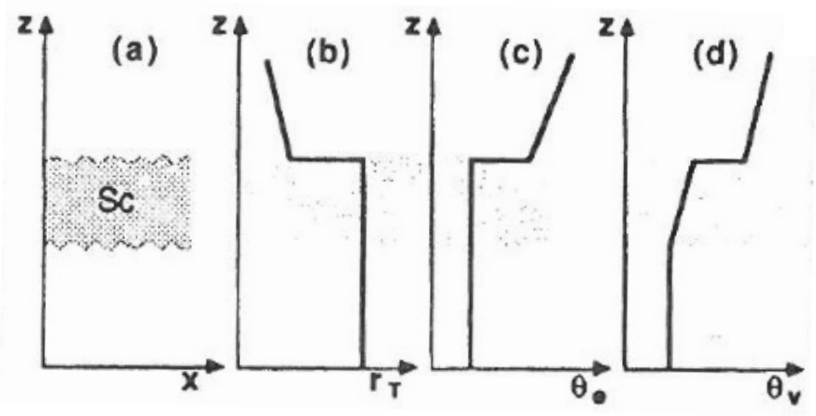


*Figure 4*: Idealized profiles of mean variables within a stratocumulus topped ML. (a) Cloud location, (b) total water mixing ratio, (c) equivalent potential temperature, (d) virtual potential temperature. Adapted from Stull (1988).

The air above the cloud is warmer (in a potential temperature sense) and drier than the cloud air. When dry warm air from above entrains the cloud some liquid water from cloud droplets evaporates and evaporative cooling occurs. The air becomes negatively buoyant and produces TKE that increases mixing and more entrainment in the cloud. This process usually causes the ML to become drier and warmer and raises the height of the cloud layer. If a large amount of dry air entrains the cloud it may cause it to break up and evaporate (Stull, 1988). Measurements show that cloud air is a mixture of air originating at the cloud top and the cloud base (Betts, 1985).

The cloud top entrainment generates TKE within the cloud. Turbulent mixing is generally high within clouds and several other processes contribute to the TKE generation: Free convection from the surface, shear generated turbulence, cloud layer shear, cloud top radiative cooling and cloud base radiative heating.

In the case of a cloud topped boundary layer (CTBL), different ways of defining the BLH exist. First, the BLH may correspond to the cloud top. In this case the CTBL is defined as a layer that is directly coupled to the surface by turbulent transfer, including fair-weather cumulus and stratocumulus clouds. Here a noticeable inversion exists at the cloud top, but the CTBL tends not to be well mixed above the cloud base (Stull, 1988; Garratt, 1992). Second, the BLH may be defined at or near the cloud base. With this definition the BLH corresponds well to the top of a relatively well-mixed layer and to a height where turbulent fluxes of heat and momentum become negligible (Garratt, 1992). A third definition of the BLH is proposed by Grimsdell and Angevine (1998), which states that when the cloud cover is roughly 50% or less and the cloud layer is not deep compared with the ABL underneath, the cloud layer may be considered to define the interfacial layer. The corresponding BLH may then be defined as approximately in the middle of the cloud layer.

## 2.8 Statistical methods

A few statistical methods used for the data analysis are presented here. The unbiased variance has already been introduced in Section 2.3 in Equation 2. The standard deviation is given by

the square root of the variance.

### Root mean square deviation

The root mean square deviation (RMSD) or root mean square error (RMSE) is a measure of differences between two measurements of the same parameter. It may also compare model output with measurements. The RMSD is defined by:

$$RMSD = \sqrt{\frac{\sum_{i=1}^{N}(x_i - y_i)^2}{N}} \tag{9}$$

where $x_i$ is the model output of index $i$ and $y_i$ is the observation of index $i$. The number of model output and observation pairs is given by $N$. It is clearly seen that if there is a lack of compatibility between model outputs and observations the RMSD will be large (Wilks, 2011).

### Correlation

When investigating the relation between two data series, $x$ and $y$, it is convenient to calculate the correlation coefficient, $R$, given as

$$R = \frac{\sum_{i=1}^{N}(x_i - \bar{x})(y_i - \bar{y})}{\sqrt{\sum_{i=1}^{N}(x_i - \bar{x})^2 \sum_{i=1}^{N}(y_i - \bar{y})^2}} \tag{10}$$

where $\bar{x}$ and $\bar{y}$ are the sample means of $x$ and $y$. When determining if the correlation is significant on a given level, the number of elements in the data series, $N$, must be included. The values of $R$ required for two confidence levels are shown in table 1, for different values of $N$, that are relevant for this thesis. This confidence level gives the probability that the correlation is not by chance, given that the datasets are independent (Kreyszig, 1999).

| Confidence level | $N = 125$ | $N = 135$ | $N = 145$ |
|---|---|---|---|
| 99% | $R = 0.21$ | $R = 0.21$ | $R = 0.20$ |
| 99.9% | $R = 0.28$ | $R = 0.27$ | $R = 0.26$ |

*Table 1*: Confidence levels for different values of $N$ .

### Linear regression

Linear regression is a statistical procedure, modelling the relationship between two variables (here $x$ and $y$), summarized by a single straight line. The most common type of linear regression is a least-squares fit, where the regression procedure minimizes the squared differences between a set of measurements and their predicted values. Given a dataset of $N$ individual ($x_i$,$y_i$) pairs, the regression produces the constants $a$ and $b$ in the straight line $\hat{y} = ax + b$ by minimizing the sum of $(y_i - \hat{y}(x_i))^2$. When solving the straight line fit for the linear regression, the slope of the straight line, $a$, is given by

$$a = \frac{\sum_{i=1}^{N}(x_i - \bar{x})(y_i - \bar{y})}{\sum_{i=1}^{N}(x_i - \bar{x})^2} \tag{11}$$

and $b$ is subsequently found by

$$b = \bar{y} - a\bar{x} \tag{12}$$

where $\bar{x}$ and $\bar{y}$ are the sample means of $x$ and $y$.

### Gamma distribution

The Gamma distribution is a continuous probability density function of two free parameters $\alpha$ and $s$. The general form of a Gamma distributed random variable, $x$, is

$$f(x;\alpha,s) = x^{\alpha-1} \cdot \frac{e^{-x/s}}{s^{\alpha} \cdot \Gamma(\alpha)} \tag{13}$$

where $\alpha$ is the shape parameter, $s$ is the scale parameter and $\Gamma$ is the Gamma function. The mean of the Gamma distribution is given by $\alpha s$ and the mean is $\sqrt{\alpha}s$ (Liu and Liang, 2010).

# 3 Site and measurements

In this section the site location is presented and some of the instruments used there. The theoretical background of the ceilometer, wind lidar and sonic anemometer measurements is explained, along with a presentation of the available data from the site database.

## 3.1 Høvsøre

Høvsøre is a farm area located at the westcoast of Jutland, seen in Figure 5(a). Here, a ceilometer has operated almost continuously since january 2007. The location of Høvsøre was chosen in 2002 to be a national test facility for large wind turbines, seen in Figure 5(b). Due to the location and the type of terrain, wind speeds are very high[4] and general wind patterns are very well understood, providing excellent conditions for the testing (Høvsøre infofolder, 2013).

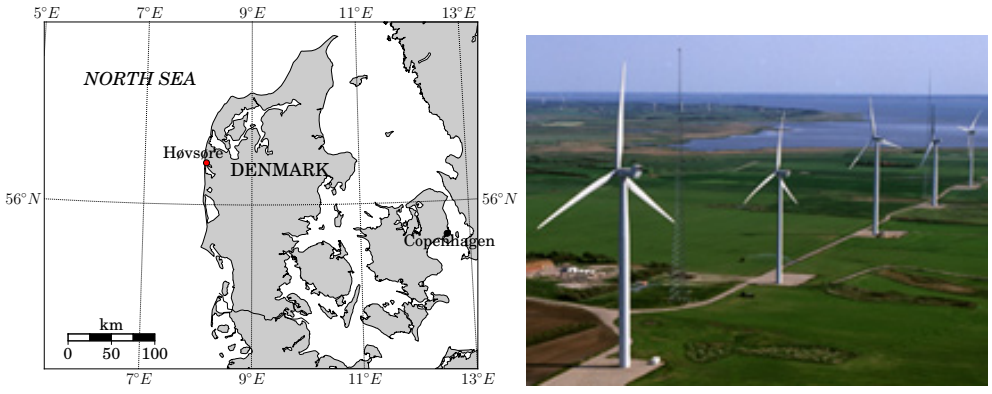


(a) (b)

*Figure 5*: (a): Map of Jutland, with Høvsøre indicated (map made by Rogier Floors). (b): View of Høvsøre test station, with operational wind turbines. Picture from Høvsøre infofolder (2013).

## 3.2 The ceilometer

The ceilometer is a single lens LIDAR (Light Detection And Ranging) device, which is primarily used to detect cloud base and vertical visibility. It transmits short pulses of light in the near-vertical direction. The light is scattered by particles in the air, aerosols, cloud droplets and precipitation. The returned light is then collected in a receiver inside the ceilometer (Vaisala User's Guide, 2004). The height $h$ from which the returned signal comes from may be estimated as

$$h = \frac{ct}{2} \tag{14}$$

where $c$ is the speed of light and $t$ the time delay. As the speed of light is taken as a constant, the height may be calculated directly from the time delay. The signal strength as a

[4] the annual mean wind speed is ∼9.3 m/s at 80 m

function of height, $P(z)$ provides information on the backscatter profile of the atmosphere. It is measured by the instrument and is related to the emitted signal and the characteristics of the propagating medium through the lidar equation:

$$P(z) = P_0 \Delta t \frac{c}{2z^2} A \beta(z) e^{-2\int_0^z \sigma(z')dz'} \tag{15}$$

where $P_0$ is the average power of the pulse [W], $\Delta$t is the duration of the emitted laser pulse [s], c is the speed of light [m/s], A is the receiver area [m$^2$], $\beta(z)$ is the volume backscatter coefficient at distance z [1/(srad m)], $\sigma$(z') is the extinction (attenuation) coefficient at various distances z' [1/m] and $e^{-2\int_0^z \sigma(z')dz'}$ is the atmospheric transmittance. When there is no attenuation, in a clear atmosphere, the last term equals 1.

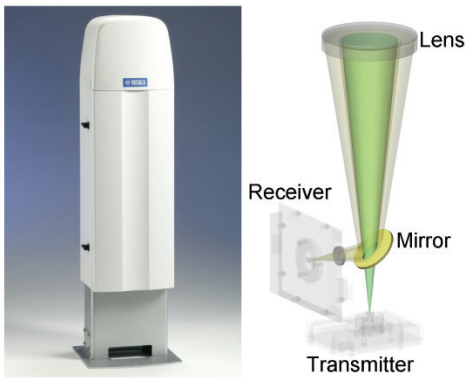


*Figure 6*: The single lensed optics of the ceilometer CL31 (Münkel, 2006)

The laser pulse signal is reduced by absorption (extinction coefficient) and scattering (backscatter coefficient), so when solving the lidar equation, there are two unknown quantities: $\beta(z)$ and $\sigma(z')$. The simplifying assumption is made that there is a linear relationship between extinction and backscatter.

$$\beta(z) = \kappa\sigma(z) \tag{16}$$

where $\kappa$ is called the lidar ratio and is assumed constant for a given height (Vaisala User's Guide, 2004). It is then possible to obtain the vertical profiles of backscatter and extinction coefficients with the use of an inversion algorithm. It is not possible to know the exact ratio $\beta(z)/\sigma(z)$ from the received signal, but the precise functional description is not needed to obtain useful results as stated by Klett (1985).

Most lidars have the transmitter and receiver placed beside each other, which means that there is a zenith angle between emitted and received light in the near range. This produces an error in the signals that may be corrected with an overlap function (Leosphere User Manual, 2009). The ceilometer on the other hand is a single lens optical devise. Figure 6 shows the Vaisala Ceilometer CL31 and a schematic drawing of its optical concept. An inclined mirror with a hole in the center divides the lens into two areas. The inner area transmits the laser beam, while the outer area receives and focuses the backscattered light. This optical arrangement provides a full overlap of the whole measuring range, but has the disadvantage that emitted light is partially reflected by the lens directly to the receiver, when measuring signals from the near range (Münkel, 2006).

## 3.3 The wind LIDAR

The main difference between the ceilometer and the wind lidar is that the wind lidar relies on measurements of the Doppler shift of the backscattered laser pulse (Leosphere, 2008; Cariou

and Boquet, 2011). Due to the wind field, the aerosols in the atmosphere are in motion. When the light emitted by a laser hits the moving aerosol this results in a frequency shift of the light, as illustrated in Figure 7. The moving particle scatters the pulse back and the received frequency, $f$, is calculated as:

$$f = f_0 + \Delta f \simeq f_0(1 + 2V/c) \tag{17}$$

where $f_0$ is the emitted frequency, $\Delta f$ is the frequency shift, $V$ the wind velocity and $c$ the speed of light.

The frequency shift of the returned light is proportional to the radial component of the wind, i.e the projection of the wind velocity vector on the line-of-sight.

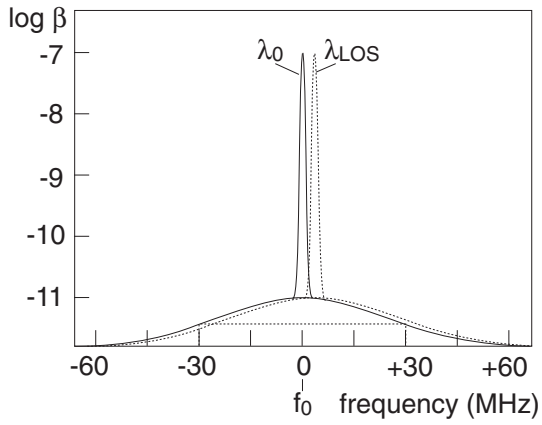


*Figure 7*: Schematic representation of the original (solid) and wind-shifted (dotted) frequency distributions. If there are aerosols present, a narrow spike is superimposed onto the broad molecular peak. The return-signal frequency is shifted here toward higher values, indicating that the wind is moving toward the lidar. At 10.59 $\mu m$ wavelength, the 3-MHz shift corresponds to a wind speed of $\sim$20 m/s (Werner, 2005).

The return signal of the laser pulse is processed with heterodyne principle. In heterodyne detection the return signal is mixed with a reference signal of a local oscillator in the device, with a frequency $f_{LO}$. The mixed signal contains two new frequencies, one is the sum $f_{LO} + (f_0 + \Delta f)$, and the other the difference $f_{LO} - (f_0 + \Delta f)$, known as the heterodyne- or beat frequency. If the frequencies of the two signals are close to each other the beat signal may be determined. The detector of the device measures the current, $i$, of the beat frequency signal only:

$$i = \rho\sqrt{2P_{LO}P(z,\lambda)}\cos[2\pi(f_{LO} - (f_0 + \Delta f))] \tag{18}$$

where $\rho$ is the detector sensitivity [A/W], $P_{LO}$ is the power of the local oscillator laser [W], $f_{LO}$ is the frequency of the local oscillator laser [Hz], $P(z,\lambda)$ is the power of the backscattered signal [W] and $f_0 + \Delta f$ the frequency of the backscattered signal [Hz].

It is important to determine the difference between the transmitted frequency and the local oscillator frequency with great accuracy. This difference is kept as stable as possible (Werner, 2005).

To provide information of all three wind vector components $U, V$ and $W$, the lidar may scan in three or four directions. If the lines of sight are in the North, South, East and West directions, the measured radial velocities $Vr_i$ are:

$$\begin{aligned} Vr_N &= U\sin\phi + W\cos\phi \\ Vr_S &= -U\sin\phi + W\cos\phi \\ Vr_E &= V\sin\phi + W\cos\phi \\ Vr_W &= -V\sin\phi + W\cos\phi \end{aligned} \tag{19}$$

where $\phi$ is the off-zenith-angle, or cone-angle. Subscripts, N,S,E,W indicate the four different directions. The retrieved wind velocity components are then:

$$U = \frac{Vr_N - Vr_S}{2\sin\phi} \tag{20a}$$

$$V = \frac{Vr_E - Vr_W}{2\sin\phi} \tag{20b}$$

$$W = \frac{Vr_N + Vr_S + Vr_E + Vr_W}{4\cos\phi} \tag{20c}$$

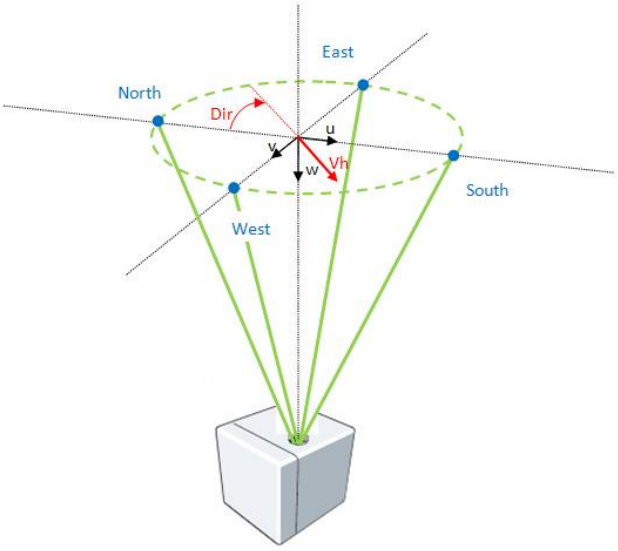


*Figure 8*: Schematic of the windcube scanning technique for retrieving the wind velocity components (Cariou and Boquet, 2011).

In Figure 8 is illustrated the principle of the lidar windcube used for estimating the wind velocity components, $U$,$V$ and $W$. The reconstruction of these wind velocity components is based on the assumption of horizontal homogeneity. This assumption is valid on offshore and on flat terrain. The off-zenith-angle $\phi$ is a trade-off between wind homogeneity and velocity resolution. Larger values of $\phi$ allow for better projections of the wind vector on each laser pulse, while smaller angles improve wind homogeneity (Cariou and Boquet, 2011).

## 3.4 Sonic anemometer

A sonic anemometer uses short pulses of ultrasonic sound waves to measure wind speed. It has three pairs of sound probes which are used alternately as transmitting and receiving units (transducers). In motionless air the time of flight for all three pulses is equal. A picture of the type of anemometer at the site is seen in Figure 9.

In a wind field the time of flight increases for a single pulse moving upwind, and decreases downwind. If the wind field is parallel to the trajectory of the sonic pulse between one of the probe pairs, the times of flight downwind $t_1$, and upwind $t_2$ are

*Figure 9*: Picture of a METEK USA-1 sonic anemometer. Taken from (Metek, 2013a).

$$t_1 = \frac{s}{v_{sound} + U} \tag{21a}$$

$$t_2 = \frac{s}{v_{sound} - U} \tag{21b}$$

where $v_{sound}$ is the sound velocity, $U$ is the wind velocity and $s$ is the distance between the transducers (Gill-Instruments, 2013). The wind speed and the sound velocity may be calculated from the changes in the time of flight.

$$v_{sound} = \frac{s}{2}\left(\frac{1}{t_1} + \frac{1}{t_2}\right) \tag{22a}$$

$$U = \frac{s}{2}\left(\frac{1}{t_1} - \frac{1}{t_2}\right) \tag{22b}$$

The sound probe pairs are mounted in three different directions to provide a 3-dimensional wind vector. The sound velocity depends on temperature and humidity, and thus the sound velocity corresponds to a measurement of nearly virtual temperature (Metek, 2013b).

## 3.5 Instrumental set-up

Temperature and RH measurements in Høvsøre are made with a Vaisala HUMICAP temperature and humidity probes. Wind measurements are made with RISØ P2546 cup anemometers. Solar radiation is measured with a Kipp & Zonen CMP pyranometer. The Metek USA-1 sonic anemometer measures turbulent fluxes.The instrumentation is placed on a meteorological mast.

The ceilometer at Høvsøre is a Vaisala CL31. This instrument was set to return the total aerosol backscatter coefficient every 10 s with a 20 m vertical resolution, within the range 20–7700 m. The wavelength of the laser is 905 nm, with an energy of 1.2 $\mu$J per pulse. For eye-safety concerns, the laser pulse of the ceilometer is not very powerful and white noise from ambient light will affect the backscattered signal. The influence of noise is reduced by averaging over a large number of pulses. The signal-to-noise ratio will be improved by the square root of the number of pulse repetitions, which is on average 8192 (Münkel et al., 2007).

The wind lidar is a Leosphere WLS70 Windcube. The north beam of the wind lidar in Høvsøre is offset from the geographical North by 50°. The off-zenith-angle is 15° and laser pulse wavelength is 1.5 $\mu m$. The lidar measures from 100 m with 50 m height resolution. It can measure up to 2000 m, assuming aerosols are present. It measures every 10 s and reports

only measurements where carrier to noise ratio (CNR) is above -35 dB. The laser pulse length is 400 ns and pulse energy is 20 $\mu J$. The laser pulse length is relatively long, resulting in a large probe length, $\sim$60 m, that influences the velocity and turbulence measurements (Mann and Peña, 2010). The wind lidar data used for this study is limited to signals where the CNR $\geq$ -22 dB. This cut-off value is based on a comparison of the wind lidar measurements at 100 m with the cup anemometer at 100 m in Høvsøre. The comparison shows that the mean bias increases and the linear correlation decreases with CNR $\leq$ -22 dB (Peña et al., 2013).

## 3.6 The Høvsøre database

The data measured with the instruments in Høvsøre is stored in a database. The database is accessed online with MySQL, which is a open source database management system (MySQL 5.1 Reference Manual, 2013). MySQL is a relational database, i.e. it stores data in separate tables structured and optimized for speed. Users of MySQL may manage the database with a Query Browser or connect directly to a numerical computing environment, in this case Matlab.

In the data base the data is sorted by the different instruments. The data output is in vector form with associated time vectors. Wind speed (m/s) averaged over 10 minutes and direction (0-360°) data is available from cup anemometers at 10, 40, 60, 80, 100 and 116 m. The RH (%) and temperature (°C) data is available at 2 and 100 m. The solar radiation reaching the surface is measured in W/m$^2$. The sonic anemometer measures turbulent fluxes and calculations of the Obukhov length (m). The wind lidar data output contains 10-minute mean wind components U, V, W, in m/s and the standard deviations of these. The total horizontal wind (m/s) and direction (0-360°) is available as well. Furthermore carrier to noise ratio (CNR) data is provided.

The data available from the Høvsøre database are 10-minute average parameters, spanning April 1 2010 (the wind lidar 24 April) to March 31 2011. Backscatter coefficients occasionally show time duplicates in the 10-min averages which show different backscatter coefficient profiles (typically 0-5 a day). Investigations of the duplicates reveal that the first profile is identical to a single 10 s profile in the same time interval, while the second profile is the expected 10 min average. Therefore the first of the time duplicates is removed when working with the data.

# 4 Boundary-layer height detection

Traditionally, BLH is derived from data measured with radiosondes. The radiosonde measurements provide measurements of temperature, dewpoint and pressure through the lower troposphere. From these measurements vertical profiles of potential temperature and water vapour mixing ratio may be attained. The BLH is associated with sharp changes in the vertical profiles and is often identified subjectively from the profiles. Objective BLH detection from radiosonde data exist as well and are described by Seibert et al. (1998). The BLH estimates derived from radiosonde data are limited to the launch time of the radiosondes, which is typically 2–4 times a day.

In this way remote sensing systems have an advantage in BLH estimations, as they provide continuous measurements. Besides lidar measurements, remote sensing is often performed with wind profilers or sodars. The sodar basically may be used to derive the BLH from the backscatter of sound waves. The intensity of the backscatter mainly depends on small-scale temperature inhomogeneities, used to derive the BLH.

The wind profiler is similar to the acoustic sodar, with the main difference being its use of electromagnetic waves instead of sound waves and that it apart from temperature also measures moisture inhomogeneities (Seibert et al., 1998).

As mentioned, the lidar measurements rely on the aerosol concentration in the atmosphere. In the ABL the aerosol concentration is high compared to the free atmosphere above and this contrast is the basis for BLH detection from lidar measurements (Cohn and Angevine, 2000).

It is often seen that the aerosol content is closely related to the temperature profile, and the different methods therefore provide similar BLH estimates. Even so, there may be notable differences in the thermal structure and the aerosol content as mentioned by Emeis et al. (2004). This is seen on clear days, near sunset, when a SBL starts to form near the surface, changing the temperature profile, while the aerosol content in the residual layer is not immediately affected by this formation. The SBL is therefore generally detected later during the nighttime with aerosol measurements. Although most BLH detection methods focus on mixed layer detection, it is also possible to detect the SBL with lidars and ceilometers (Martucci et al., 2007).

When looking at an aerosol backscatter profile under ideal cloud free conditions during daytime, the entrainment zone and the mixed layer may clearly be seen. In these situations the BLH may be identified by visual inspection. However, when the amount of backscatter data is large, this method will be time consuming. In that case an automated BLH detection program will be preferable.

There are numerous ways to detect the BLH from aerosol backscatter data, e.g. wavelet analyses (Davis et al., 1997), variance method (Martucci et al., 2010), the vertical gradient (Schäfer et al., 2004; Emeis et al., 2008), critical threshold (Batchvarova et al., 1999) and fitting of an ideal profile (Steyn et al., 1999). Three of the methods are presented here.

## 4.1 The vertical gradient of the aerosol profile

The vertical gradient of the backscatter profile is calculated with a central-difference formula

$$\frac{\partial \beta}{\partial z}(z_i) \approx \frac{\beta(z_i + \Delta z) - \beta(z_i - \Delta z)}{2\Delta z} \tag{23}$$

where $\beta$ is the backscatter, $z_i$ a reference height and $\Delta z = 20m$ (from the ceilometer settings). The minimum value of the gradient often indicates the BLH.

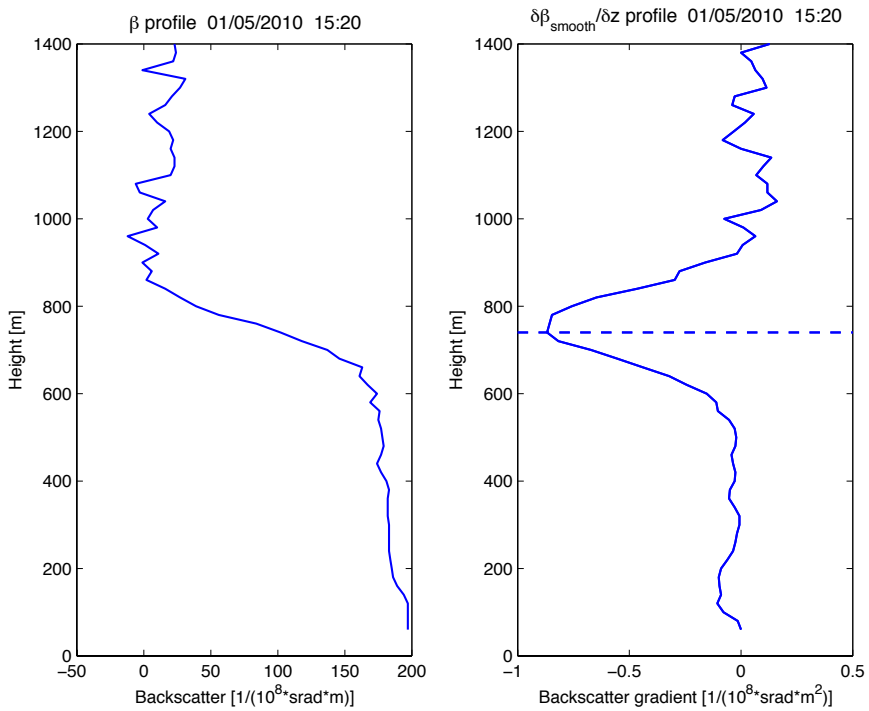


*Figure 10*: On the left: The vertical backscatter profile. On the right: The vertical gradient of the smoothed backscatter profile. Dashed line shows the BLH estimate. Data is from the ceilometer on May 1 2010.

Fluctuations due to noise in the backscatter profile may give large noise induced gradients. These may sometimes be misinterpreted in automated BLH detection programs as the BLH. These misinterpretations may be reduced by smoothing of the backscatter profile and then calculating the vertical gradient of the smoothed profile. In this study the backscatter profile is smoothed with a moving average filter spanning 7 measuring heights before calculating the gradient. The vertical gradient method is computationally simple and therefore comparatively fast in automatic BLH detection programs. In Figure 10 is seen the vertical backscatter profile along with the calculated vertical gradient of the smoothed backscatter profile. The BLH estimate is made where the minimum of the backscatter gradient is found.

## 4.2 Critical threshold value of the aerosol profile

In the ABL the aerosol concentration and the backscatter values are relatively high. Therefore one method of estimating the BLH is by applying a critical threshold value to the backscatter profile. This value will lie in the transition from high backscatter values to low, and would best represent the BLH as approximately half the mean mixed layer backscatter. As the mean mixed layer backscatter varies considerably ($\sim$50–300/($10^8$ m srad)), a constant critical value will overestimate the BLH when aerosol concentrations are relatively high, and underestimate, or even not estimate the BLH at all, when aerosol concentrations are low.

An automated BLH detection algorithm is therefore developed for this study with a variable critical threshold value. The approach of the method is to define a critical threshold value, $\beta_{crit}$ and a 'maximum' mean backscatter value $\beta_m$. Here set to $\beta_{crit} = 100/(10^8$ m srad) and $\beta_m$=150/($10^8$ m srad). The first height with backscatter values below $\beta_{crit}$ is then taken as a preliminary BLH estimate. Next, the mean backscatter from ground level to that height is calculated. If this value is above $\beta_m$ the BLH estimate is used, else it is discarded and the process is repeated with lower $\beta_{crit}$ and $\beta_m$ values (here 60/($10^8$ m srad) and

$90/(10^8\ \mathrm{m\ srad})$, respectively). For very low aerosol concentrations these values may still prove too high, and $\beta_{crit}$ is set to $40/(10^8\ \mathrm{m\ srad})$.

The values of $\beta_{crit}$ and $\beta_m$ are somewhat arbitrary, and may be chosen differently. Here the values are chosen after exploring the sensitivity of the method in a variety of aerosol backscatter profiles.

## 4.3 Fitting an idealized aerosol backscatter profile

Under ideal cloudless conditions, when the ABL is well mixed, the observed backscatter profile will show a shape that resembles an error function. Steyn et al. (1999) developed a method that exploits this resemblance.

The method involves minimizing the differences between an idealized backscatter profile $B(z)$ and the observed backscatter profile $\beta(z)$. The idealized backscatter, $B$, at height $z$ is given as

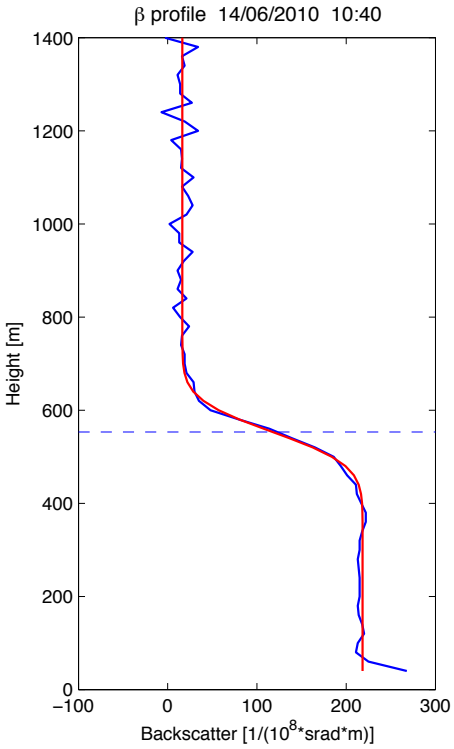


*Figure 11*: The vertical backscatter profile and the idealized profile. The profile parameters are: $B_m$=218, $B_u$=16 and $s$=79. Dashed line indicates the BLH estimate, $z_m$ = 553 m. Data from the ceilometer on June 14 2010.

$$B(z) = \frac{B_m + B_u}{2} - \frac{B_m - B_u}{2}\mathrm{erf}\left(\frac{z - z_m}{s}\right) \tag{24}$$

where $B_m$ is the mean backscatter in the mixed layer, $B_u$ is the mean backscatter above the mixed layer, $z_m$ the mixed layer height and $s$ is a normalization constant related to the entrainment zone thickness (EZT). The EZT is defined here to be the area where backscatter values drop from $0.95B_m$ to $0.05B_m$. The profile parameters are determined by a nonlinear curve fitting procedure, minimizing the least squares between $\beta(z)$ and $B(z)$.

$$\underset{B_m,B_u,z_m,s}{min} \sum_i \Big(B(B_m, B_u, z_m, s, z_i) - \beta(z_i)\Big) \tag{25}$$

An initial guess is needed for the parameters before solving the least squares. Here $B_u = 0$ and $s = 30$ are held constant but $B_m$ and $z_m$ are found from the critical backscatter method.

In Figure 11 is seen an example of the idealized profile fitted to the measured aerosol backscatter values from the ceilometer. There is a close resemblance between the two profiles, as the conditions for BLH detection are ideal. Notice though, that equation 25 is not based on physical considerations, but merely applied on observational grounds. This method is fairly easy to implement in automatic detection algorithms, but is computationally heavier than the previously mentioned methods. Smoothing of the aerosol backscatter profile before fitting with the idealized profile does not improve the results of the method.

## 4.4 Addition to the idealized profile

The observed backscatter profile in Høvsøre often differs from the idealized profile, especially when the winds are westerly. Then the observed profile generally shows higher backscatter values near the surface. This may be because the aerosols (in this case marine aerosols), close to the surface are heavier than those immediately above, and larger aerosols give higher backscatter values. Another reason could be that the near-surface air is more humid.

To make a better fit to the observed profile, an additional exponential term to the idealized profile is suggested in this study.

$$B(z) = \frac{B_m + B_u}{2} - \frac{B_m - B_u}{2} erf\left(\frac{z - z_m}{s}\right) + a\exp(-bz) \tag{26}$$

where $a$ is the initial value, and $b$ the growth factor of the exponential function.

Under certain circumstances this improved profile fits the aerosol profile better than the idealized profile, resulting in a more robust BLH detection. This is seen in Figure 12, where a fitted idealized profile is shown, both with and without the added exponential term. The BLH estimate with the exponential term is ∼150 m higher than the estimate without. The thickness of the EZT is reduced considerably by the new method, where $s$ is found to be less than half of the value fitted by the idealized profile.

The addition of the exponential term makes the non-linear curve fitting algorithm computationally more intense, with two additional parameters to fit. A great improvement is done in the fitting process by defining lower and upper bounds on all fitted parameters. This minimizes misfits of the profile and speeds up the procedure. The method will be called the exponent idealized profile.

## 4.5 Filtering clouds

In the available ceilometer data, clouds are very frequently observed. Cloud droplets give very high backscatter values, often more than 100 to 1000 times stronger than backscatter values in clear sky conditions. These high values dominate the backscatter profile as high peaks and the boundary-layer structure is not visible due to these peaks. The BLH detection methods are not always able to identify the BLH in cloudy conditions and they automatically detect the BLH at the top or the bottom of the cloud. This may cause problems in automated BLH detection programs, when the cloud is well above the ABL as seen in Figure 13.

Here is presented a new method to filter the clouds to gain better control of BLH detection in cloudy conditions. Backscatter signals greater than $1000/(10^8 \text{ m srad})$ are interpreted as indicating clouds, fog or precipitation, and therefore filtered (or removed). The neighbouring backscatter values to the cloud, $\beta(z_{cloud} + \Delta z)$, $\beta(z_{cloud} + 2\Delta z)$,$\beta(z_{cloud} - \Delta z)$, $\beta(z_{cloud} - 2\Delta z)$, are also removed regardless of their value. Three different methods are used to fill in the 'gap' of removed $\beta$ values.

1. Every data point in the gap is set to zero.

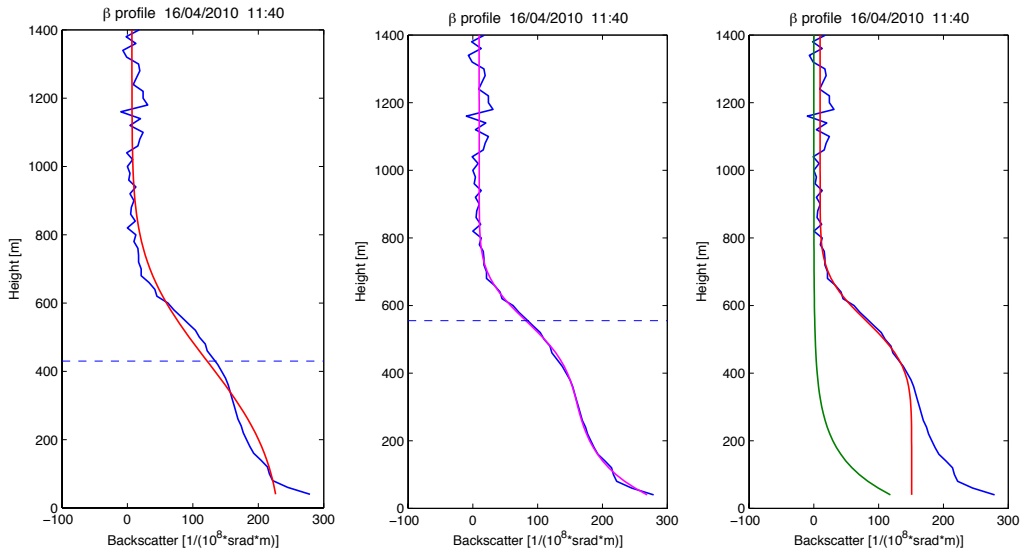


*Figure 12*: Left: The vertical backscatter profile (blue) with the corresponding fitted idealized profile (red). The profile parameters are: $B_m$=237/($10^8$ m srad), $B_u$=7/($10^8$ m srad), $s$=325 m and $z_m$=430 m. Middle: The same backscatter profile (blue) with the corresponding fitted exponent idealized profile (magenta). The improved profile parameters are: $B_m$=151/($10^8$ m srad), $B_u$=10/($10^8$ m srad), $s$=150 m, $z_m$=555 m, $a$=167 and $b$=0.01. Right: The backscatter profile (blue) and the exponent idealized profile split into the exponent contribution (green) and the idealized profile (red). Data from the ceilometer on April 16 2010.

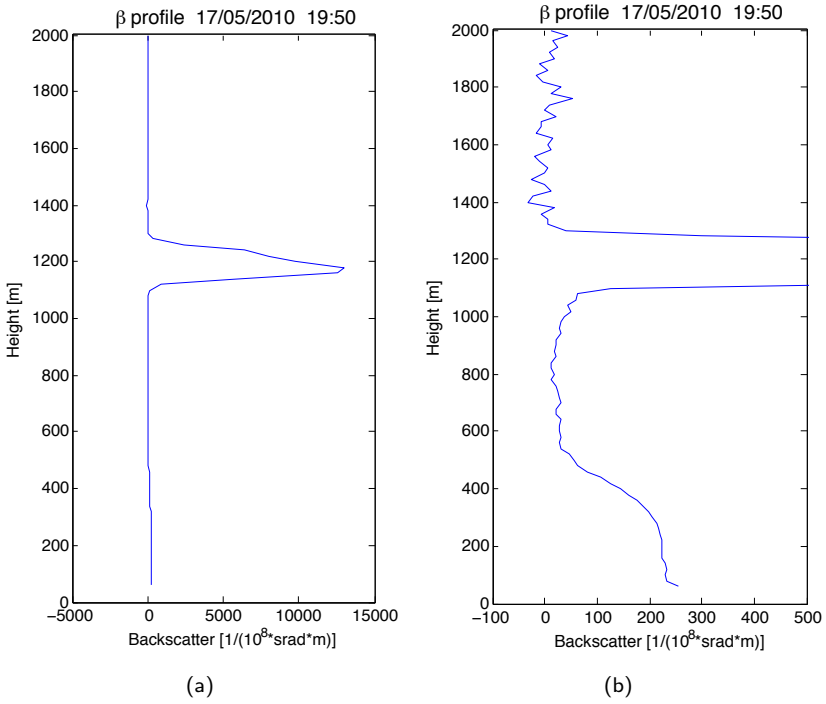


*Figure 13*: (a): Aerosol backscatter profile, with a decoupled cloud well above the ABL. The cloud base is at ∼1100 m. The cloud signal peaks at ∼ 13000/($10^8$ m srad). (b): Zooming in on the $\beta$-profile reveals the boundary-layer structure around ∼400 m.

2. An interpolation between the non-removed values. Either linear- or nearest neighbour interpolation[5] may be used.

3. Every data point in the gap is set to the cloud base value.

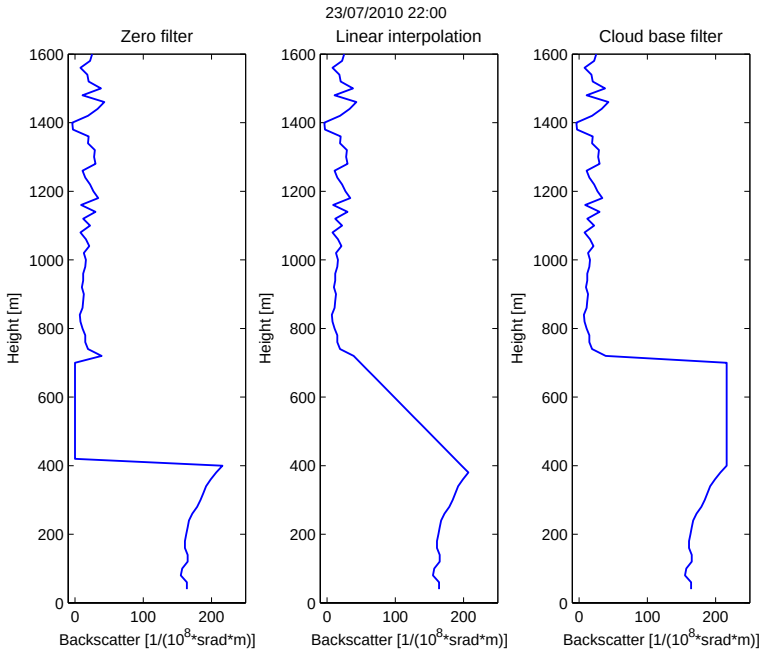


*Figure 14*: A cloud topped ABL showing the three different cloud filtering methods.

These three filtering methods can be seen in Figure 14. If there is fog an extrapolation is made from the first above ground 'non-removed ' $\beta$ value.

As mentioned in section 2.7, it is a matter of definition where to identify the BLH in a CTBL. But with these three different filtering methods it is possible to detect the BLH matching the chosen definition of the CTBL.

The cloud definition value $\beta(z) = 1000$ is chosen relatively high to ensure the presence of a cloud. A lower value of cloud definition $\beta(z) = 800$ has been tested, with no noticeable differences from the higher value.

## 4.6 Minimum turbulence kinetic energy

The wind lidar provides measures of wind velocity fluctuations. These are given as the standard deviations of the mean wind velocity components $\sigma_u, \sigma_v$ and $\sigma_w$ and may be used to calculate the TKE of the wind field with equation 3. The TKE approaches zero at the top of the ABL as the wind velocity fluctuations are small in the laminar flow above the ABL. The BLH may therefore be estimated as the height where the TKE drops below a critical value (Vickers and Mahrt, 2004).

Figure 15 shows the vertical profiles of $\sigma_u, \sigma_v$ and $\sigma_w$ and the associated vertical profile of the TKE. The height of the wind lidar measurements is limited by the height of the aerosol content in the atmosphere, leading to height limited vertical profiles of $\sigma_u, \sigma_v$ and $\sigma_w$. Therefore the minimum value of the TKE is used as a BLH estimate in this study, instead of defining a critical value. If there are more than one equal minimum values the lowest one is used as a BLH estimate.

[5] The nearest neighbour method takes the value of the nearest point only, yielding a piecewise interpolation.

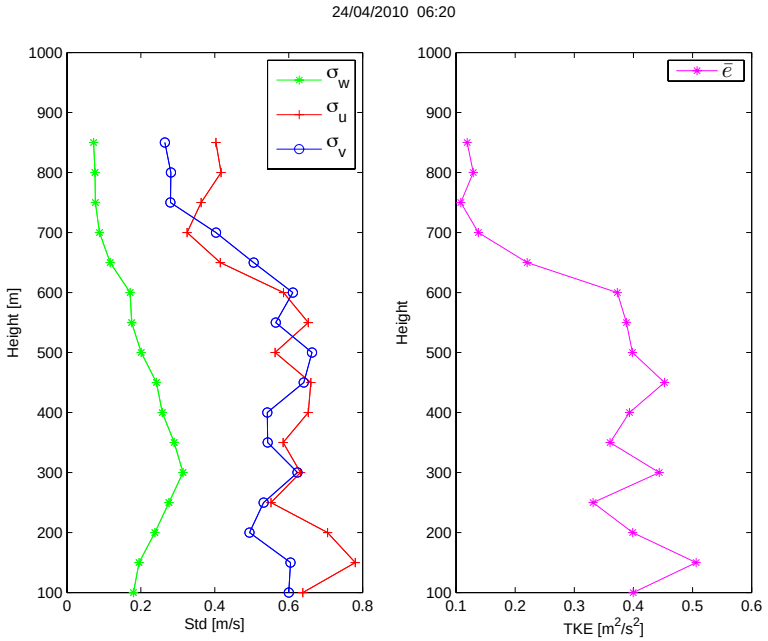


*Figure 15*: Left: The vertical profiles of the wind velocity fluctuations. Right: The vertical profile of the calculated TKE. Data is from the wind lidar on April 24 2010.

# 5 Results

## 5.1 Clouds

A simple estimate of cloud cover is made from the ceilometer data. Every time the backscatter signal exceeds $1000/(10^8 \text{ m srad})$, the algorithm indicates either cloud or fog and the time step is noted as a cloud observation. As mentioned in section 3 the ceilometer measurements cover the period from April 2010 to March 2011 with 10 s time resolution. From the analysis of the 10 min data stored in the database, it is seen that 58 % of the time the presence of clouds is detected within the vertical range of 200 – 3000 m. The starting height of 200 m is chosen to avoid mist events that give very high backscatter values at the lowest measuring heights.

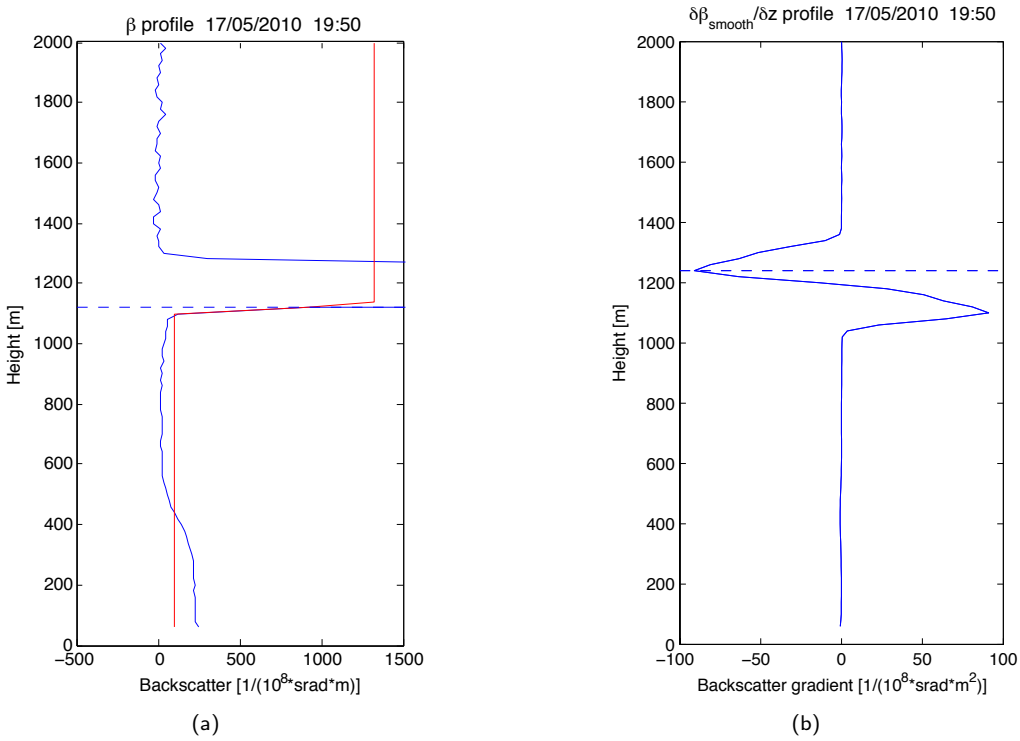


*Figure 16*: Left: Blue line indicates the backscatter profile, while the red line indicates the fitted idealized profile. The high values in the backscatter at ∼1100–1300 m indicate a cloud layer. The profile peaks at $13000/(10^8 \text{ m srad})$. Right: The vertical gradient of the smoothed backscatter profile. Backscatter values peak at height 1200 m. Horizontal dashed lines indicate estimated BLH. Data is from the ceilometer on May 17 2010 at 19:50.

### Decoupled Clouds

Clouds that are not boundary-layer clouds, i.e. those that are decoupled from the ABL or well above it, still influence the BLH detection. As seen in Figure 16 the cloud signal dominates the backscatter profile where the highest signals are $\sim 13000/(10^8 \text{ m srad})$. Both the fitting of the idealized profile seen in Figure 16(a) and the vertical gradient of the smoothed backscatter seen in Figure 16(b) fail to detect the BLH that is seen to be at ∼400 m. The idealized profile method finds the minimized differences by identifying the BLH at the cloud base at ∼1110 m. The vertical gradient method identifies the BLH at the cloud top at ∼1250 m.

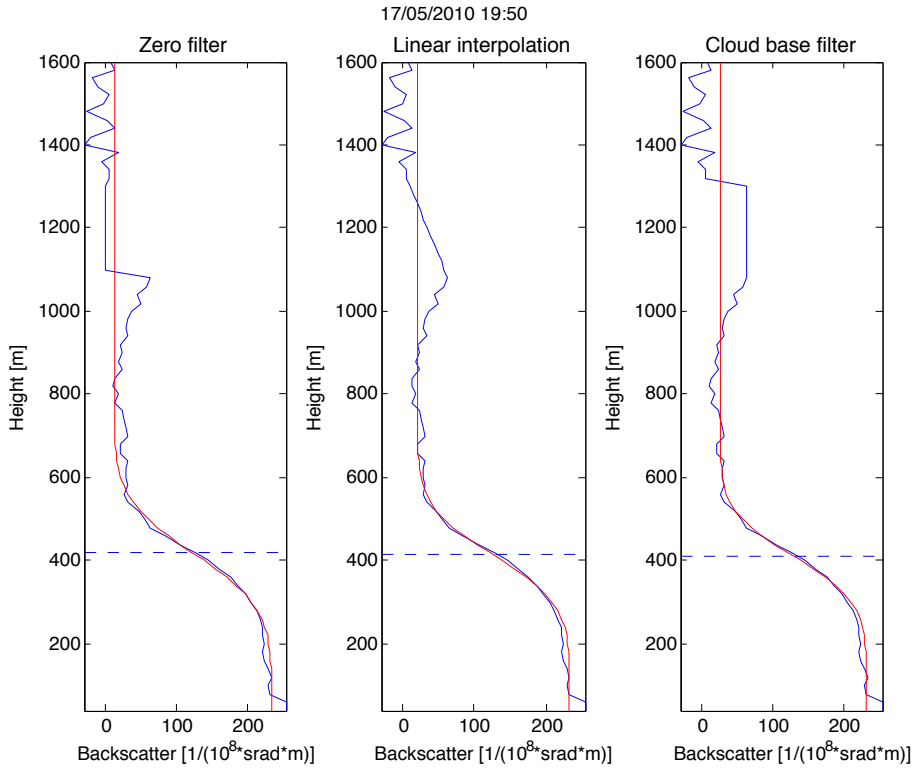


*Figure 17*: Plots of three different cloud filtering methods with associated fitting of the idealized profile. Blue lines indicate backscatter profile while red lines indicate idealized profile. Horizontal dotted lines indicate BLH estimates. Data taken from the ceilometer May 17 2010 at 19:50.

Filtering decoupled clouds improves the BLH detection significantly. This is seen in Figure 17 showing three different cloud filtering methods (the zero filter, linear interpolation and cloud base filter) and the idealized profile BLH detection method. This figure shows the same backscatter profile as in Figure 16 only with the cloud filtering applied. The cloud signal does not dominate the backscatter profile any longer and the idealized profile now makes a better fit, identifying the BLH right above 400 m.

It is seen in Figure 17 that the BLH estimates are independent of the chosen cloud filtering method. This is because in this case the cloud is ∼700 m above the detected ABL. However in conditions with a cloud topped ABL, the chosen cloud filtering method will influence the BLH estimate of all methods.

### The cloud topped boundary layer

In situations with a CTBL, the BLH detection methods often detect the BLH at the top of the cloud. This might not always cause wrong detections, depending on the chosen BLH definition with a cloud topped boundary layer. As mentioned in section 2.7 when a CTBL is

observed and the cloud layer and boundary layer are turbulently fully coupled then defining the BLH at the top of the cloud may be preferable. When working with ceilometer data alone, it cannot be determined if the two layers are fully coupled and it may be convenient to define the BLH in another manner than at the cloud top.

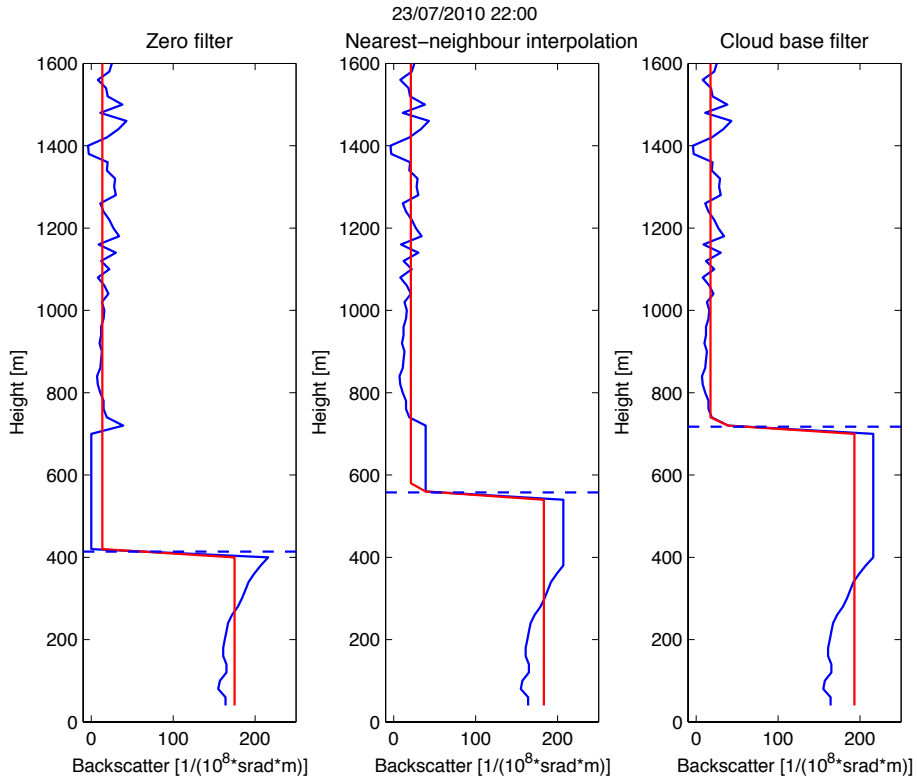


*Figure 18*: Three different cloud filtering methods applied to the backscatter profile. The blue line is the backscatter profile, while the red line is the idealized profile. Dotted horizontal lines indicate the estimated BLH. Data is from July 23 2010 at 22:00.

The cloud filtering methods allow the BLH detection algorithm to gain better control over the aerosol backscatter profile under the presence of clouds and determine the BLH according to the chosen BLH detection method. Figure 18 shows the idealized profile fitted to a backscatter profile, where clouds were filtered with three different methods. In Figure 18 (left) the zero filter is applied, setting all signals in the cloud layer to zero. This results in a sharp decrease in the backscatter at the cloud base and the BLH detection methods generally identify the BLH in such a sharp transition. In this case the BLH estimate is ∼400 m.

In Figure 18 (middle) the signals in the cloud layer were filtered with nearest neighbour interpolation, resulting in a sharp transition in the middle of the cloud layer. This filtering method proposes the BLH detection methods estimate the BLH in the middle of the cloud, corresponding well with a BLH definition treating the cloud layer as an entrainment zone. Cloud filtering with linear interpolation gives similar results as the nearest neighbour interpolation, though the BLH estimates tend to be slightly higher with the linear interpolation. Here the BLH estimate is ∼550 m. Figure 18 (right) shows the cloud base filtering, where the signals in the cloud are set to the same backscatter value as the cloud base. With this filtering method the BLH estimates are detected at the cloud top. Here the BLH estimate is ∼750 m. The BLH estimates with the cloud base filter mostly give the same results in a CTBL case as no filtering at all, especially when using the vertical gradient and the threshold methods. However the cloud filtering gives better control of the data and the profile fitting methods are improved. As seen in Figure 16(a) the profile fitting methods do not always detect the BLH at the cloud top.

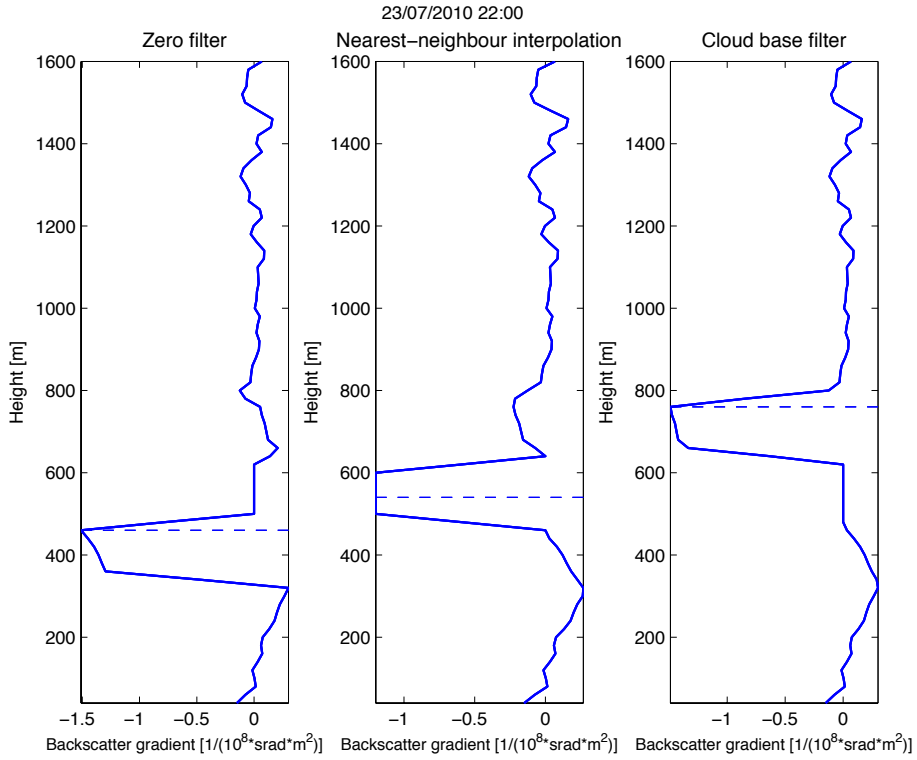


*Figure 19*: The vertical gradient of the smoothed backscatter profile with three different cloud filtering methods. The dashed horizontal line indicates the BLH estimate from the method. Data is from the ceilometer on July 23 2010 at 22:00.

Figure 19 shows the vertical gradient of the smoothed backscatter profile with three different cloud filtering methods. The vertical gradients are calculated from the same profiles as shown in Figure 18 with the same cloud filtering. In the left figure the BLH is estimated at ∼450 m, approximately 50 m higher than compared to the idealized profile. In the middle figure the BLH is estimated at ∼550 m, approximately the same height as the idealized profile. In the right figure the BLH estimated at ∼750 m, approximately 50 m higher than the idealized profile. These differences are due to the smoothing of the backscatter profile before BLH detection with the vertical gradient method.

Figure 20 shows the backscatter intensities on August 19 2010. A CTBL is observed with varying cloud thickness of 100–800 m. All BLH estimates are made with the critical threshold detection method, but three different cloud filtering methods are used for the estimates. The BLH estimate with zero filter (black circles) follow the cloud base. The nearest neighbour interpolation (green triangles) generally show a BLH in the middle of the cloud, though a few are at the top, coinciding with the pink stars. In these situations the cloud top is diffuse and the top and bottom values that the interpolation is made between are of similar size. The BLH estimates performed with the cloud base filtering method follow the cloud top.

It is seen from Figure 20 that BLH estimates made on backscatter profiles with zero cloud filtering applied, show the least variation in height. These estimates vary between ∼400–700 m following the cloud base. The cloud top height on the other hand changes rapidly with the cloud thickness, where the cloud top varies between ∼700 m and ∼1400 m, resulting in fluctuating BLH estimates.

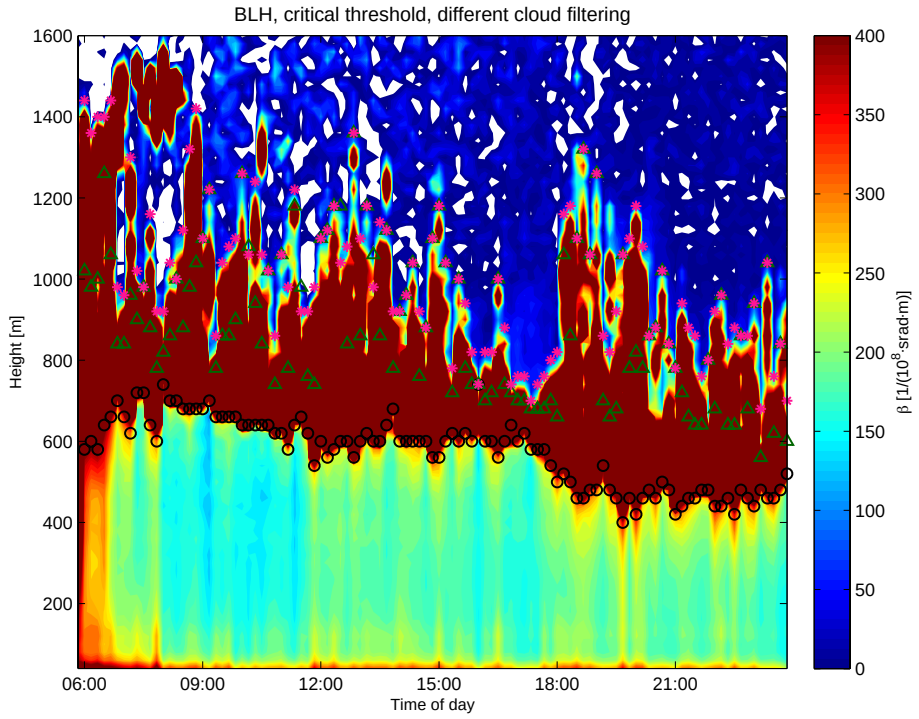


*Figure 20*: The backscatter coefficient measured with the ceilometer on August 19 2010. The coloured shading indicates the intensity of the backscattered light, blue shading indicates minimal scattering and white indicates negative backscatter values. All BLH estimates are made with the critical threshold method and three different cloud filtering methods are applied. The black circles indicate zero filter, green triangles indicate nearest neighbour interpolation and pink stars indicate the cloud base filter.

## 5.2 Continuous and average data

The ceilometer at Høvsøre provides measurements of the aerosol backscatter every ten seconds (henceforth, 10 s data). These data are not readily available on the Høvsøre database, but remain stored at the Risø met data server. The ten minute means (henceforth, 10 min data) of these high resolution data are as mentioned in section 3 available on the database.

To compare the BLH estimates of 10 min data with those of the 10 s data, BLH estimates are made for every 10 s data during a ten minute interval for a single whole day. The mean of these 60 estimates is calculated (henceforth, 10 s mean BLH) and compared to the 10 min data BLH estimates.

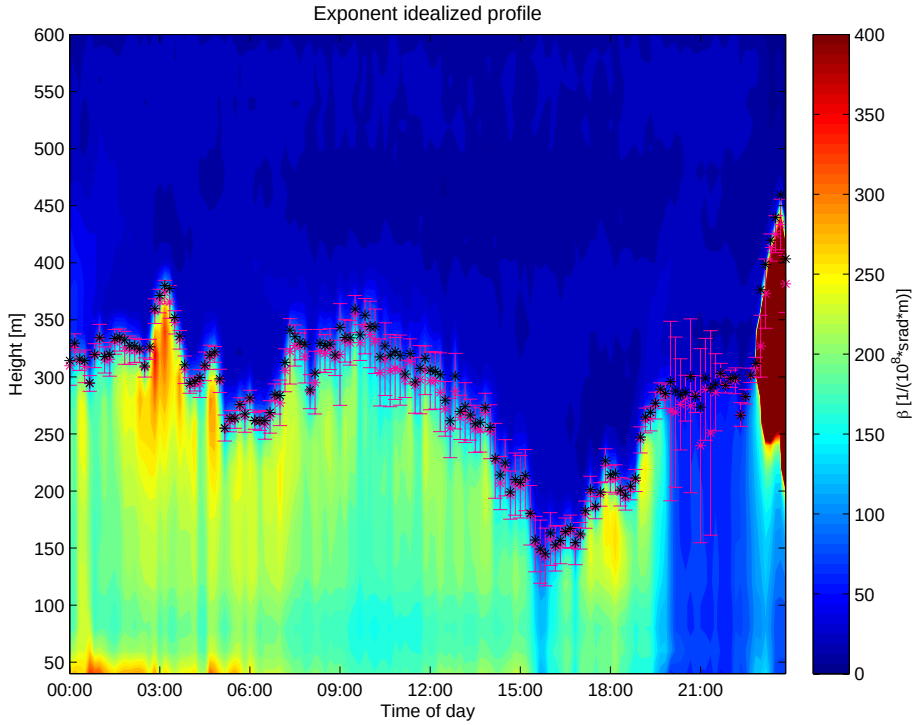


*Figure 21*: The diurnal evolution of the ABL on June 21 2010. The BLH estimates are found by fitting the exponent idealized profile. Black stars indicate the BLH estimates from the 10 min data and magenta stars the BLH estimates from the 10 s mean BLH. The error bars represent the standard deviation of the 10 s estimates within 10 minutes.

In Figure 21 the BLH estimates from the different data types, 10 s and 10 min, are illustrated for an entire day, starting at midnight. These BLH estimates have all been performed by fitting the exponent idealized profile described in Section 4.4. It should be noted that the error bars shown are not exact errors, but the BLH variability, found by computing the standard deviation, $\sigma$ of all 10 s BLH estimates within 10 minutes. It is seen that the variability is generally larger during daytime, from around 7:00 to 16:00, than during nighttime, from 00:00 to 07:00. The standard deviation of the BLH estimates is largest in the late evening from 20:00 to 22:00, where the backscatter signal is relatively weak. The cloud visible from around 23:00 has been removed with the cloud base filter described in Section 4.5. The BLH estimates from the two data sets agree very well, though with a tendency in the 10 min data estimates to be a little higher, especially during daytime. This is common for all four methods of BLH detection, and may be seen in appendix B where plots similar to Figure 21 are made for the remaining three detection methods.

Figure 22 shows a scatter plot of the 10 min BLH estimates and those 10 min means derived from the 10 s estimates from the four different BLH detection methods. As in Figure 21 the

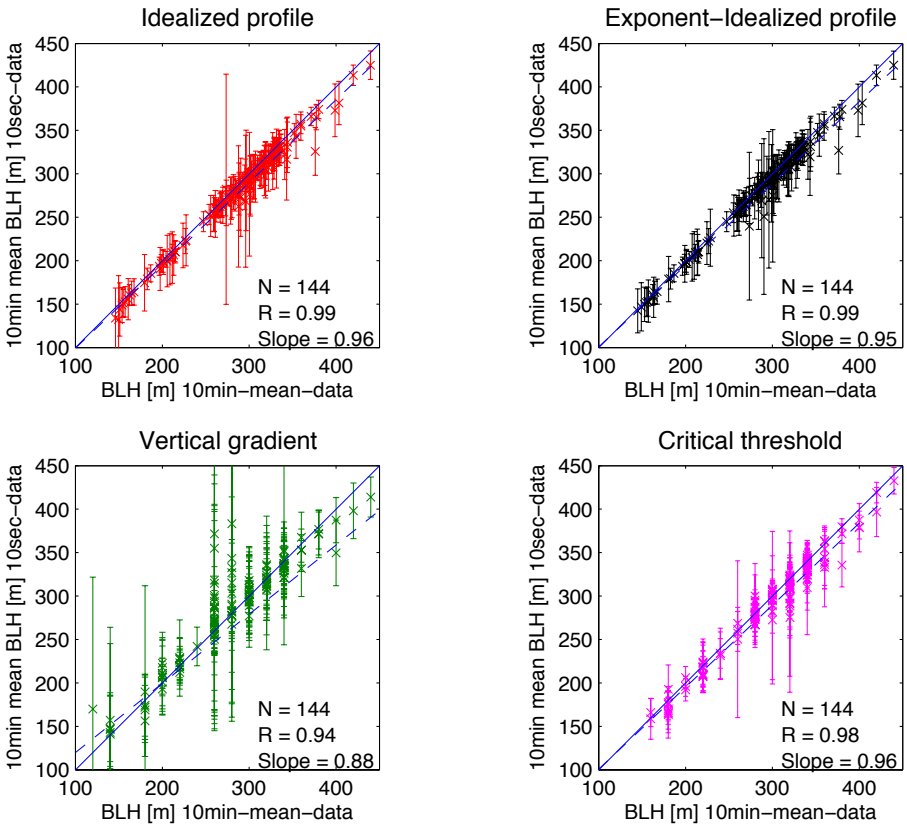


*Figure 22*: Scatter plots of BLH estimates from 10 s data for June 21 2010 using the various BLH detection methods. Error bars represent the standard deviation of BLH estimates within 10 minutes. N = number of estimates, R = correlation coefficient, Slope = the slope of the linear regression ($a$). Dashed line is the linear regression. Blue solid line is the 1:1 line.

| Method | RMSD [m] | Mean $\sigma$ [m] |
|---|---|---|
| Idealized profile | 10 | 21 |
| Exp. ideal. profile | 10 | 19 |
| Vertical gradient | 23 | 48 |
| Critical threshold | 12 | 21 |

*Table 2*: Root mean square deviation and the mean standard deviation of the different BLH detection methods for 10 s data, June 21 2010.

error bars represent the standard deviation of the BLH estimates from the 10 s data within 10 minutes. The slopes are calculated by a simple linear regression with a least square estimator. The slopes are all less than 1, indicating the tendency for the BLH estimates from the 10 min data to generally be a little higher as mentioned above. All four methods show excellent correlation between the data, with the lowest correlation of 0.94. These high correlations are also expected, as the data sets (10 s and 10 min) are not independent. The critical threshold and the vertical gradient methods depend on the height resolution (in this case 20 m). For this reason the BLH estimates for the 10 min data appear as discretized, while the 10 s data mean BLH estimates vary more smoothly over height. Thus many values in the figure are difficult to distinguish as crosses and error bars are on top of each other. The profile fitting methods on the other hand are independent of the height resolution, estimating the BLH in the middle of the apparent interfacial layer.

Table 2 shows the root mean square deviations (RMSD) between the BLH estimates from 10 min data and the 10 s data mean BLH estimates. The mean $\sigma$ is simply the averaged size

of the error bars during the day. The two profile fitting methods have the lowest RMSD, 10 m and the exponent idealized profile method shows the lowest mean $\sigma$. The method showing largest $\sigma$ is the vertical gradient, also with the largest RMSD.

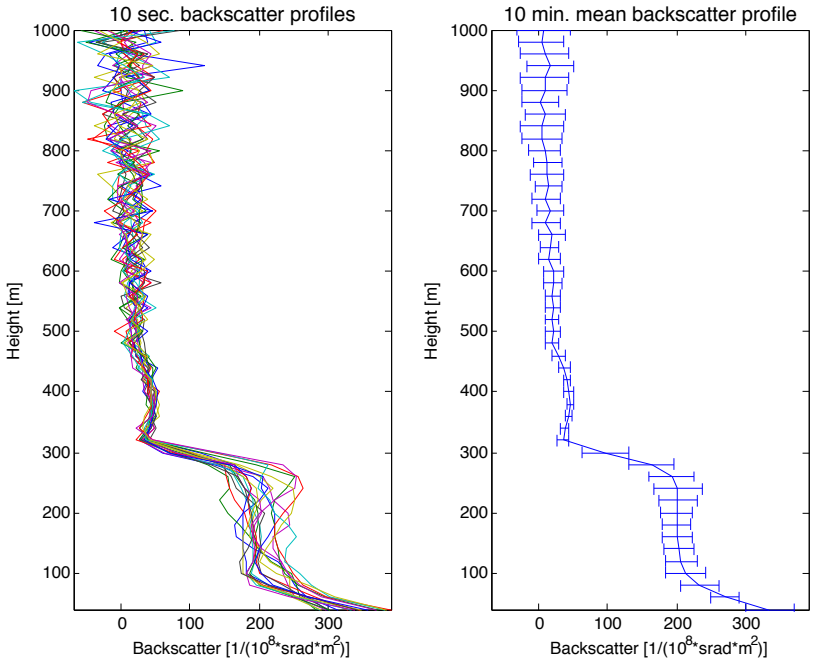


*Figure 23*: On the left: Vertical backscatter profiles measured every 10 seconds from 00:40 to 00:50. Every third profile is shown. On the right: The average of the sixty 10 s profiles from 00:40 to 00:50. With error bars representing the standard deviation of the backscatter signal at every measured height. The BLH is seen to be around 300 m.

| Method | BLH [m] 10min data | Mean BLH [m] 10s data | $\sigma$ [m] |
|---|---|---|---|
| Idealized profile | 288 | 276 | 24 |
| Exp. ideal. profile | 295 | 294 | 7 |
| Vertical gradient | 260 | 275 | 40 |
| Critical threshold | 300 | 307 | 10 |

*Table 3*: BLH detection between 00:40 and 00:50, showing the results for the four methodologies.

To further compare the 10 min data with the 10 s data, two 10 minute intervals from the day are chosen for plotting the vertical profile of the backscatter. The first interval is from 00:40 to 00:50, during nighttime. The vertical profiles are seen in Figure 23. The left plot shows the vertical 10 s backscatter profiles [6] while the right plot shows the related mean backscatter profile. The standard deviation of the signal within 10 minutes is shown as horizontal error bars on the right plot. It is noteworthy how little variability there is in the signal immediately above the ABL, and generally higher deviation of the signal within the ABL, especially in the transition zone. Above the ABL the standard deviation of the signal increases with height due to noise, as the measured signal strength is inversely proportional to the squared height as seen in equation 15.

Table 3 shows the related BLH estimates from the 10 min and the 10 s data, together with the standard deviation of the 10 s BLH estimates, between 00:40 and 00:50. The vertical pro-

[6] Only every third profile is shown for better visualization.

files show a shape that fits well with the exponent idealized profile, i.e increasing backscatter values from $\sim 100$ m down to the surface. The exponent idealized profile method detects the BLH with the least $\sigma$, only differing one meter between the 10 min and 10 s data.

The second time interval is chosen from 09:00 to 09:10 during daytime. In Figure 24 is shown plots analogous to those seen in Figure 23 for this second time interval. The error of the signal is greater during the daytime as the ambient sunlight influences the light detection of the ceilometer's laser among others. This is seen by the standard deviations both above and within the ABL being greater than those seen during nighttime. The standard deviation of the BLH estimates is also noticeably larger during daytime as may be seen in Table 4, with values up to 6 times larger than during nighttime (for the exponent ideal profile method). Hennemuth and Lammert (2006) noted that this variability may be caused by single convective eddies with a time scale of a few minutes. The variability might also be caused by gravity- or Kelvin-Helmholtz waves.

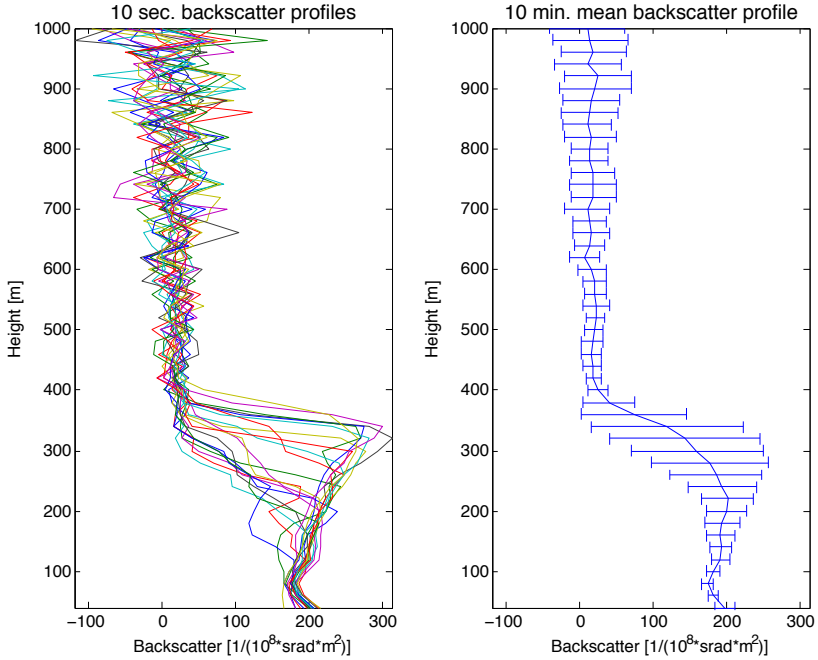


*Figure 24*: On the left: Backscatter profiles measured every 10 seconds from 9:00 to 9:10. Every third profile is shown. On the right: The average of the sixty 10 s profiles from 9:00 to 9:10. With error bars representing the standard deviation of the backscatter signal at every measured height. The BLH is seen to be around 300 m.

| Method | BLH [m] 10min data | Mean BLH [m] 10s data | $\sigma$ [m] |
|---|---|---|---|
| Idealized profile | 343 | 316 | 47 |
| Exp. ideal. profile | 343 | 319 | 45 |
| Vertical gradient | 340 | 326 | 51 |
| Critical threshold | 360 | 333 | 46 |

*Table 4*: Results of the BLH detection methods on June 21 2010 between 9:00 and 9:10.

The averaging procedure results in a thicker interface between the ABL and the free atmosphere (Wyngaard, 2010). The 10 s profiles seen in Figure 24 show a sharper, or more horizontal interfacial layer compared with the 10 min mean. But the variability of the height of these sharp interfacial layers results in a very smooth and large interfacial layer of the 10 min mean profile. The reason for the generally higher BLH estimates of the 10 min data may

also be explained by the shape of the 10 s profiles in Figure 24. It is seen that the profiles estimating the BLH at higher levels also show the largest backscatter values at the top of the ABL, thereby contributing more to the mean value.

The shape of the vertical backscatter profile is influenced by RH. Figure 25 shows the RH measured at heights of 2 and 100 m in Høvsøre. From 00:00 to 6:30 the RH at 2 m is higher than at 100 m resulting in the high backscatter values near ground seen in Figure 23. From 6:30 to 15:30 the RH at 100 m is higher than at 2 m. The RH is likely to increase to the BLH as indicated by Figure 24, with the higher backscatter values at greater heights (∼350 m).

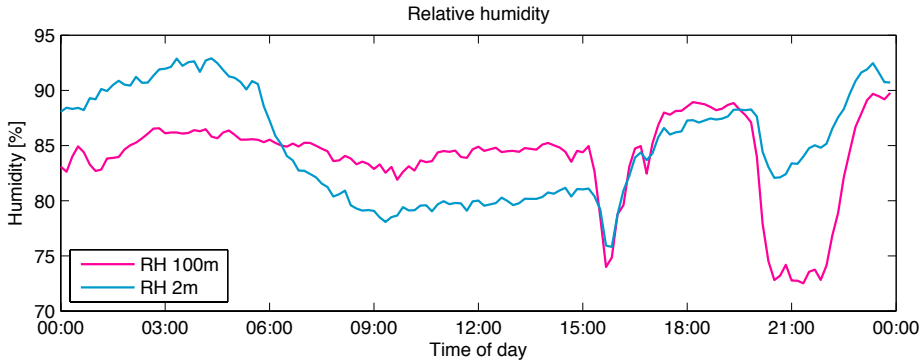


*Figure 25*: 10 min RH observations on June 21 2010.

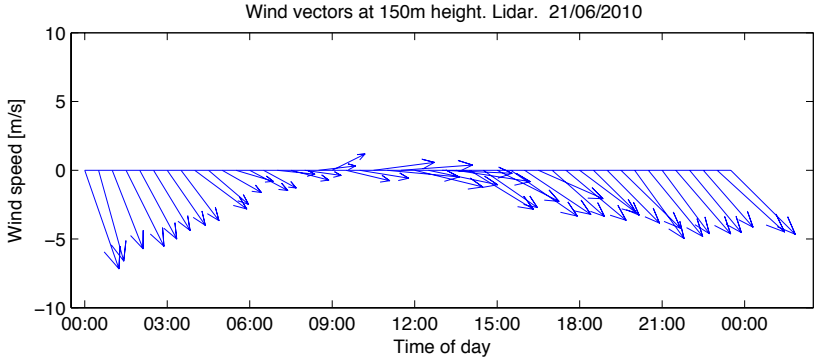


*Figure 26*: Wind speed and direction measured at 150 m with the wind lidar on June 21 2010. The length of the vectors indicates the wind speed and the scale of the wind speed is shown on the y-axis. Wind direction is given by the angle of the vectors (westerly winds along the positive x-axis). For clarity only every third wind vector is shown.

The winds are westerly as seen in Figure 26, indicating that the aerosol content is marine in origin. Notice that the sudden drop in RH around 20:00, is not related to a sudden change in wind direction. The RH measured at 100 m decreases from $\sim 90\%$ to $\sim 75\%$ around 20:00 and at the same time the measured ceilometer intensity is significantly reduced. The reason for this may be related to the hygroscopic growth of the marine NaCl aerosols. At a RH of $90\%$ they may be near twice their size at a RH of $75\%$ (Hämeri et al., 2001). The smaller the particle size, the less backscatter is measured by the ceilometer (Emeis et al., 2004).

## 5.3 Comparison with a wind lidar

As mentioned in section 4 numerous ways exist to define the BLH. To validate the BLH estimates of the ceilometer data, comparisons are made with BLH estimates from TKE calculations using wind lidar data. Two days are chosen for the comparison.

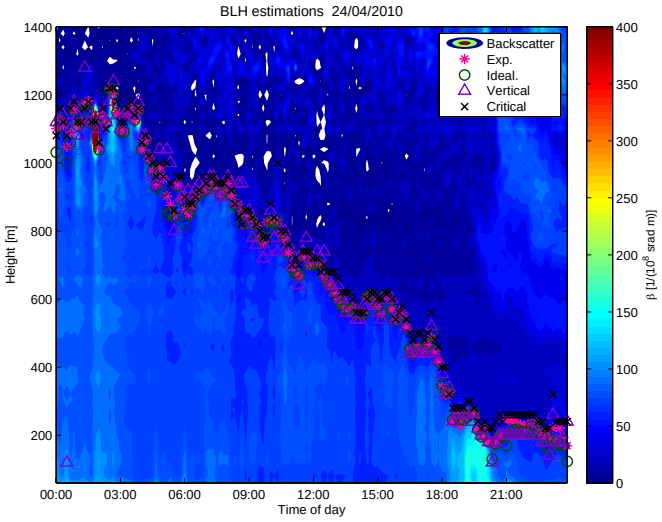


(a)

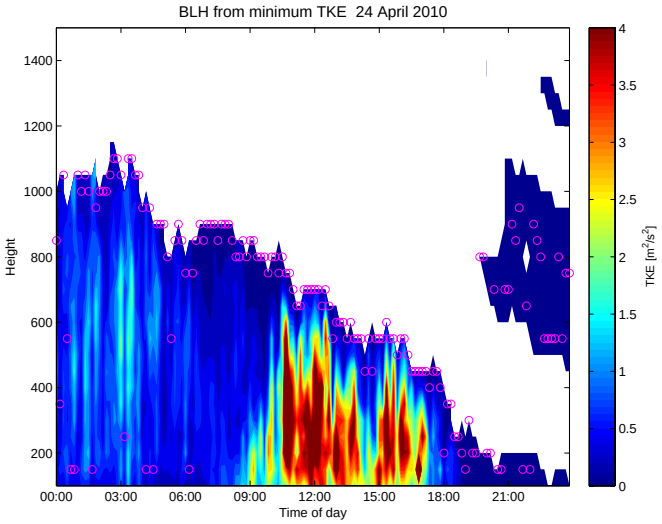


(b)

*Figure 27*: (a) The backscatter coefficient measured with the ceilometer on April 24 2010. Pink stars indicate BLH estimates with the exponent idealized profile, green circles the idealized profile, purple triangles the vertical gradient and black crosses the critical threshold. (b) The TKE measured with the wind lidar on April 24 2010. Pink circles indicate BLH estimates with the minimum TKE.

The mean variance of the wind speed components measured with the wind lidar are used to calculate the 10 min vertical TKE profiles. Two cases have been chosen for inter-comparison of the minimum TKE calculated with the wind lidar and BLH estimates retrieved from ceilometer data.

Figure 27(a) shows the backscatter intensities measured with a ceilometer on April 24 2010. The intensities are relatively low this day and nearly constant with height, though intensity

increases from 19:00–20:00. A residual layer is visible from 19:00 at ∼500 m. The four different BLH detection methods show very similar BLH estimates at ∼1100 m from midnight to 4:00. The BLH estimates show a generally decreasing height from 4:00–20:00, whereafter the BLHs are ∼200 m.

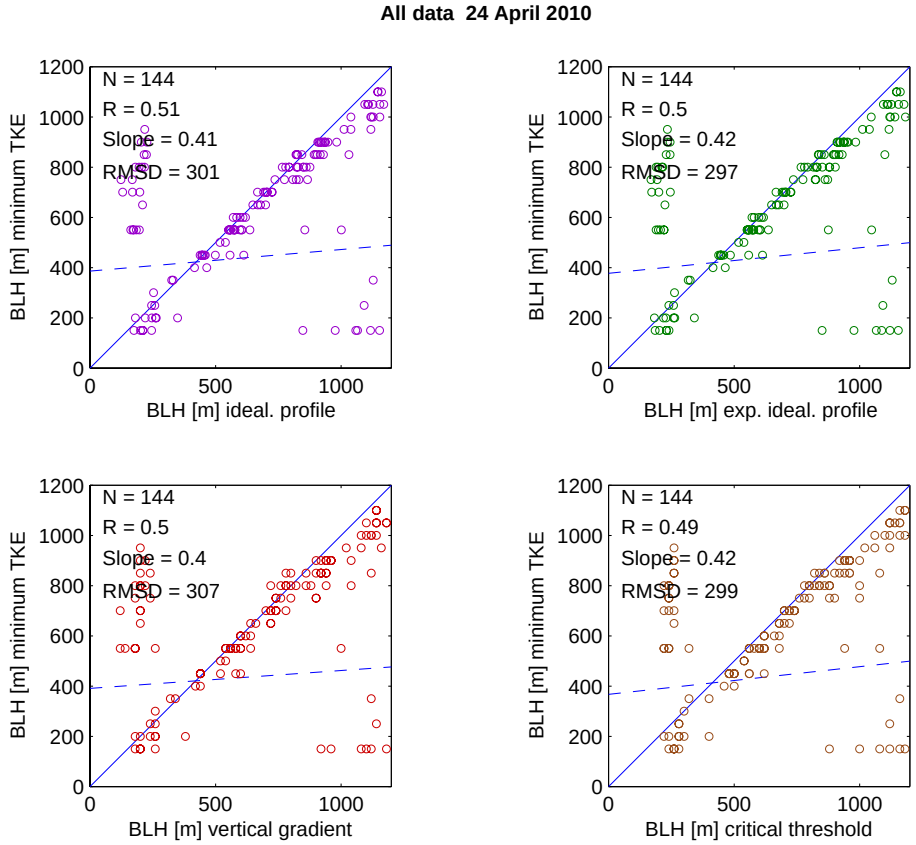


*Figure 28*: Inter-comparison between the BLH methods using the ceilometer and that using the minimum TKE using the wind lidar on April 24 2010. The dashed line is the linear regression and the solid line is the 1:1 line.

The TKE per unit mass is shown in Figure 27(b) and indicated by the colour bar, measured on the same day with the wind lidar. The minimum of every vertical TKE profile is indicated by a pink circle. From midnight to ∼9:00 the TKE values are relatively low, but clearly distinguishable minima are found. These minima indicate the BLH and most of them follow the cut-off value of the wind measurements, though with a few outliers closer to the surface. The turbulence is strongest from ∼10:00–17:00 showing high TKE values from the first measurement height (100 m) to the estimated BLH. After 18:00 turbulence generation decreases and no clear minima are found. The minimum values are scattered between a near surface layer and a residual layer visible from around 20:00. The estimates in the residual layer are somewhat artificial, as the TKE profiles are not continuous.

In Figure 28 it is seen that the inter-comparisons all show correlations ∼0.5 and slopes are all ∼0.4. Although the correlation coefficients are not high they are significant at 99.9% confidence level. In Table 1 is seen that a correlation of 0.26, where $N = 145$ is significant on a 99.9% confidence level. The low-valued correlation coefficients and slopes are due to the outliers, as most of the data points are seen to lie close to the 1:1 line.

A filtering method is applied to remove the outliers of the data and improve the correlation

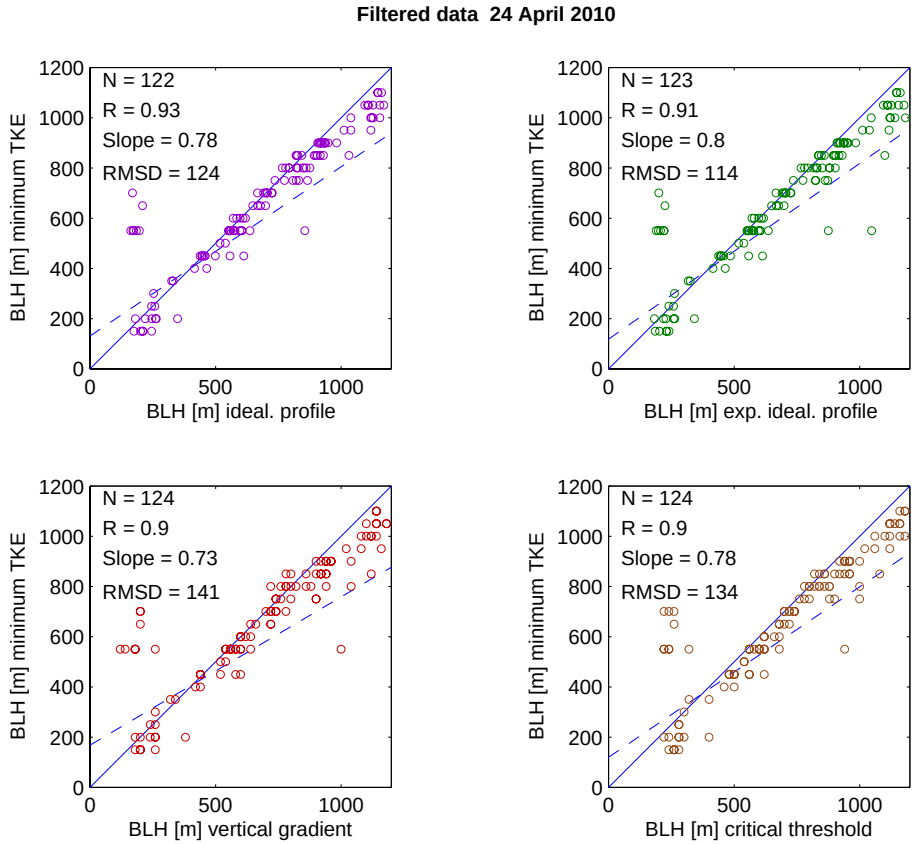


*Figure 29*: Inter-comparison between the BLH methods using the ceilometer and that using the minimum TKE using the wind lidar on April 24 2010. The dashed line is the linear regression and the solid line is the 1:1 line. Outliers have been filtered.

coefficients. This method is suggested by Milroy et al. (2012). The approach of the filtering method is to calculate the differences of minimum TKE and the four different BLH detection methods. All corresponding BLH estimates that are more than two standard deviations from the mean difference are removed before the correlation is calculated.

The inter-comparisons seen in Figure 29 all show $R \geq 0.9$ when the filtering is applied. The vertical gradient comparison shows a RMSD of 141 m, which is the largest and the exponent idealized profile comparison shows the lowest RMSD (114 m). All four methods result in slopes between 0.73 and 0.8. It is seen that the high BLH estimates are higher with the ceilometer data methods compared to the minimum TKE.

The second comparison is illustrated in Figure 30(a) from May 1 2010. Clouds are visible from midnight to 12:00, with a short 'break' around 10:00. The clouds were filtered with a nearest neighbour interpolation.

From 12:00 the backscatter intensities are relatively high throughout the day. The BLH estimates are similar for all four methods, except from around 10:00 to noon, when there are both a low and a higher cloud layer present. In this time interval the BLH estimates fluctuate between the low and high cloud layers and deviate from each other.

From the TKE plot in Figure 30(b) it is observed that when the cloud layer is detected with the ceilometer, the cut-off value of the wind lidar data is approximately at the same height as the cloud top. The CNR decreases to the cut-off value and the wind lidar does not measure above the cloud layer. Peaks of high TKE are seen most often at cloud top, indicating high turbulence generation. This is likely due to cloud entrainment and mixing. There is no clear zone of minimum TKE in the presence of the cloud layer. The minima scatter between 150

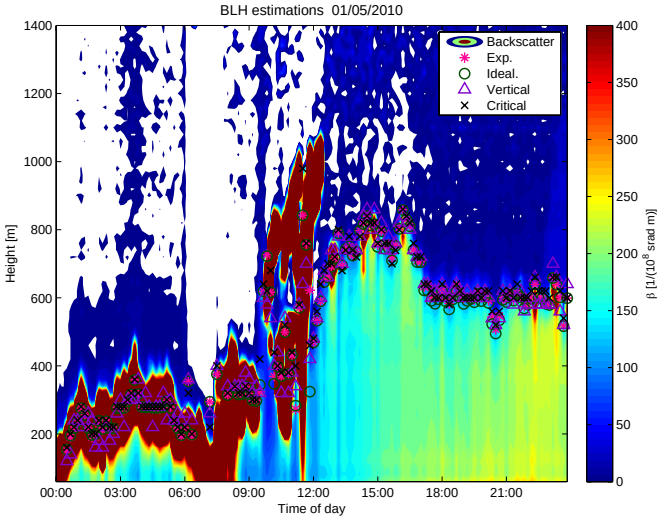


(a)

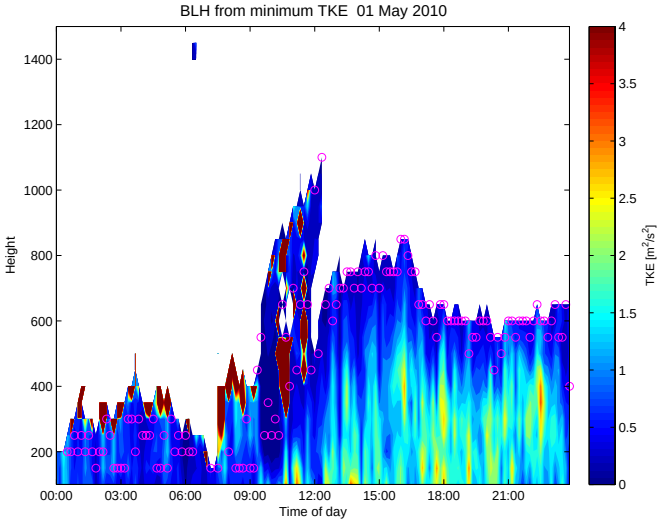


(b)

*Figure 30*: (a) The backscatter coefficient measured with the ceilometer on May 1 2010. Pink stars indicate BLH estimates with the exponent idealized profile, green circles the idealized profile, purple triangles the vertical gradient and the black cross the critical threshold. (b) The TKE measured with the wind lidar May 1 2010. Pink circles indicate BLH estimates with the minimum TKE.

m and the cloud top. BLH detection in cloudy conditions is therefore difficult or not possible with this particular method. The cloud layers are not observable after noon and the TKE increases showing relatively high values from the first measuring height to the estimated BLH ranging from ∼500–800 m.

The statistics of the inter-comparison is shown in Figure 31. As with the previous example, data that are more than two standard deviations apart are removed. All methods show linear correlations of 0.86 or 0.87. The methods all show similar RMSD (117–119 m) and slopes between 0.97 and 0.98. Although the TKE minima scatter between the first measuring height and the cloud top, this does not affect the correlation much due to the low height of the cloud layer.

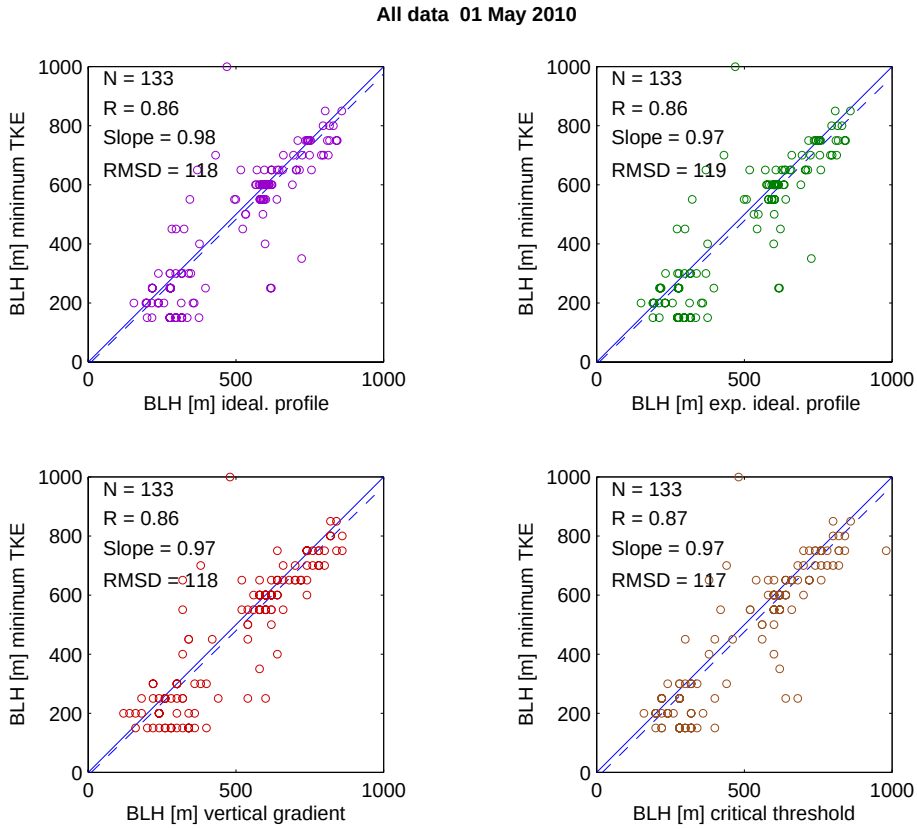


*Figure 31*: Inter-comparison between the BLH methods using the ceilometer and that using the minimum TKE using the wind lidar on May 1 2010. The dashed line is the linear regression and the solid line is the 1:1 line.

## 5.4 Cold front passage

On April 8 2010 a cold front passage was observed at around 5:00. Investigations of satellite figures and weather maps with included frontal analysis[7] were made to determine the frontal passage. These figures are however not shown here, only data from the Høvsøre measuring site are used.

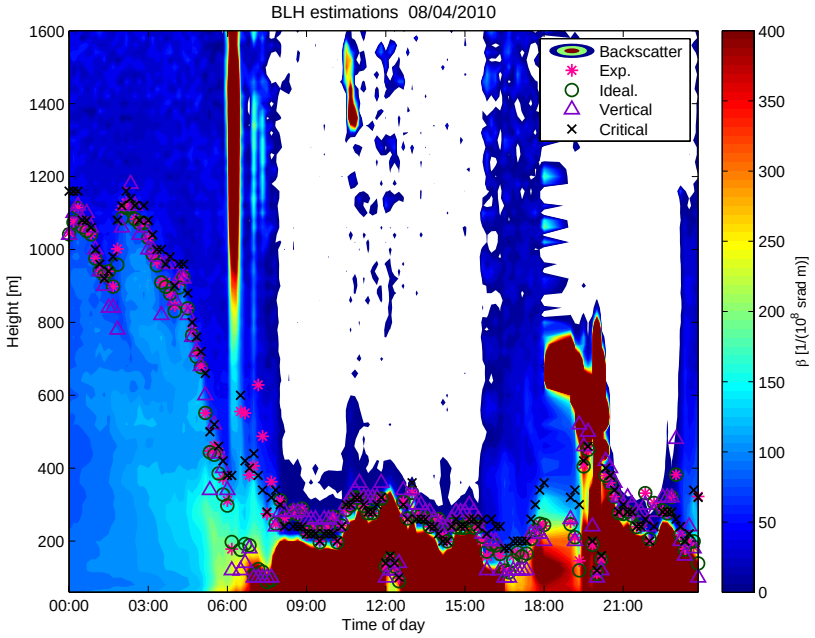


*Figure 32*: The backscatter coefficient measured with the ceilometer on April 8 2010. The coloured shading indicates the intensity of the backscattered light, blue shading indicates minimal scattering and white indicates negative backscatter values. BLH estimates indicated by different shapes and colours.

Figure 32 shows the backscatter intensity measured with the ceilometer on this day. The intensity is generally high close to the surface from around 7:00 below 400 m, indicating a fog layer or a low precipitating cloud. A higher cloud layer is also present at around 20:00. It is clearly illustrated how dense clouds or fog affect the intensity detected by the receiver of the ceilometer. A large amount of laser light is backscattered in the cloud layer, and less light is received from above it. The receiver becomes saturated resulting in negative backscatter intensities from above the cloud. The white colour represents this non-physical, negative backscatter. Data are also missing from 18:10–18:50, but is interpolated to keep right proportions on the time axis of the figure.

Clouds were removed before the BLH detections are made. The zero filter method is used to remove clouds and fog is removed by extrapolating the backscatter intensities from the first non-removed value. The four different BLH detection methods are shown with different shapes and colours. The methods generally show a similar BLH. A notable exception is seen around 6:00–8:00 where the vertical gradient and the idealized profile show lower BLH estimates than the two other methods. Notice how the fog layer rises right after 12:00 and is interpreted as a cloud with very low BLH due to the cloud filtering method.

In Figure 33 the inverse Obukhov length measured at 10 m and 100 m is plotted. Stable conditions are observed at 10 m from 0:00 to around 7:00, and afterwards unstable conditions are observed until around 19:00. From 19:00 near neutral conditions are observed. The stability measurements at 100 m show more neutral conditions than at 10 m and generally

[7] from www.wetterzentrale.de and www.wetter3.de

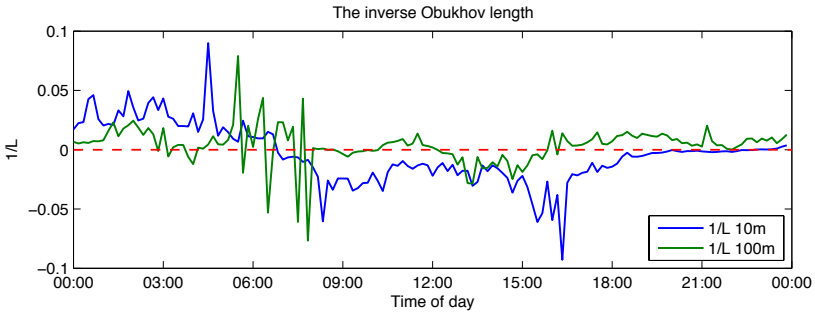


*Figure 33*: The inverse Obukhov length derived from sonic anenometer measurements at 2 m and 100 m on April 8 2010.

more fluctuations. Especially between 5:00–8:00 fluctuations in the 100 m $1/L$ values are more noticeable, right after the cold front passage. The stability at 100 m is generally more variable.

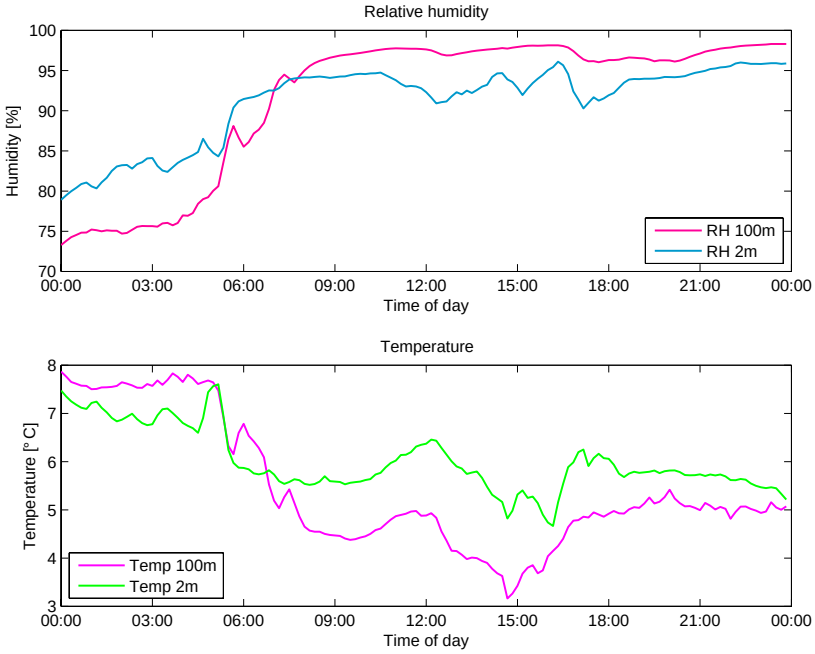


*Figure 34*: The relative humidity and temperature measured at 2 m and 100 m with the temperature and humidity probe on April 8 2010.

The cold front passage is clearly identified in Figure 34 where RH and temperature measurements at 2 and 100 m are shown. There is a clear drop in temperature at both measurement heights at around 5:00. Before that time temperature at 100 m is higher than that at 2 m, indicating stability. The RH increases rapidly at around 5:00 after which it stays high the rest of the day. At 100 m the RH is above 95% and at 2 m it is above 90%. This is the highly humid air that is commonly observed after a cold front passage.

In Figure 35 it is seen that at 0:00–3:00 the winds blow from SE. Increased wind speeds with height are observed and slight clockwise veering with height throughout the day. The wind direction changes gradually at around 4:00 and at around 5:00 westerly winds are observed. The wind speed measured at 100 m decreases slightly after the frontal passage, but increases again around 11:00 and is then north westerly. However the wind speed at 10 m increases after the frontal passage. From between 16:00–20:00 the wind directions are from

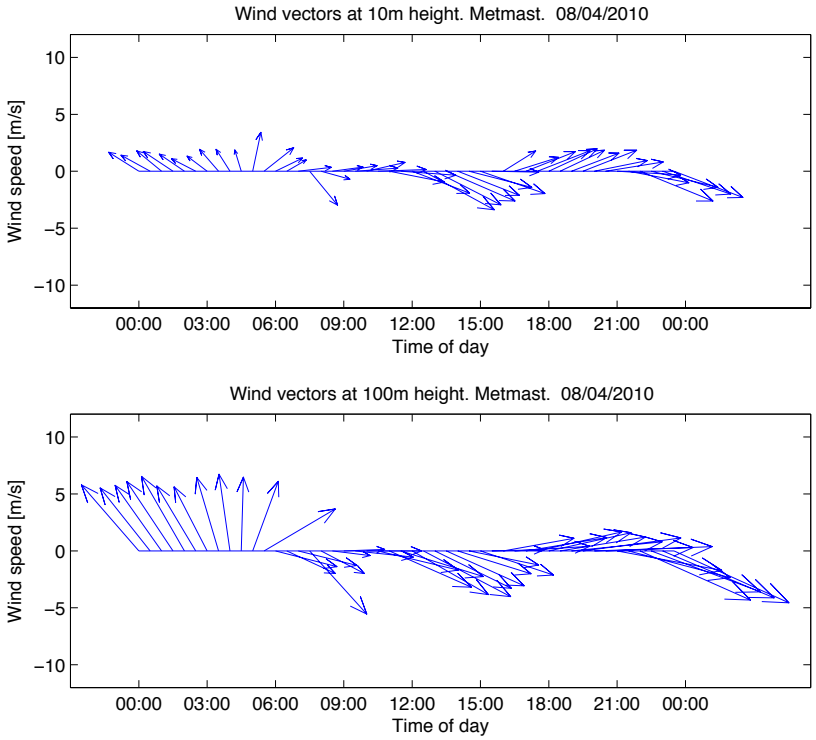


*Figure 35*: Wind speed and direction measured at 10 and 100 m with cup anemometers at the meteorological mast at Høvsøre on April 8 2010. The length of the vectors indicates the wind speed and the scale of the wind speed is shown on the y-axis. Wind direction is given by the angle of the vectors (westerly winds along the positive x-axis). For clarity only every third wind vector is shown.

south west at 10 m and turns to north westerly after that.

## 5.5 Ideal daily evolution of the ABL

On April 11 2010, ideal cloud free conditions, with easterly winds are observed. Figure 36 indicates the backscatter intensities and BLH estimates with the four different detection methods. The backscatter intensity is generally low this day. Notice the different scale on the colour bar compared with previous backscatter intensity figures. At midnight the backscatter intensity is below $40/(10^8 \text{ m srad})$ above the surface, so no BLH estimates are made. After 3:00 the backscatter intensity increases slightly. The BLH detection methods generally show a similar BLH. After 7:00 the BLH increases rapidly and reaches its maximum at ∼800 m at noon. After 18:00 the BLH begins to decrease and the residual layer is visible between 18:00–21:00.

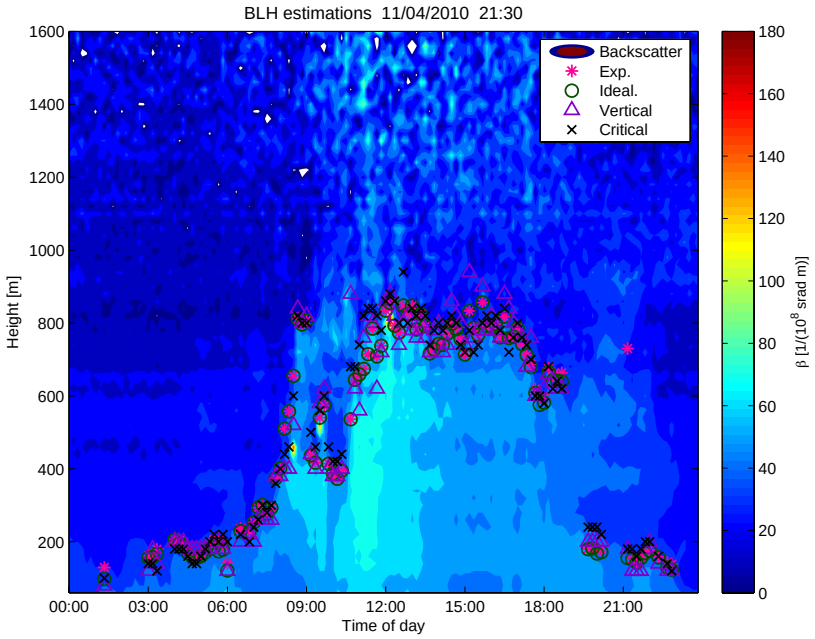


*Figure 36*: The backscatter coefficient measured with the ceilometer on April 11 2010. The coloured shading indicates the intensity of the backscattered light, blue shading indicates minimal scattering and white indicates negative backscatter values. BLH estimates indicated by different shapes and colours.

Figure 37 topmost shows the inverse Obukhov lenght measured at 10 and 100 m. From midnight to 7:00 there are observed stable conditions at 10 and 100 m, though the measurements at 100 m show large fluctuations until 2:00. Between ∼7:00–17:00 unstable conditions are observed at both measuring heights and after 17:00 both heights show stable conditions until midnight. The bottom figure shows the solar radiation from the pyranometer. Radiation values larger than 1 $\text{W/m}^2$ are measured from 5:30–19:20. The radiation peaks at noon showing values just below 700 $\text{W/m}^2$.

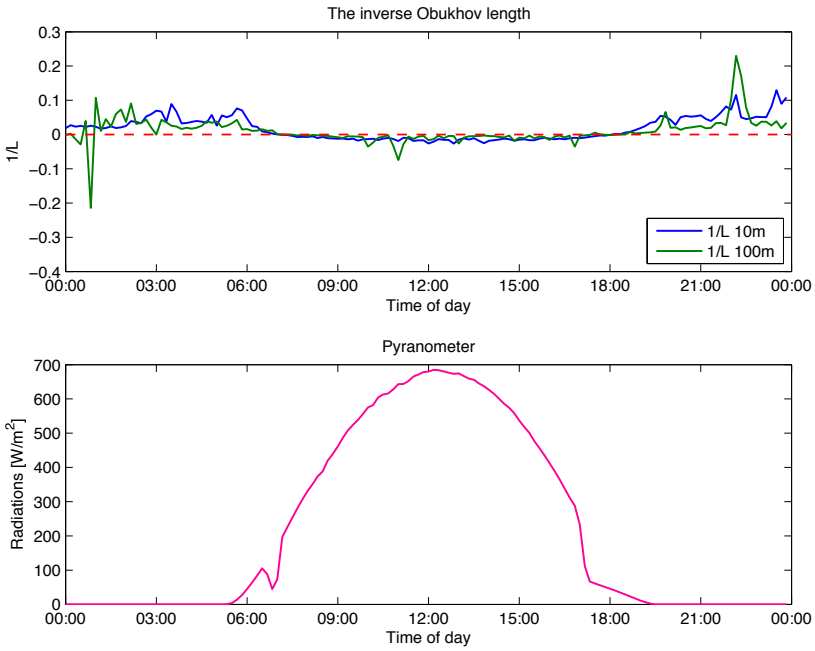


*Figure 37*: Upper: The inverse Obukhov length derived from sonic anenometer measurements at 2 m and 100 m. Lower: The solar radiation measured with the pyranometer. Measurements from April 11 2010.

## 5.6 Exponent idealized profile

Here will be studied the ceilometer data from April 16 2010. This day is chosen to specifically show the conditions where the exponent idealized profile is a clear improvement over the idealized profile. On this day winds are north westerly and wind speeds are high, reaching maximum wind speed 20 m/s at 4:00.

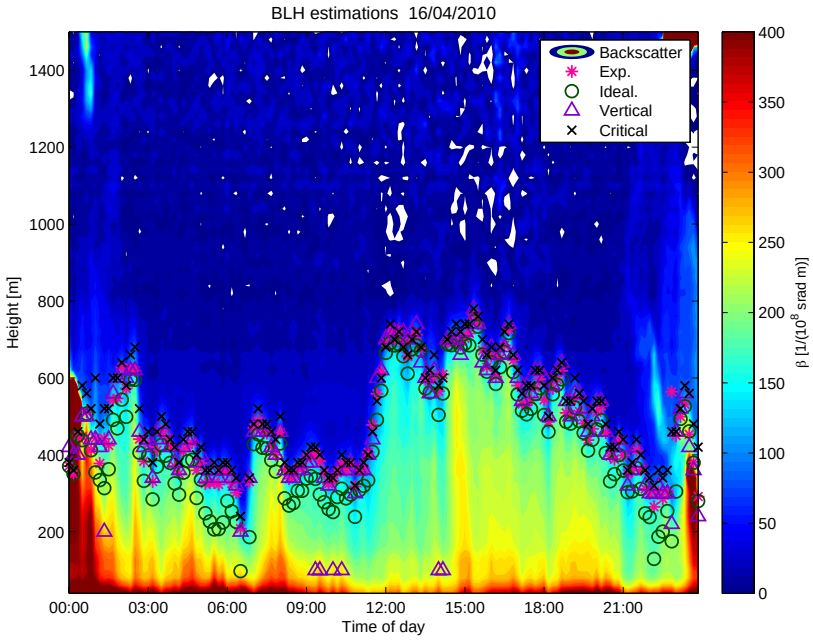


*Figure 38*: The daily evolution of the ABL on April 16 2010. The coloured shading indicates the intensity of the backscatter coefficient measured with the ceilometer. Blue shading indicates minimal scattering and white indicates negative backscatter values. BLH estimates indicated by different shapes and colours.

In Figure 38 the backscatter intensities are shown. The backscatter values are relatively high this day, generally highest near the surface. The strong winds advect relatively many marine aerosols, where the heaviest of these fall closest to the surface, resulting in high backscatter intensities. The BLH estimates deviate this particular day, where the vertical gradient detects the minimum gradient where the high surface values decrease with height. The idealized profile makes profile fits as shown in Figure 12 resulting in lower BLH than the exponent idealized profile. The exponent idealized profile and the critical threshold method show similar BLH estimates.

Figure 39 shows the wind speed and direction measured at 100 m height with the cup anemometer. The winds blow from north west the whole day with direction change with more westerly winds at the end of the day. The wind speed is relatively high this day, producing sea spray which results in relatively high aerosol backscatter values.

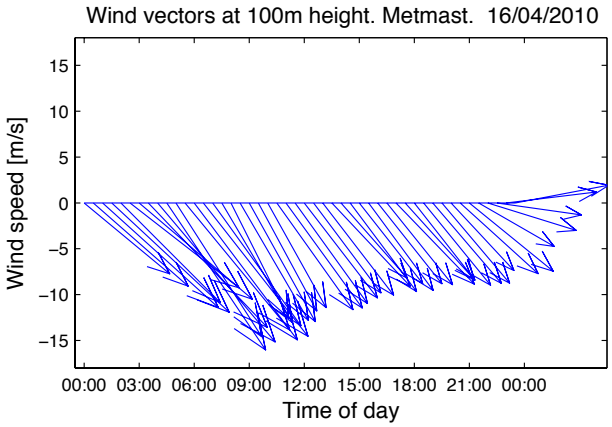


*Figure 39*: Wind speed and direction measured at 100 m with cup anemometers on April 16 2010. The length of the vectors indicates the wind speed and the scale of the wind speed is shown on the y-axis. Wind direction is given by the angle of the vectors (westerly winds along the positive x-axis).

## 5.7 Evolution of the CTBL

On June 16 2010 the marine CTBL is observed in Høvsøre. Figure 40 shows the wind speed and direction measured at 10 m height with the cup anemometer and at 300 m with the wind lidar. The winds blow from north west the whole day with slight direction change with more westerly winds during the day. The wind speed is generally higher at 300 m but the wind direction is approximately the same at both measuring heights.

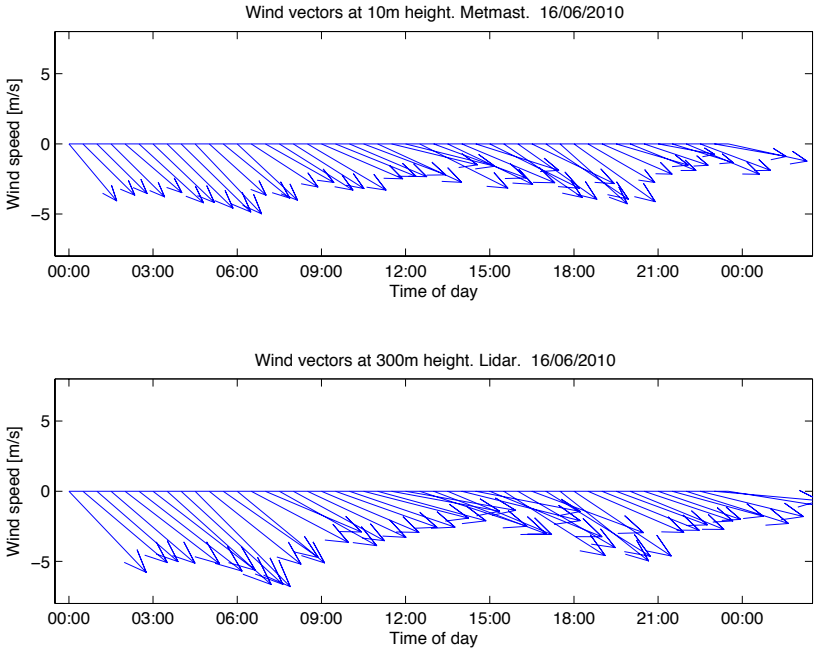


*Figure 40*: Wind speed and direction measured at 10 m with cup anemometers and 300 m with the wind lidar on June 16 2010. The length of the vectors indicates the wind speed and the scale of the wind speed is shown on the y-axis. Wind direction is given by the angle of the vectors (westerly winds along the positive x-axis).

Figure 41 topmost shows the inverse Obukhov length measured at 10 m and 100 m. From midnight to 6:00 there are observed stable conditions at 10 m and slightly unstable conditions at 100 m, though the measurements at this height are fluctuating. From 6:00–19:00 unstable conditions are observed at both measuring heights and afterwords neutral conditions are measured the remainder of the day. The lower figure shows the solar radiation from the pyranometer. Positive radiation is measured from ∼4:00–21:00. The radiation peaks between 12:00 and 13:00 showing values above 900 W/m$^2$. The radiation profile is fluctuating due to the cloud cover and its changing thickness.

Figure 42 topmost shows the RH measurements measured at 2 m and 100 m. At midnight the RH at 2 m is right below 85% and 80% at 100 m. After 7:00 the RH at 100 m is $\sim 2.5\%$ above the RH at 2 m and the profiles follow each other. Both profiles reach a minimum at 13:00, whereafter they increase through the day reaching $\sim 90\%$ RH. Figure 42 bottom shows the temperature measurements at 2 m and 100 m. The temperature at 2 m increases rapidly after sunrise (compared to the pyranometer) from ∼9.5–13°C at around noon. The temperature decreases after sunset just below 12°C and stays approximately constant the rest of the day. The temperature profile at 100 m shows less daily evolution showing an increase of ∼1°C through the day.

In Figure 43 the backscatter intensity is shown. The intensity is relatively high above the surface up to 400–500 m between 0:00 and 5:00. Around 3:30 a cloud is visible at top of the ABL seen as strong backscatter intensities throughout the day. As the colour bar shows only

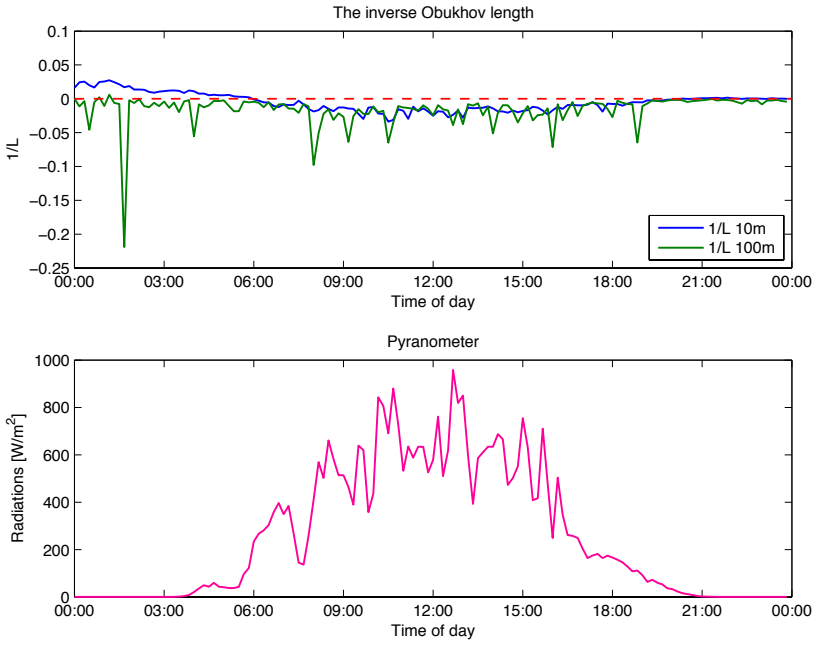


*Figure 41*: Upper: The inverse Obukhov length derived from sonic anenometer measurements at 2 m and 100 m. Lower: The solar radiation measured with the pyranometer. Measurements from June 16 2010.

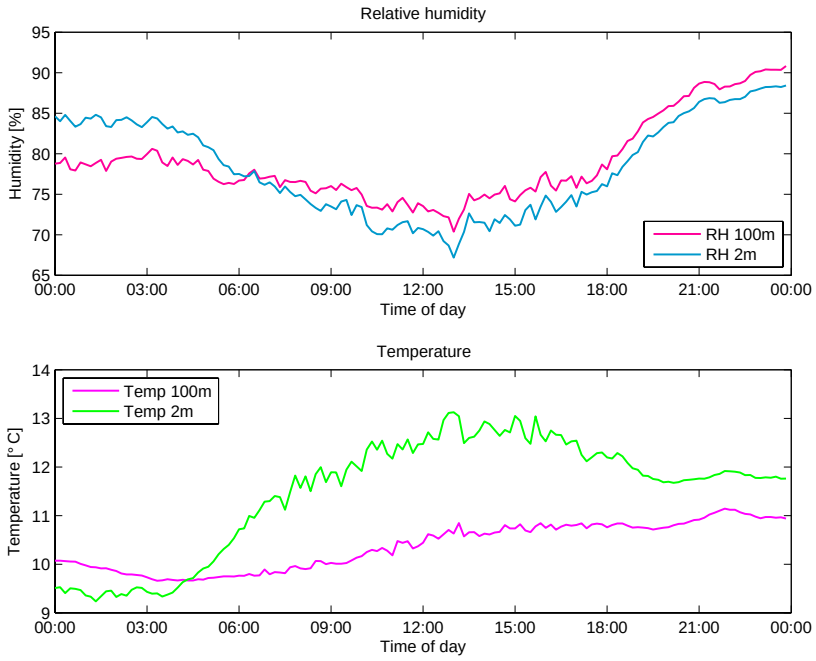


*Figure 42*: The relative humidity and temperature measured at 2 m and 100 m with the temperature and humidity probe on June 16 2010.

intensities from 0-400 the cloud is seen as intensities above $400/(10^8 \text{ m srad})$, although the backscatter signal of a cloud is typically well above $1000/(10^8 \text{ m srad})$. Between 10:00 and 19:00 the backscatter intensities are lower beneath the cloud, but higher near the surface. After the cloud appearance at 3:30 the cloud layer thickens and reaches maximum depth of ∼300 m in the afternoon. The height of the cloud layer increases from the time of the appearance to noon, where maximum height is reached. After noon the cloud layer height

decreases until midnight.

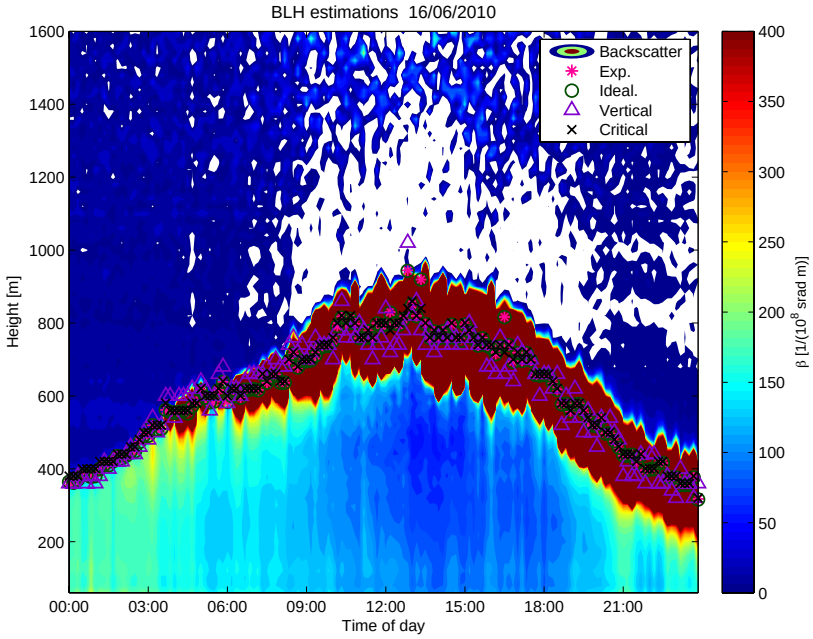


*Figure 43*: The backscatter coefficient measured with the ceilometer on June 16 2010. The coloured shading indicates the intensity of the backscattered light, blue shading indicates minimal scattering and white indicates negative backscatter values. BLH estimates indicated by different shapes and colours.

Clouds have been filtered and interpolated with a nearest neighbour interpolation. The BLH detection methods generally detect the same BLHs, except the vertical gradient deviates slightly from the other methods. The nearest neighbour cloud filtering results in a discrete change of the backscatter profile approximately in the middle of the removed cloud. As the profile fitting methods and the critical threshold detect the non-smoothed backscatter profile, these methods are prone to detect the BLH in middle of the cloud (with three exceptions of the profile fitting methods). The vertical gradient is the only method that uses the smoothed backscatter profile for BLH detection. Therefore the BLH estimates of the vertical gradient method will deviate from the other methods.

Data are available from the wind lidar this day. The standard deviations of the total wind field are used to calculate the vertical TKE profiles. The turbulence kinetic energy per unit mass is shown in Figure 44. Only signals where the CNR $\geq$ -22 dB are shown. The white area shows missing data. When compared with Figure 43 it is seen that the cut-off edge of the data follows the cloud top. Bands of strong turbulence are seen in the presence of the cloud, sometimes reaching from the first measuring height to the cloud top. In these cases the minimum TKE is at the cloud top. From 9:00–18:00 there is increased turbulence in the cloud, at heights $\sim$600–800 m. There are peaks of high TKE values at the cloud top from 9:00. There are relatively high TKE values near the surface from 9:00 to 15:00. From midnight the minimum TKE values follow the cut-off value until $\sim$7:00 where the cloud thickness has increased. After that the minima are scattered at different heights, from the near surface to cloud top.

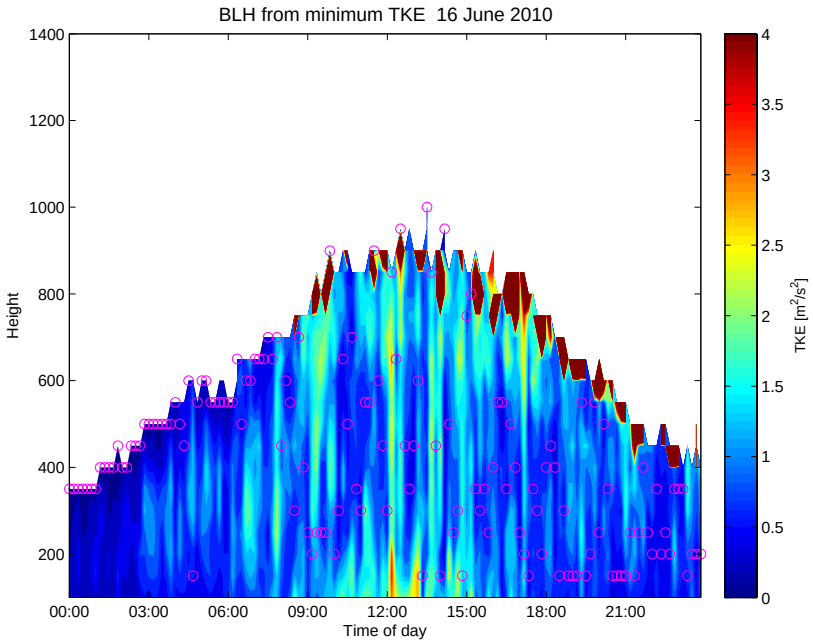


*Figure 44*: The TKE measured with the wind lidar on June 16 2010. The coloured shading indicates the strength of the TKE, blue shading indicates minimal values and white indicates missing data. Pink circles indicate BLH estimates with the minimum TKE.

## 5.8 Frequency distributions of BLH estimates

In this section frequency distributions are presented of all BLH estimates for an entire year. These are investigated to describe the variability of the BLH estimate for different atmospheric conditions, seasons and periods of time. All estimates are made using the ceilometer CL31 data from the Høvsøre database. The estimates are made with the four different BLH detection methods presented in section 4. Fog and clouds have been removed and filtered. All clouds are filtered with the zero filter explained in section 4.5 and fog is removed by extrapolating from the first non-removed backscatter value above the fog layer. The BLH detections are made from 60 up to 3000 m, starting at 60 m to partly avoid mist events. No BLH detections are made when the backscatter signal at 60 m is below $40/(10^8 \text{ m srad})$. Furthermore BLH estimates are discarded when one or more of the methods fail to detect the BLH.

In the following figures some BLH estimates are divided into different wind directions. The wind data are from the meteorological mast at Høvsøre equipped with cup anemometers at different heights. Westerly winds are defined within the range 210–330° measured at 100 m and easterly winds within 190–250°. Occasionally, winds are further divided into south west (SW), within the range 190–250° and north west (NW), within 290–350°. Some estimates are also divided into daytime and nighttime. Such periods are here depicted by using observations from a pyranometer. Daytime is defined as solar radiation values $\geq 1 \text{ W/m}^2$ and nighttime as $< 1 \text{ W/m}^2$.

#### April 2010

During this month there are relatively many days with easterly winds. This month is chosen to illustrate the different frequency distributions in westerly and easterly wind conditions.

| Method | Day mean BLH [m] | Night mean BLH [m] |
|---|---|---|
| Critical threshold | 620 | 846 |
| Idealized profile | 567 | 752 |
| Exp. ideal. profile | 608 | 795 |
| Vertical gradient | 587 | 737 |

*Table 5*: Mean BLH in the daytime and nighttime during April 2010 for easterly winds.

Figure 45 shows the frequency distribution of all BLH detections in April 2010 with easterly winds. BLH estimates are found between 0–2500 m, however only estimates up to 2000 m are shown in the figure as values above 2000 m are very rare. The vertical gradient and the critical threshold methods do not detect any BLH below 60 m because that is the starting height for the algorithm as mentioned above. The profile fitting methods on the other hand may fit a BLH below the starting height in some cases, when the backscatter gradually decreases from the first value.

The mean BLH estimates for both day and night are shown in table 5. The mean BLH is higher during the night according to all the methods. However it should be noted that the mean BLH in this case does not represent the distributions well, as it does not resemble a Gaussian distribution. The distribution is clearly multi-modal.

The nighttime BLHs shows a distinct peak at the bin centred at 225 m with the critical threshold method, and at 175 m with the three remaining methods. These peaks are the modes (the value that appears most often) of the nighttime BLH detections. Apart from the peaks the nighttime BLH estimates scatter over the whole vertical detection range, showing few estimates around 500 m. The daytime BLH estimates are mostly observed from $\sim$ 200–850 m. The threshold method shows the highest mean BLH both day and night and the

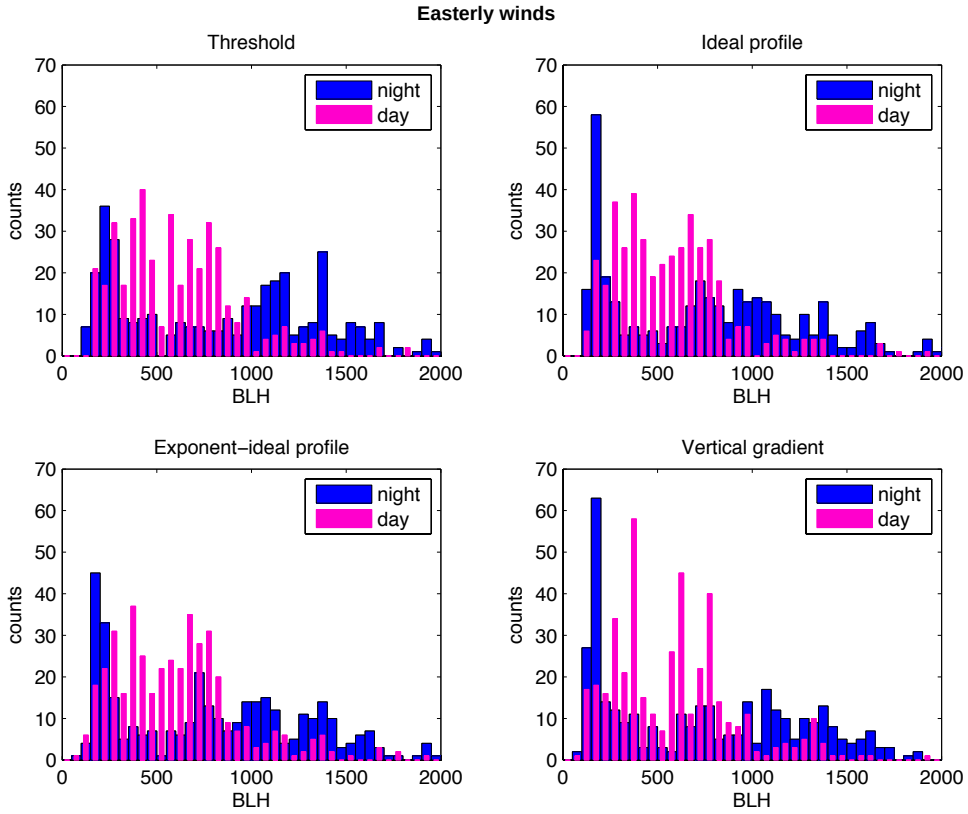


*Figure 45*: Frequency distribution of all BLH estimates in April 2010. Easterly winds, divided into day and night.

vertical gradient method shows the lowest mean BLH both day and night.
One would generally expect lower BLHs in night than daytime when the winds are easterly in ideal cloud free conditions. This is not observed since there are relatively many occurrences between 1000 and 1500 m at nighttime. The lack of the expected low night BLH and high daytime BLH is because ideal cloud free conditions with a daily evolution of the ABL as shown in Figure 1 and shown in section 5.5 are rarely observed.

| Method | NW mean BLH [m] | SW mean BLH [m] |
|---|---|---|
| Critical threshold | 515 | 420 |
| Idealized profile | 469 | 328 |
| Exp. ideal. profile | 496 | 386 |
| Vertical gradient | 470 | 326 |

*Table 6*: Mean BLH estimates for April 2010 divided into winds from SW and NW.

Figure 46 compares the BLH estimates performed when winds are from SW and NW. The estimates are found between 0 and 2260 m, but only estimates from 0–2000 m are shown as values above 2000 m are rare. The mean BLH for the two different wind conditions are shown in table 6. According to all the methods, the mean BLH is higher when the winds are from NW than that found when the wind is from SW. The sea surface temperature changes relatively slowly over the course of a month. Winds from NW are more likely to be colder than winds from SW and colder than the sea surface as well. Therefore unstable conditions occur more often resulting in generally higher BLH, when winds are from NW. The idealized profile and vertical gradient methods detect the lowest mean BLH in both wind conditions. The highest mean BLH is detected by the critical threshold method both when winds are from SW and NW. The distributions are very similar with all the methods, bi-modal distributions

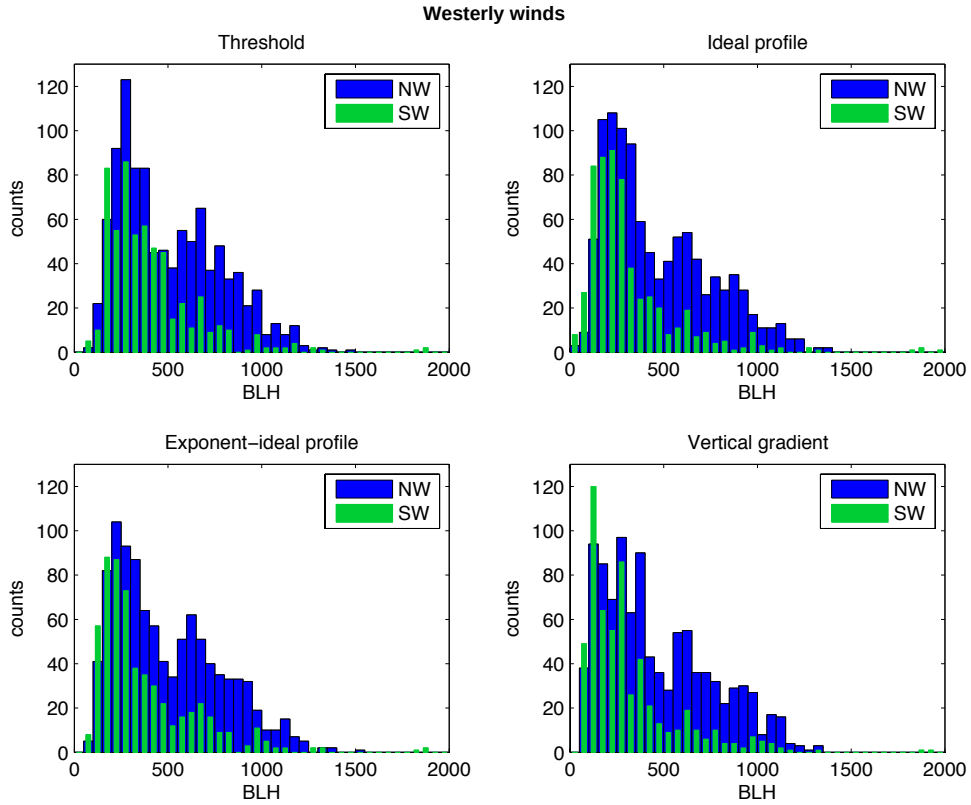


*Figure 46*: Frequency distribution of all BLH estimates in April 2010. The estimates are divided into winds from SW (green) and NW (blue).

are observed with peaks at approximately the same heights.

### May 2010

Frequency distributions for the westerly winds in May 2010 are here analysed. Easterly winds are rarely observed during this month, only in 231 out of 3310 10 min observations. Dividing the westerly wind into SW and NW shows that winds from SW only occur in 75 cases, while winds from NW occur in 2058 cases. North west is the dominating wind direction this month.

| Method | Day mean BLH [m] | Night mean BLH [m] |
|---|---|---|
| Critical threshold | 506 | 505 |
| Idealized profile | 485 | 481 |
| Exp. ideal. profile | 495 | 487 |
| Vertical gradient | 495 | 490 |

*Table 7*: Mean BLH in the daytime and nighttime May 2010 north westerly winds.

Figure 47 shows the BLH detections made when the wind direction is from west and further divided into day and night. The distributions are bi-modal but this is more clearly seen in the daytime estimates. The mean BLH estimates are approximately the same for day and nighttime, as the day and night sea surface temperature difference is small, due to the large heat capacity of the ocean mixed layer. All the BLH detection methods detect a distinct peak at 750–800 m. At 200–250 m a peak is detected for the exponent- and idealized profiles. The critical threshold method shows a peak at 250–300 m and the vertical gradient shows a peak at 350–400 m.

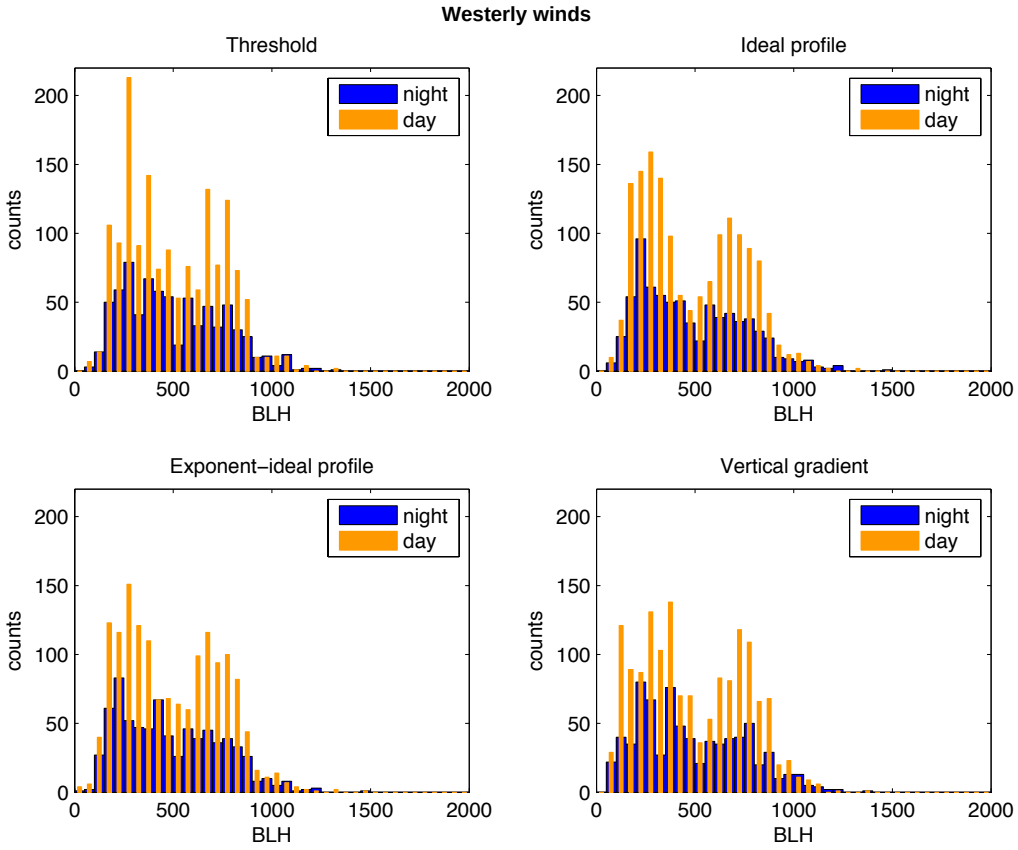


*Figure 47*: Frequency distribution of all BLH estimates May 2010 for westerly winds day and night.

| Method | Mean BLH [m] T$>9°$C | Mean BLH [m] T$<6°$C |
|---|---|---|
| Critical threshold | 275 | 690 |
| Idealized profile | 231 | 677 |
| Exp. ideal. profile | 251 | 681 |
| Vertical gradient | 219 | 688 |

*Table 8*: Mean BLH May 2010 north-westerly winds, divided in high and low temperature measured at 100 m.

As wind directions from SW are rarely observed, it is not possible to separate the bi-modal shape of the distributions can not be divided by SW and NW wind directions. Therefore another approach of division is tried by temperature measurements. Figure 48 shows the BLH estimates performed in westerly wind directions where they are divided into high temperature and low temperature measured at 100 m. High temperature is defined here as 9°C and above, low temperature as less than 6°C. The temperature measurements at 100 m are from the highest temperature sensor on the meteorological mast, and are chosen here to minimize the influence of the ground warming up during the day, to best represent the air temperature over sea. The BLH estimates are found between 0 and 1500 m. The mean BLH estimates for the different temperature criteria are shown in Table 7. All the methods clearly show higher mean BLH when the air temperature is beneath 6°C compared with the mean BLH when the air temperature is above 9°C. The BLH detection methods all show a peak at 750–800 m with the low temperature criteria. With the high temperature criteria the peaks are around 100-300 m. When the air temperature is above 9°C it is likely to be warmer than the sea surface temperature, leading to stable conditions an low BLHs. The sea surface temperature is likely to be warmer than the air temperatures below 6°C, leading to unstable conditions

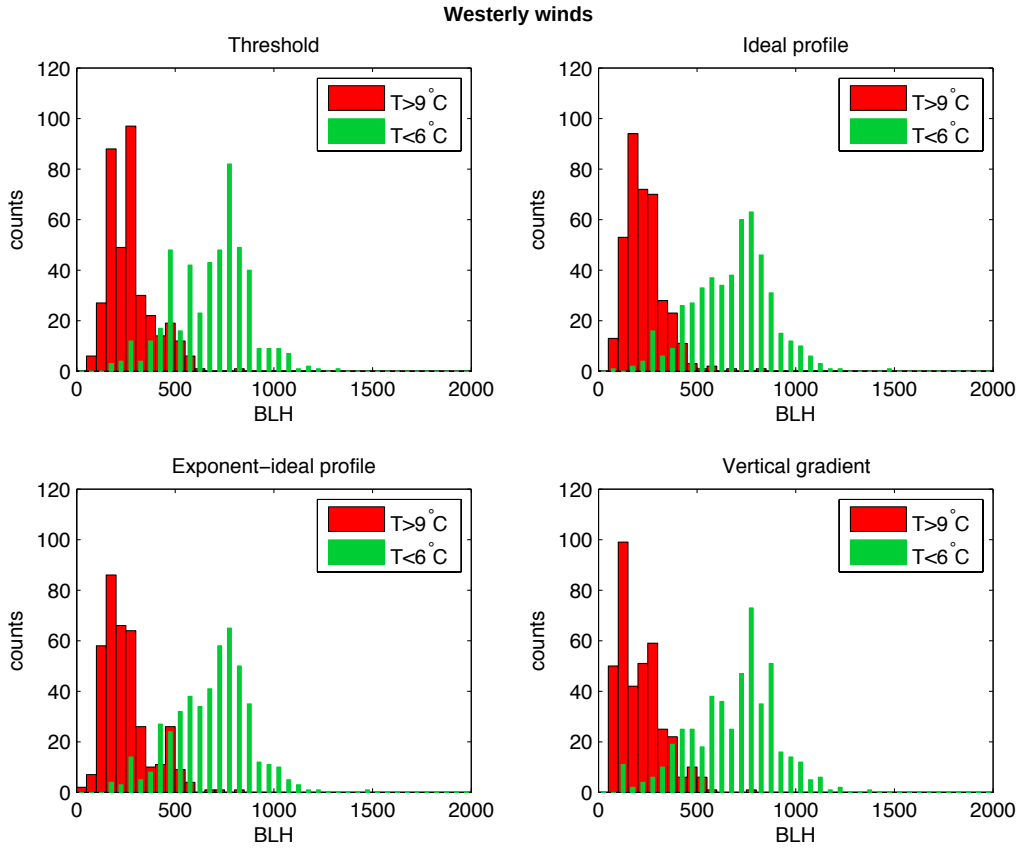


*Figure 48*: Frequency distribution of all BLH estimates May 2010, westerly winds. The BLH estimates are divided by temperature measurements at 100 m, T>9°C and T<6°C.

and higher BLHs than that found when the air temperature is above 9°C.

### October 2010

In Figure 49 the frequency distributions of the BLH estimates are seen for easterly winds divided into day and night for October 2010. The BLH detections are found between 0 and 2000 m. The four different methods all show a similar shape with generally higher BLH estimates during day than nighttime. This is what is expected since unstable conditions are more often observed during daytime. The modes of the distributions are the same for all methods; 350–400 m in the nighttime and 550–600 m in the daytime. In table 9 the mean BLH estimate for every method is shown for day and night. The mean BLH during daytime is higher than during nighttime for all the methods. The critical threshold method shows the highest mean BLH estimates both day and night. The lowest mean BLH estimates are from the vertical gradient method, both day and night.

| Method | Day mean BLH [m] | Night mean BLH [m] |
|---|---|---|
| Critical threshold | 555 | 491 |
| Idealized profile | 522 | 436 |
| Exp. ideal. profile | 527 | 457 |
| Vertical gradient | 513 | 426 |

*Table 9*: Mean BLH in the daytime and nighttime for October 2010, easterly winds.

The plots in Figure 50 shows the BLH estimates for winds from SW and from NW. The BLH estimates are found between 0–2000 m. The mean BLH for the month and for different

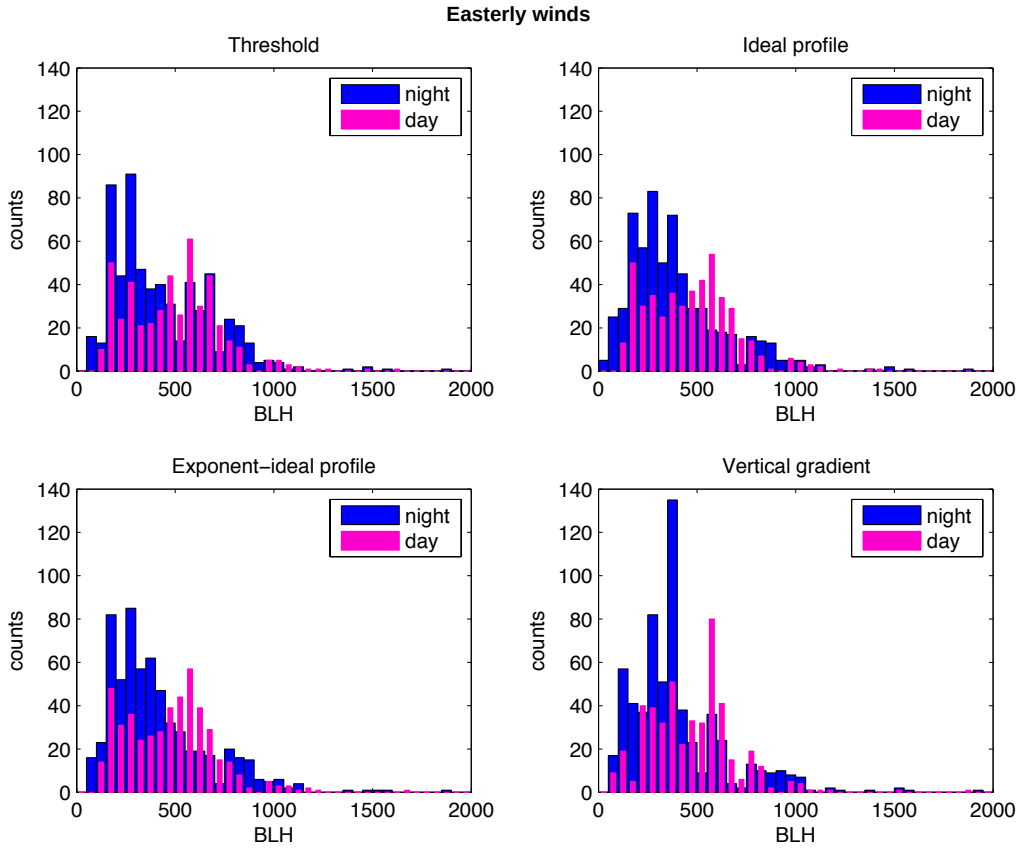


*Figure 49*: Frequency distribution of all BLH estimates during October 2010, easterly wind direction, divided in day and night.

wind directions are shown in table 10. The mean BLH is much higher when winds are north westerly according to all methods. The explanation of the higher BLHs when winds are from NW is given above for April 2010, but here the difference is more noticeable and the mean BLHs significantly higher, as the sea surface temperature is higher in October than in April. The detections of the critical threshold method show the highest mean BLH both with south westerly and north westerly winds compared with the other methods. The vertical gradient method results in the lowest mean BLH for both wind direction criteria.

| Method | SW mean BLH [m] | NW mean BLH [m] |
|---|---|---|
| Critical threshold | 633 | 884 |
| Idealized profile | 577 | 859 |
| Exp. ideal. profile | 602 | 870 |
| Vertical gradient | 558 | 826 |

*Table 10*: Mean BLH October 2010 north westerly- and south westerly winds.

### February 2011

In Figure 51 the frequency distributions of the BLH estimates are shown for easterly wind directions, divided into day and night for February 2011. The BLH estimates are found between 0 and 1800 m. The four different BLH detection methods show similar distributions and generally higher BLHs during night than during daytime. The mean BLHs are seen in Table 11 and it is seen that the nighttime BLHs are not much higher, only ∼60 m higher than the daytime BLHs. The lowest mean BLH estimates are made with the idealized profile, both day

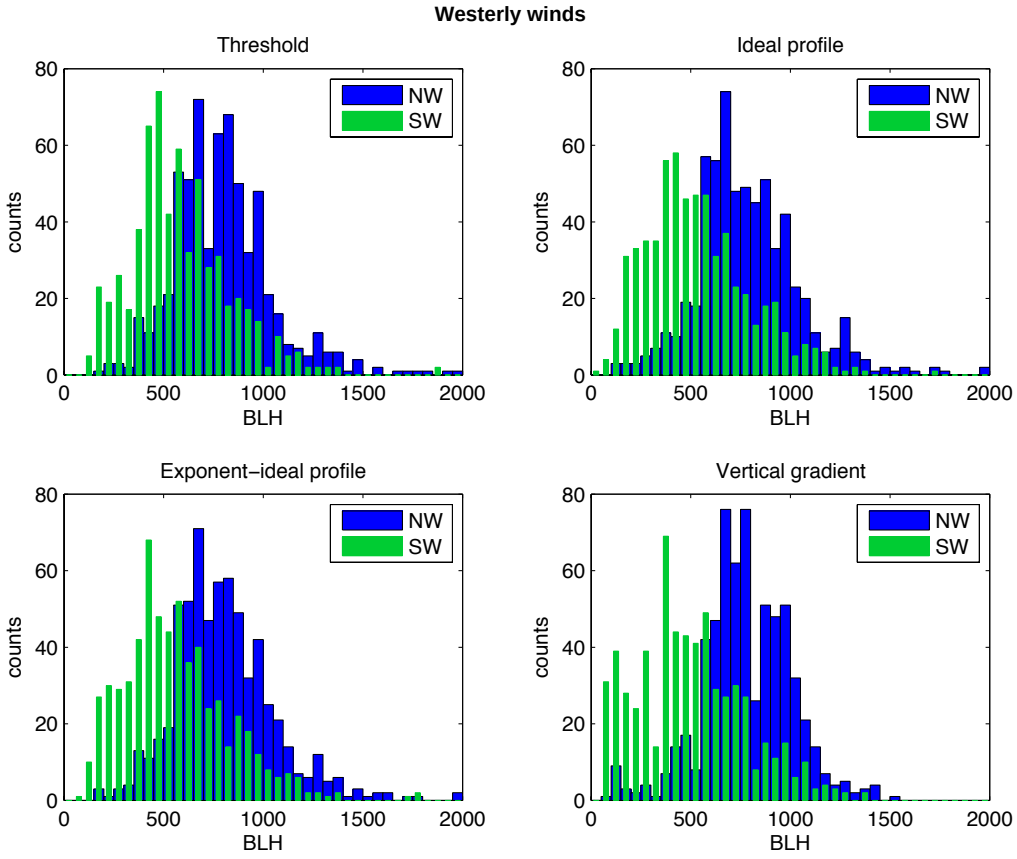


*Figure 50*: Frequency distribution of all BLH estimates for October 2010. Divided into south westerly and north westerly wind directions.

| Method | Day BLH [m] | Night BLH [m] |
|---|---|---|
| Critical threshold | 532 | 589 |
| Idealized profile | 513 | 575 |
| Exp. ideal. profile | 520 | 579 |
| Vertical gradient | 535 | 595 |

*Table 11*: Mean BLH February 2011 easterly winds, divided in day- and nighttime.

and night. The critical threshold shows the highest mean BLHs day and night.

There are some notable features of the synoptic weather situation during this month, that may explain the similar BLH distributions for day and night. The predominant wind direction is from the east, which is rarely the case at Høvsøre. February 2011 was also relatively cold, with a high pressure zone over southern Scandinavia. A cloud layer is observed most of the month ($\sim 70\%$ of observations), possibly stratus clouds, which are common near the subsidence inversion (A.W. Hansen, personal communication). Under these circumstances, stability conditions are expected to be approximately the same during day and night.

### April 2010 – March 2011

Figure 52 shows the frequency distribution for an entire year of BLH estimates in the period April 2010–March 2011 with the four different BLH detection methods. All wind directions are included. The BLH estimates are found between 0–2500 m. The figure shows the interval 0–1500 m only, as estimates above 1500 m account for less than $1\%$ of the total. The bin size is 20 m. The figure also shows a Gamma distribution fitted to each frequency distribution. The

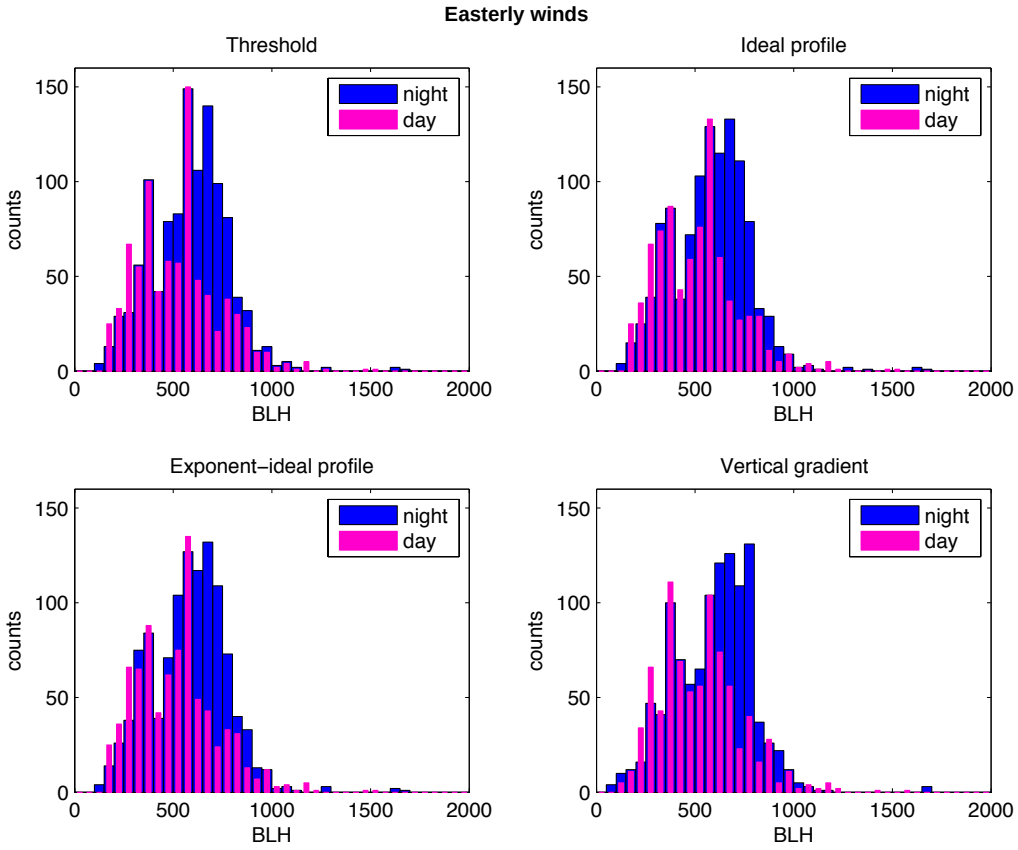


*Figure 51*: Frequency distribution of all BLH estimates for February 2011. Divided in day and night, easterly wind directions.

Gamma distribution is also used by Liu and Liang (2010) and is chosen as the distributions are positively skewed with longer tails on the right. The shape parameter, scale parameter, the mean and deviation of a Gamma distribution are given by $\alpha$, $s$, $\alpha s$ and $\sqrt{\mathrm{k}}\mathrm{s}$ respectively and are seen in Table 12. The highest mean BLH (516 m) and lowest deviation (273 m) is estimated by the critical threshold method. The lowest mean BLH (473 m) is estimated by the vertical gradient method and the largest deviation (309 m) is found by the idealized profile method.

The frequency distribution of BLH estimates with the critical threshold method follows the Gamma distribution well except at height ranges about 180–280 m, 600 m, 680 m and 800–840 m, where the histogram occurrences exceed the Gamma distribution. In between these peaks there are lower occurrences. The idealized profile frequencies show lower occurrences than the Gamma distribution from 20–100 m. At height ranges about 180–300 m and 560–640 m the histogram occurrences exceed the distribution. The exponent idealized profile distribution shows slightly lower occurrences than the Gamma distribution at height ranges about 20–100 m and 320–540 m. From 160 m to 240 m the the histogram occurrences exceed the distribution. The vertical gradient method distribution shows a distinct peak at 120 m and a clear drop at 160 m. This peak is due to the many BLH detections by the method when the backscatter intensities are relatively strong near the surface (where the exponent idealized profile fits the exponential function). Apart from this distinct peak the shape of the distribution is similar to the critical threshold method, though the peaks are not at the exact same heights. The histogram occurrences exceed the Gamma distribution around heights 100–120 m, 200–260 m, 600–640 m and 720–780 m.

The peaks that are clearly seen in the frequency distributions of the BLHs estimated with the critical threshold method and the vertical gradient method are due to a wave pattern

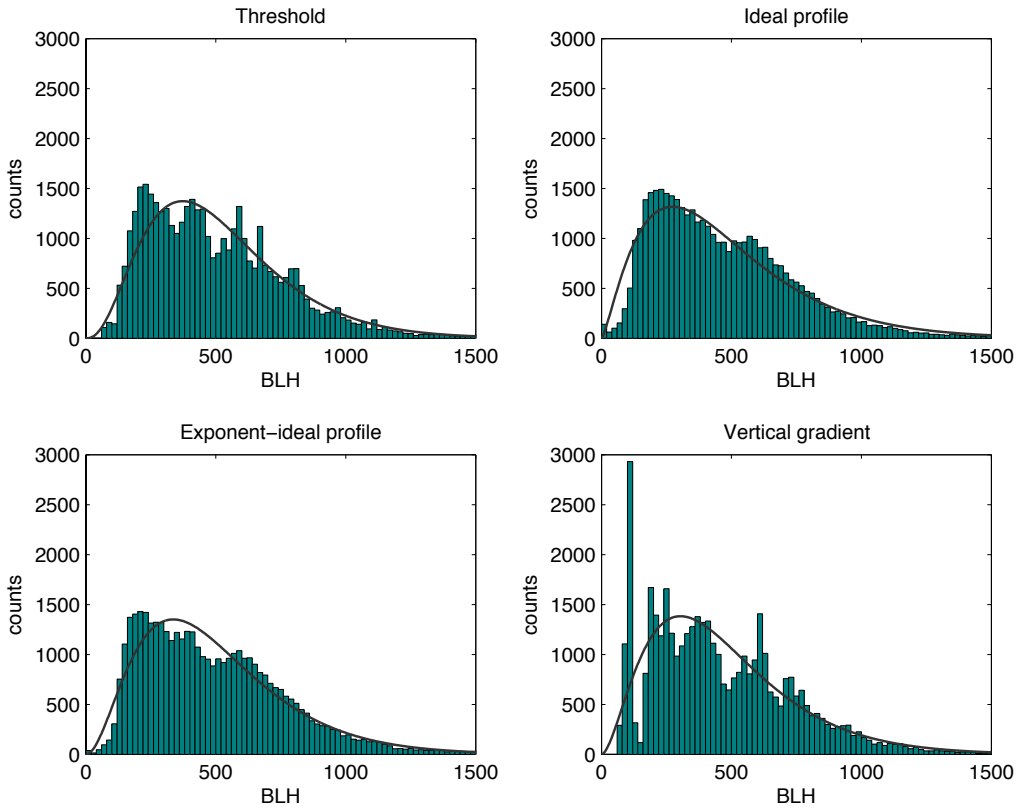


*Figure 52*: Histogram of all BLH estimates between April 2010–March 2011. The bars show the histograms and the solid black line shows a fit using a Gamma distribution.

| Method | $\alpha$ | $s$ | $\alpha s$ | $\sqrt{\alpha}$s |
|---|---|---|---|---|
| Critical threshold | 3.59 | 144 | 516 | 273 |
| Idealized profile | 2.36 | 201 | 475 | 309 |
| Exp. ideal. profile | 3.07 | 162 | 498 | 284 |
| Vertical gradient | 2.80 | 169 | 473 | 283 |

*Table 12*: The shape parameter ($\alpha$), scale parameter ($s$), mean ($\alpha s$) and deviations ($\sqrt{\alpha} s$) found by a Gamma fit of all BLH estimates during April 2010– March 2011.

in the vertical backscatter profiles. The wave pattern is visible in the density plots as weak horizontal 'bands' e.g. in Figures 27(a) and 36, where the backscatter intensities are relatively weak. The BLH estimates tend to converge to the regions where the backscatter signals are weaker due to the wave pattern. According to Schäfer et al. (2004) this wave pattern is caused by a small disturbance in the receiver electronics. They worked with a Vaisala CT25K ceilometer and removed the wave pattern with an algorithm that subtracts the pattern from every backscatter profile.

Figure 53 shows the frequency distribution of BLH estimates in the period April 2010 – March 2011, easterly winds only and further divided into day and night. The BLH estimates are found between 0–2500 m. The figure shows the interval 0–1500 m, as estimates above 1500 m make $\sim$1% of the total. The bin size is 20 m. The figure also shows a Gamma distribution fitted to each frequency distribution. The shape parameter, scale parameter, the mean and deviation of a Gamma distributions are seen in Table 13. The mean BLHs estimated in daytime are generally slightly higher than the nighttime BLH estimates, except for the critical threshold method which shows the same mean BLHs day and night.

The frequency distributions do not follow the Gamma distribution as well as in the case

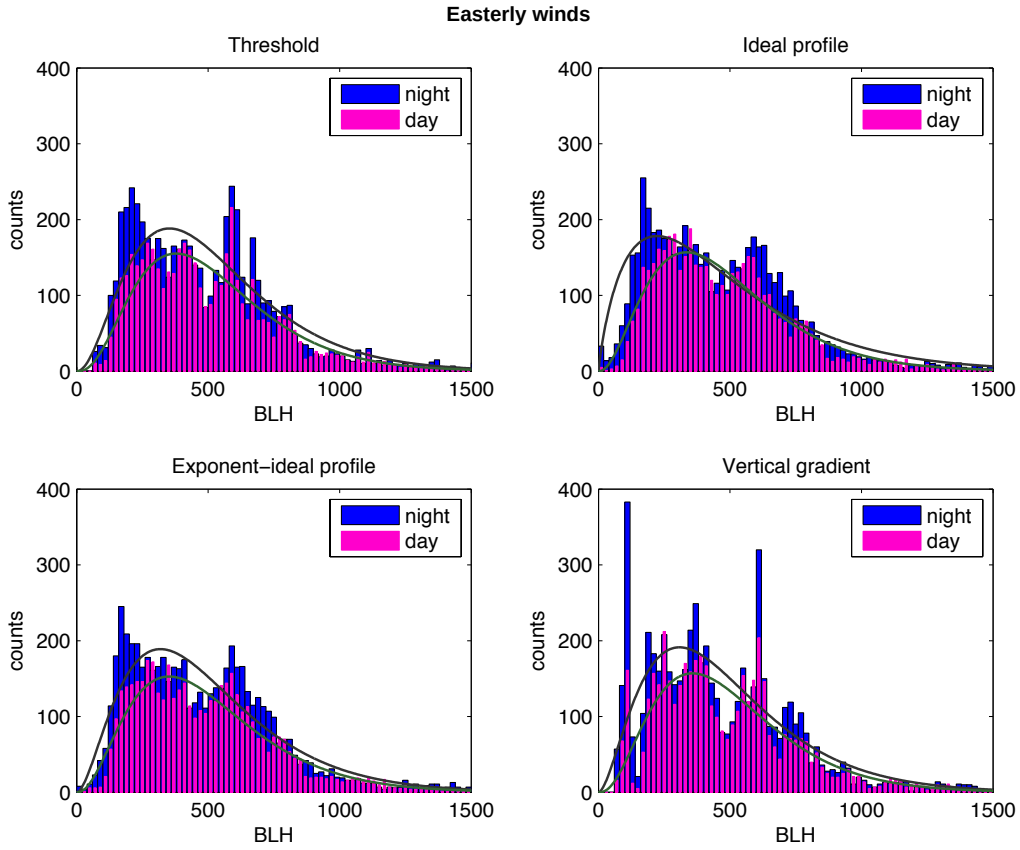


*Figure 53*: Histogram of all BLH estimates from April 2010 – March 2011 for easterly winds divided in day- and nighttime.

of all wind directions. The nighttime histogram occurrences exceed the Gamma distribution at heights around 200 and 600 m. The vertical gradient shows distinct peaks at 120 and 620 m. All four methods show a distinct drop in the BLH estimates around 500 m and lower occurrences than the Gamma distribution both day and night. A multi-modal distribution might perform a better fit to the histograms particularly during nighttime. The reason for the fewer occurrences around 500 m is unknown.

| | Day | | | | Night | | | |
|---|---|---|---|---|---|---|---|---|
| Method | $\alpha$ | $s$ | $\alpha s$ | $\sqrt{\alpha}$s | $\alpha$ | $s$ | $\alpha s$ | $\sqrt{\alpha}$s |
| Critical threshold | 3.76 | 137 | 515 | 266 | 3.18 | 162 | 515 | 288 |
| Idealized profile | 3.24 | 150 | 484 | 269 | 1.87 | 256 | 479 | 350 |
| Exp. ideal. profile | 3.34 | 151 | 502 | 275 | 2.82 | 175 | 494 | 294 |
| Vertical gradient | 3.54 | 141 | 499 | 265 | 2.75 | 176 | 484 | 292 |

*Table 13*: The shape parameter ($\alpha$), scale parameter ($s$), mean ($\alpha s$) and deviation ($\sqrt{\alpha}s$) found by a Gamma fit of all BLH estimates during April 2010– March 2011. Easterly winds only, divided into day and nighttime.

Figure 54 shows the frequency distribution of BLH estimates in the period April 2010 – March 2011 where wind directions are from SW and NW. The BLH estimates are found between 0–2500 m. The figure shows the interval 0 – 1500 m, as estimates above 1500 m make up 0.4% of the total. The bin size is 20 m. The figure also shows a Gamma distribution fitted to each frequency distribution. The shape parameter, scale parameter, the mean and deviation of a Gamma distribution are given in Table 14. The mean BLHs are generally higher when the wind direction is from NW shown by all four BLH detection methods.

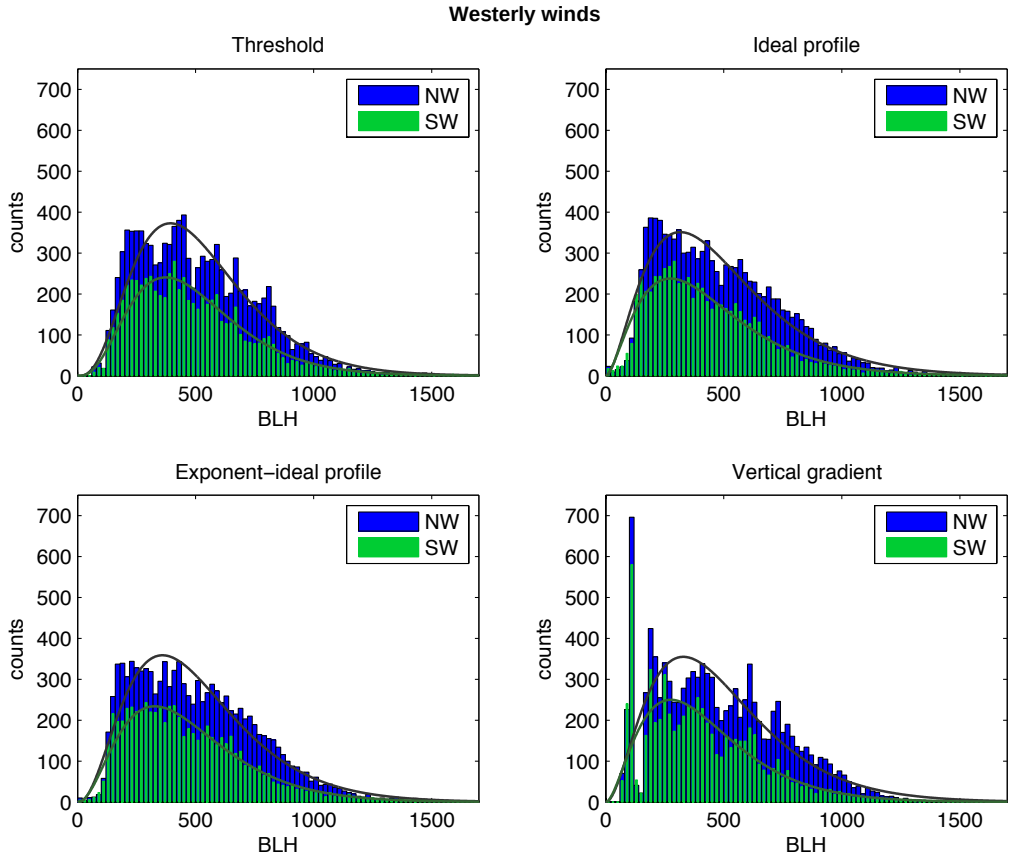


*Figure 54*: Histogram of all BLH estimates from April 2010 – March 2011, divided in south westerly and north westerly wind directions.

| | South west | | | | North west | | | |
|---|---|---|---|---|---|---|---|---|
| Method | $\alpha$ | $s$ | $\alpha s$ | $\sqrt{\alpha}$s | $\alpha$ | $s$ | $\alpha s$ | $\sqrt{\alpha}$s |
| Critical threshold | 4.04 | 123 | 496 | 247 | 4.06 | 129 | 522 | 259 |
| Idealized profile | 2.67 | 164 | 438 | 268 | 2.81 | 174 | 490 | 292 |
| Exp. ideal. profile | 3.24 | 146 | 472 | 262 | 3.40 | 150 | 509 | 276 |
| Vertical gradient | 2.85 | 149 | 424 | 252 | 2.99 | 165 | 494 | 286 |

*Table 14*: The shape parameter ($\alpha$), scale parameter ($s$), mean ($\alpha s$) and deviation ($\sqrt{\alpha}s$) found by a Gamma fit of all BLH estimates during April 2010– March 2011. South westerly and north westerly winds.

The frequency distributions follow the Gamma distribution well, but the histogram occurrences slightly exceed the Gamma distribution around 200 m. The influence of the wave pattern of the backscatter profiles on the BLH estimates is seen, especially on the distributions with the critical threshold and the vertical gradient methods. A distinct peak is seen around 120 m with the vertical gradient method, with both wind direction criteria.

## 5.9 Intra-annual variation

The BLH estimates made with the four different BLH detection methods are used to derive a monthly variation of the mean BLH. Figure 55 illustrates the mean BLH estimated in westerly and easterly wind conditions. The four different methods show very similar curves. This analysis shows generally the highest BLH estimates with the critical threshold method and the lowest with the vertical gradient method. The exponent idealized profile tends to show higher BLH estimates than the idealized profile method.

All the BLH detection methods show the highest mean BLH in November when winds are predominantly from the west. The mean BLH in westerly winds increases from June to November. The high BLHs in the autumn may be explained by the temperature difference of the air and sea surface. The relatively warm sea surface in autumn may lead to unstable conditions with deep boundary-layer observations.

The curves showing the mean BLHs in easterly wind conditions are more fluctuating compared with those for westerly winds. The BLH detection methods all show the highest mean BLH in April 2010. From October 2010 to January 2011 the mean BLH estimates are generally low and decrease slightly throughout the period.

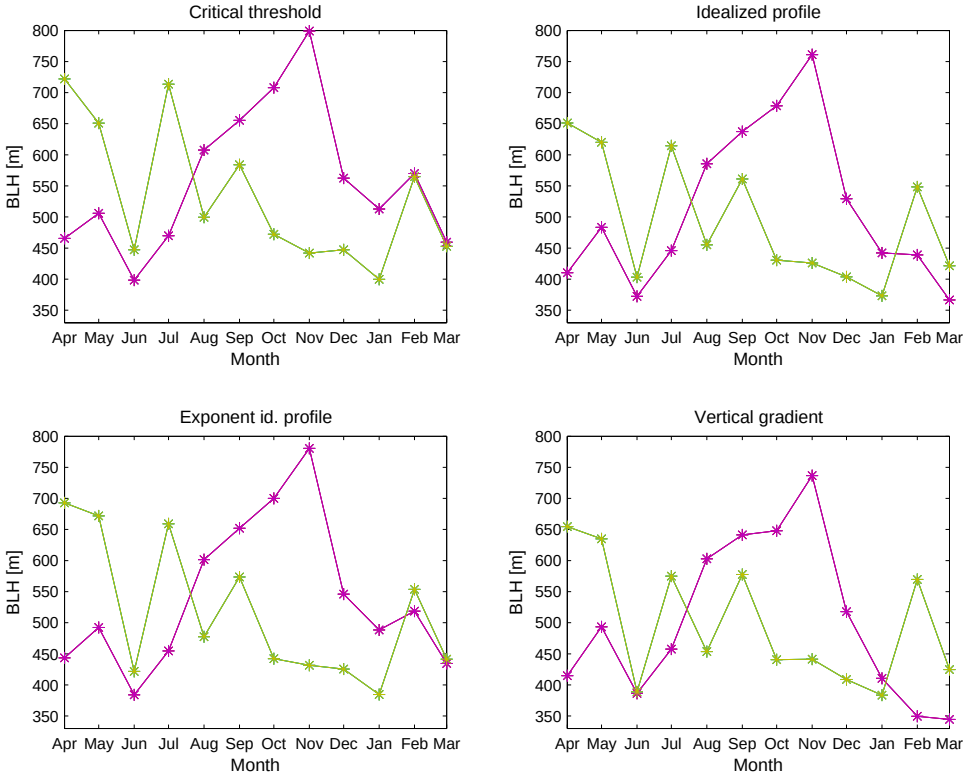


*Figure 55*: Intra-annual variation of the BLH estimates from April 2010 – March 2011. The green line denotes the easterly wind BLH estimates and the purple line denotes the westerly wind BLH estimates.

# 6 Discussion

In this section, a discussion of key results of the investigations from sections 4 and 5 are discussed.

### Clouds

The presence of clouds complicates the BLH detection with a ceilometer. It is illustrated in section 5.1 how decoupled and high clouds still influence the detection algorithms. The BLH detections are associated with the cloud layer and the different methods detect the BLH at different heights. It should be noted that the critical threshold method is not influenced by decoupled clouds, as the BLH is found at the first height below the critical threshold value. However all the BLH detection methods are influenced by a CTBL, in which case there is no scientific consensus on how to define the BLH. The reason for this is partly because there is a continuum of behaviour of a CTBL, from thin stratus or fair weather cumulus to deep convective clouds at the top of the ABL (Grimsdell and Angevine, 1998).

The zero filtering method proves to be most robust. With this method it does not matter if the cloud has diffuse boundaries that do not get removed, as the detection method consistently estimates the BLH at cloud base. Also the BLH estimates are relatively stable, compared with the other filtering methods, when the cloud thickness varies rapidly as seen in Figure 20. As mentioned in section 2.7 the BLH definition at cloud base corresponds well with a relatively well mixed layer.

### BLH detection methods

The critical threshold method is very simple and not computationally heavy. The values, $\beta_{crit}$ and $\beta_m$ are chosen by trial and error and different values may be applied. The vertical gradient is a relatively simple approach, not computationally heavy, but does rely on smoothing of the vertical profile. This method is sensitive to noise and variations, e.g. the frequently observed high aerosol backscatter values near the surface. The profile fitting methods are more computationally heavy and they rely on an initial guess. This guess does not have to be accurate, especially if lower and upper bounds are set on the fitted variables. The methods are not sensitive to noise and fluctuations. The wave pattern in the backscatter profiles does not seem to influence the BLH estimations as with the critical threshold and vertical gradient. This is seen in Figure 52. The two profile fitting methods give very similar results as the methods are similar. The advantage of the exponent idealized profile is that a better fit is often accomplished when winds are westerly and aerosol backscatter values are strong close to the surface. The method may also result in better fits to aerosol backscatter profiles in stable conditions, where the aerosol content is highest immediately above the surface and gradually decreases. The weakness of the exponent idealized profile method compared to the idealized profile method is that it is more computationally intense.

### Wind lidar comparison

It should be noted that wind lidars are generally not capable of measuring turbulence accurately compared with sonic anemometer measurements. The wind velocity variance measurements show systematic errors due to the measuring volume and the scanning pattern of the

wind lidar (Sathe et al., 2011). However, as the absolute value of the TKE is not important but only the height of the minimum TKE, the turbulence measurements of the wind lidar are assumed to be valid for this study.

It is seen how the correlation coefficients are sensitive to outliers and how removing the outliers greatly improves the correlations. Applying a more sophisticated detection algorithm to the TKE calculations, thereby reducing the number of BLH detections in the residual layer, would improve the method and correlations. The inter-comparison shows that the two methods correspond well with each other showing significant correlations on a 99.9% confidence level. This may partly be explained by the height of the cut-off value of the wind lidar data. The retrieved data of the wind lidar is dependent on the aerosol content of the atmosphere and the height of the cut-off value does not often exceed the BLH estimate from the ceilometer data. This influences the comparisons, improving the correlations.

**Frontal passage**

It is seen from the figures in section 5.4 that a frontal passage greatly influences the weather and the BLH detections on the site. The stability measurements indicate stable conditions near the surface before the cold front passage. The height of a SL is typically 200–300m (Peña et al., 2010). However the detected BLHs are relatively high ∼1000 m. One explanation for these high nighttime BLH estimates may be homogeneously distributed aerosols between the stable and residual layer. In such a situation there is no clear gradient of the aerosol backscatter found in the ceilometer data at the top of the SL (Milroy et al., 2012). However it is not likely that the high backscatter values and homogeneously distributed aerosols would persist for a whole night. This effect is usually observed for a few hours right after sunset as seen in section 5.5. Another possible explanation is described by Sinclair et al. (2012) where a nocturnal cold front passes southern Finland. In this case the BLH is observed ∼800–1000 m in the warm sector ahead of the cold front, and a lower BLH is detected in the cold postfrontal air. The vertical wind shear is larger ahead of the front than behind, both for model outputs and observations. Therefore a deep BLH ahead of the front is most likely due to increased shear-driven turbulent mixing. This explanation may very well apply to the Høvsøre case, as the conditions are similar in many ways. Both are nocturnal frontal passages in the mid-latitudes, moving eastward from sea over land. The vertical wind shear in Høvsøre cannot be estimated up to the estimated BLH, but the vertical wind shear is large up to 100 m, which may be seen in Figure 35 from the low wind speeds measured at 10 m compared to the wind speeds measured at 100 m in the warm sector ahead of the cold front. It is not possible to distinguish between low precipitating clouds and fog from the ceilometer data. In both situations high backscatter values are observed from the first measuring height to the cloud/fog-layer height. After the cold frontal passage the high backscatter signals near ground most likely indicate low precipitating clouds. The difference in cloud and fog filtering in the automatic BLH detection results in a sudden jump in BLH estimates just after 12:00, when the fog/low cloud layer rises above ground and is filtered as a cloud. The BLH detections then show the cloud base. In this situation it would be preferable to choose another cloud filtering method.

**Ideal conditions**

The wind direction is from north east (not shown here) the whole day. The BLH estimates show a low stable layer before sunrise. The boundary-layer growth coincides well with the solar radiation and stability measurements. The BLH decrease in the evening does not coincide as well with the solar radiation and stability measurements. Stable conditions are measured after 18:00, but the BLH estimates first decrease to ∼200 m around 20:00. This is the effect of unchanged aerosol content in the residual layer around sunset, as mentioned in section 4. After 20:00 only one BLH estimate detects the residual layer around 21:00. This is the exponent idealized profile, which is expected to detect the residual layers more often, because of its

variable profile fitting. Surprisingly few of these ideal boundary-layer evolutions are observed at Høvsøre. The reason is mainly twofold: First the ideal conditions with high pressure, no clouds and easterly winds are rarely present during a whole day. Second, the ceilometer has difficulties detecting the backscatter when either the aerosol concentration or RH is low which is frequently observed for easterly winds.

### Evolution of the marine CTBL

On this day the wind is predominantly north westerly and the marine ABL is observed. Although stable conditions are measured at 10 m in Høvsøre from midnight until morning, this does not influence the marine ABL. The stability conditions on land influence the internal boundary layer in Høvsøre and using equation 8 the internal boundary layer is likely to be $\sim$100–240 m, as the fetch is $\sim$2.4 km when winds are from north west.

It is seen from the stability measurements how the cloud layer affects the stability at the surface. During nighttime stable conditions are observed in cloudless conditions, but neutral conditions are observed in the presence of clouds.

The daily evolution of the BLH during the day is not likely to be caused by a increase/decrease in sea surface temperature, because of the large heat capacity and mixing within the top of the ocean. Possible mechanism causing the increase in the BLH is instability of near surface air at sea and cloud top entrainment instability (Garratt, 1992; Stull, 1988). It is seen that the BLH increases from midnight, before the onset of the cloud, until around noon. The wind flow is from north west and the air is likely to be colder than the sea surface temperature leading to instability. The measured Obukhov length at 100 m indicates instability before the cloud appearance, although the measurements are fluctuating. These measurements might indicate instability over the sea if the internal boundary layer is less than 100 m.

The ceilometer clearly observes a cloud cover from around 3:30. Despite the cloud cover the solar measured radiation shows very high values, especially a peak above 900 W/m$^2$ around 13:00. This may be an indication of partially clear sky inbetween the observed clouds. However the cloud cover appears constant in the ceilometer data as a result of the 10 minute averaging. Increased TKE is seen near the surface around noon, due to the surface warming of the sun. The inverse Obukhov length at 10 m indicates instability near the surface.

Entrainment of dry, warm air from above into the cloud may lead to evaporative cooling and the air will sink. This mechanism causes warming and drying of the mixed layer beneath the cloud and causes the cloud base to rise. This possibility could be supported by the low RH measurements at around 13:00. The bands of high TKE reaching from the cloud top through the whole mixed layer also indicates this process. After noon the wind flow is more directly from west and the stability measurements indicate neutral conditions after 19:00. The temperature measurements at 100 m show a slightly increasing temperature after 19:30 indicating warmer air being advected after the wind direction change and more stable conditions over the ocean. It is clearly illustrated in Figure 44 how the minimum TKE method is not suitable for BLH detection in cloudy conditions, where the minimum TKE values scatter between the first measuring height and the cloud top, after the presence of a cloud around 06:00.

### Frequency distributions

The division of BLH estimates into day and nighttime with easterly winds shows surprisingly small differences. The nighttime distribution for October shows a peak around 200 m, but relatively many BLH detections $\sim$800–1500 m, resulting in a higher mean BLH in night than daytime. This month is typical in the sense that the same kind of distributions for other spring and summer months look very similar, though they are not shown here. It is seen from the yearly distributions in Figure 53 that the nigthtime occurrences exceed the daytime occurrences around 200 m, otherwise the day and nighttime distributions are very similar.

There are many challenges when detecting the BLH in easterly winds. There is not a single or simple reasons for these high BLH estimates detected in nighttime seen in the frequency

distributions. It is clear that the synoptic weather has a profound influence on the ABL structure and BLH, as illustrated in the case study in section 5.4. Also when the aerosol content is low and the RH less than 80% the measured aerosol backscatter signals are very low, often too low to distinguish a clear vertical backscatter profile. In this situation the BLH detection methods will mostly fail to detect the BLH correctly. Cloud layers at nighttime often result in associated BLH detections in the cloud layer. Although it is questionable if a SBL can form in the presence of a cloud layer, as radiative cooling is reduced. It cannot be determined from the ceilometer data alone if the ABL and cloud layer are fully coupled and the BLH detection associated with the cloud layer is correct. Another contribution that has already been mentioned is when there is a clear signal, it is not always possible to distinguish a difference between a SBL near the surface and the residual layers above, as the aerosols may be evenly distributed. This may lead to overestimates of the BLH at night.

When the winds are westerly, the detected backscatter signals are generally much higher than those detected when winds are easterly. The aerosol content is relatively high, resulting in high backscatter values, which are seen to increase with wind speed and RH. Under these circumstances the vertical backscatter profile is easily distinguishable resulting in robust BLH detections. Dividing the BLH estimates in SW and NW clearly shows two separate distributions, especially during the autumn months. The division by temperature in May shows even more distinguishable frequency distributions. This approach of dividing the BLH estimates is not tried for the whole year as the sea surface temperature varies significantly over the course of a year and unstable conditions over the sea might be observed over a large temperature range during a whole year. The division of the yearly frequency distributions into winds from SW and NW shows very similar distributions and the mean BLH estimates for NW are only approximately 50 m higher. This small difference is observed since all seasons are 'put together' in one distribution. The NW and SW division does generally not show separate distributions during summer and winter months. The temperature difference between the sea surface and the atmosphere is much smaller during summer and winter, than that during autumn and spring.

#### Intra-annual variation

As the BLH estimates are divided into easterly and westerly winds, it is important to point out that the amount of estimates based on westerly winds far exceed the amount of estimates based on easterly winds. The high BLH estimates during the autumn months are as expected when the winds are from the west, due to the influence of the marine conditions, where sea surface temperatures are higher than the air temperature. The BLH estimates based on easterly winds show generally low heights during winter months, where days are shorter, and convective conditions are less frequently observed.

A similar intra-annual analysis was performed by Peña et al. (2013) with BLHs derived from both ceilometer observations and from simulations performed with the Weather Research and Forecasting model (WRF) in Høvsøre. The analysis was made on the westerly wind sector only and shows similar curves to the green curves in Figure 55. Both the WRF and ceilometer analysis found a highest mean BLH in November 2010 and the lowest in June 2010, though the mean BLHs are somewhat higher than those found in this analysis.

# 7 Conclusion

The cloud filtering provides a clear improvement when estimating the BLH with the four applied methods and may easily be implemented in an automated BLH detection algorithm. As the cloud filtering methods may be chosen according to different cloud conditions or BLH definitions, they provide flexibility in BLH detection. The amount of usable data may be increased considerably by filtering clouds. In this analysis, $\sim$60% of the aerosol backscatter measurements during the year showed cloud cover, and many would have been discarded without the filtering methods applied.

Both of the BLH detection algorithms that have been modified in this work may provide better estimates of the BLH under certain conditions. The variable critical threshold value is easily implemented in an automated BLH detection algorithm. The larger the range in aerosol backscatter values for a given study, the larger is the benefit of implementing the modification. The exponent idealized method shows a notable improvement when aerosol concentrations are high near the surface. In this study this was often seen when there were strong winds from the west. As the method is computationally intense with the two additional parameters, it may therefore be dependent on the specific study whether the benefits of the modification outweigh the extra computational time.

The ceilometer may be used for analysis of the ABL structure and the daily evolution. The standard deviation of the 10 s BLH estimates is significantly larger when the aerosol backscatter signals are weak and generally more robust BLH estimations are performed when the signals are strong. The backscatter signals are seen to depend on the RH of the atmosphere, as this influences the aerosol size.

A significant correlation is found between the BLH estimations from the aerosol backscatter measurements with ceilometer data and BLH estimations based on turbulence measurements with the wind lidar. As both instruments are dependent on the aerosol content of the atmosphere, they only produce reliable measurements when aerosol concentration is above a critical value. This was often not the case when winds were easterly. It would therefore be interesting to compare the ceilometer-based BLH estimates with other methods than the minimum TKE, also as this method is not reliable in the presence of clouds. This comparison would also be relevant for further investigation of the cloud filtering methods, as no clear consensus on a definition of the CTBL exists.

For the first time frequency distributions of BLH estimates were made with a large data set with measurements from Høvsøre. It is noteworthy that no matter the method of estimation, the mean BLH and the shape of the distributions were relatively similar. This tells something about the robustness of the BLH detection algorithms. The monthly analysis of the marine BLH estimates often showed bi-modal distributions. It was possible to divide these monthly distributions into separate distributions by wind direction or air temperature criteria. Division of the marine BLH estimates into day and night showed similar distributions with the same mean BLH, as was expected. The monthly frequency distributions of BLH estimates with easterly winds showed more surprising results, as the distributions were seldom bi-modal. The division of the BLH estimates into day and night showed no consistent results, sometimes with a higher mean BLH during nighttime than daytime.

The wave patterns of the vertical backscatter profiles in the ceilometer data, mentioned in section 5.8 have not been filtered for this work. The patterns are not so dominant in the two profile fitting methods, but it may still be worthwhile to correct for these patterns in future analyses.

# A Appendix

## Abbreviations

| | |
|---|---|
| **ABL** | *Atmospheric Boundary Layer* |
| **BLH** | *Boundary Layer Height* |
| **CBL** | *Convective Boundary Layer* |
| **CI** | *Capping Inversion* |
| **CNR** | *Carrier to Noise Ratio* |
| **CTBL** | *Cloud Topped Boundary Layer* |
| **EZ** | *Entrainment Zone* |
| **EZT** | *Entrainment Zone Thickness* |
| **FA** | *Free Atmosphere* |
| **LIDAR** | *Light Detection and Ranging* |
| **NW** | *North West* |
| **ML** | *Mixed Layer* |
| **RH** | *Relative Humidity* |
| **RL** | *Residual Layer* |
| **RMSD** | *Root Mean Square Deviation* |
| **SE** | *South East* |
| **SBL** | *Stable Boundary Layer* |
| **SL** | *Surface Layer* |
| **SW** | *South West* |
| **TIBL** | *Thermal Internal Boundary Layer* |
| **TKE** | *Turbulence Kinetic Energy* |

# B Appendix

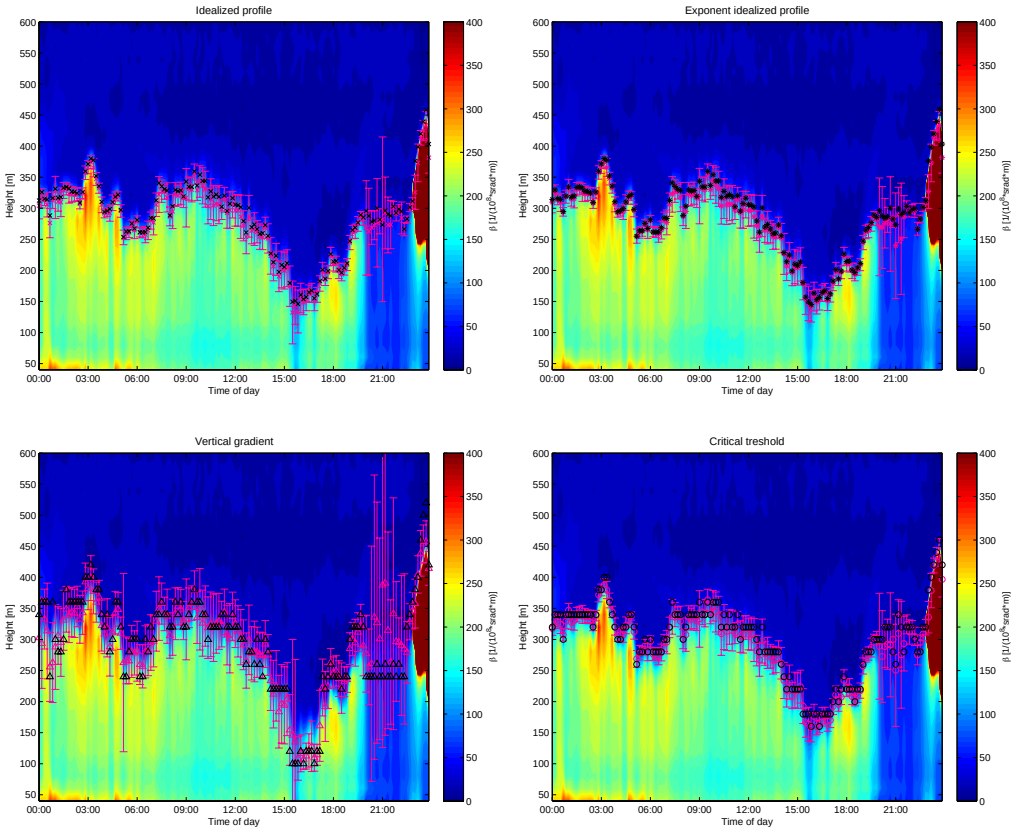


*Figure 56*: The diurnal evolution of the ABL on 21 June 2010 shown with four different BLH detections methods. Black symbols indicate the BLH estimates from the 10 min data and magenta symbols the BLH estimates from the 10 s mean BLH. The error bars represent the standard deviation of the 10 s estimates within 10 minutes.

# References


Batchvarova, E., X. Cai, S.-E. Gryning, and D. Steyn, 1999: Modelling the internal boundary layer in the lower fraser valley. *Boundary-Layer Meteorology*, **90**, 1–20.

Batchvarova, E. and S.-E. Gryning, 1991: Applied model for the growth of the daytime mixed layer. *Boundary-Layer Meteorology*, **56**, 261–274.

Betts, A. K., 1985: Mixing line analysis of clouds and cloudy boundary layers. *Journal of Atmospheric Science*, **42**, 2751–2763.

Cariou, J.-P. and M. Boquet, 2011: Leosphere pulsed lidar principles. Tech. Rep. Up-Wind Scientific Report WP6-D6.1.1, Risø National Laboratory, Roskilde, Denmark, *URL:www.upwind.eu*.

Cohn, S. A. and W. M. Angevine, 2000: Boundary layer height and entrainment zone thickness measured by lidars and wind-profiling radars. *Journal of Applied Meteorology*, **39**, 1233–1247.

Davis, K., D. H. Lenschow, S. P. Oncley, C. Kiemle, G. Ehret, A. Giez, and J. Mann, 1997: Role of entrainment in surface-atmosphere interactions over the boreal forest. *Journal of Geophysical Research*, **102**, 29 219–29 230.

Emeis, S., C. Münkel, S. Vogt, W. J. Müller, and K. Schäfer, 2004: Atmospheric boundary-layer structure from simultaneous SODAR, RASS, and ceilometer measurements. *Atmospheric Environment*, **38**, 273–286.

Emeis, S., K. Schäfer, and C. Münkel, 2008: Surface-based remote sensing of the mixing-layer height, a review. *Meteorologische Zeitschrift*, **17**.

Garratt, J., 1992: *The atmospheric boundary layer*. Cambridge atmospheric and space science series, Cambridge University Press.

Gill-Instruments, 2013: *Principle of operation*. Gill-Instruments, URL `www.gill.co.uk/products/anemometer/principleofoperation.htm`.

Grimsdell, A. W. and W. M. Angevine, 1998: Convective boundary layer height measurement with wind profilers and comparison to cloud base. *Journal of Atmospheric and Oceanic Technology*, **15**, 1331–1338.

Gryning, S.-E. and E. Batchvarova, 1994: Applied model for the growth of the daytime mixed layer. *Quarterly Journal of the Royal Meteorological Society*, **120**, 47–58.

Gryning, S.-E. and E. Batchvarova, 2002: Marine boundary-layer height estimated from the hirlam model. *Boreal Environment Research*, 229–233.

Hennemuth, B. and A. Lammert, 2006: Determination of the atmospheric boundary layer height from radiosonde and lidar backscatter. *Boundary-Layer Meteorology*, **120 (1)**, 181–200.

Hämeri, K., A. Laaksonen, M. Väkevä, and T. Suni, 2001: Hygroscopic growth of ultrafine sodium chloride particles. *Journal of Geophysical Research*, **106**, 20 749–20 757.

Høvsøre infofolder, 2013: *Velkommen til Høvsøre*. Nationallaboratoriet for bæredygtig energi.

Klaus, C., 2005: *Cloud types*. Argonne National Laboratory, URL `http://commons.wikimedia.org/wiki/File:Cloud_types.jpg`.

Klett, J., 1985: Lidar inversion with variable backscatter/extinction ratios. *Applied Optics*, **24**, 1638–1643.

Kreyszig, E., 1999: *Advanced Engineering Mathematics*. John Wiley and Sons.

Larsen, S., 2009: Microscale meteorology, lecture notes.

Leosphere, 2008: $Windcube^{TM}$ *Wind lidar system for wind measurement Product information*. Leosphere, LIDAR Environmental observations.

Leosphere User Manual, 2009: *Ez aerosol and cloud lidar ALS300 and ALS450*. Leosphere, LIDAR Environmental observations.

Liu, S. and X.-Z. Liang, 2010: Observed diurnal cycle climatology of planetary boundary layer height. *Journal of Climate*, **23**, 5790–5809.

Mann, J. and A. Peña, 2010: Lidar scanning of momentum flux in and above the atmospheric surface layer. *Journal of Atmospheric and Oceanic Technology*, **27**, 959?976.

Martucci, G., R. Matthey, and V. Mitev, 2007: Comparison between backscatter lidar and radiosonde measurements of the diurnal and nocturnal stratification in the lower troposphere. *Journal of Atmospheric and Oceanic Technology*, **24**, 1231–1244.

Martucci, G., R. Matthey, V. Mitev, and H. Richner, 2010: Frequency of boundary-layer-top fluctuations in convective and stable conditions using laser remote sensing. *Boundary-Layer Meteorology*, **135**, 313–331.

Metek, 2013a: *Ultrasonic Wind Sensor uSonic-3 Scientific*. Metek, URL [http://www.metek.de/product-details/usonic-3-scientific.html].

Metek, 2013b: *USA-1 Ultrasonic Anemometer*. Metek, URL www.deltatech.ch/up/ktml/files/produkte/METEK_USA1_EN.pdf.

Milroy, C., et al., 2012: An assessment of pseudo-operational ground-based light detection and ranging sensors to determine the boundary-layer structure in the coastal atmosphere. *Advances in Meteorology*, **2012**.

MySQL 5.1 Reference Manual, 2013: *What is MySQL?* Oracle, URL [http://dev.mysql.com/doc/refman/5.1/en/what-is-mysql.html].

Münkel, C., 2006: Boundary layer and air quality monitoring with a commercial lidar ceilometer. *Society of Photo-Optical Instrumentation Engineers (SPIE) Conference Series*, Vol. 6367.

Münkel, C., N. Eresmaa, J. Rasanen, and A. Karppinen, 2007: Retrieval of mixing height and dust concentration with lidar ceilometer. *Boundary-Layer Meteorology*, **124**, 117–128.

Obukhov, A., 1946: Turbulence in an atmosphere with a non-uniform temperature. *Boundary-Layer Meteorology*, **2 (1)**, 7–29, english translation, 1971.

Peña, A., S.-E. Gryning, and A. M. Hahmann, 2013: Observations of the atmospheric boundary-layer height under marine upstream flow conditions at a coastal site. *Journal of geophysical research: Atmospheres*, **118**, 1924–1940.

Peña, A., S. E. Gryning, and C. B. Hasager, 2010: Comparing mixing-length models of the diabatic wind profile over homogeneous terrain. *Theor. Appl. Climatol.*, **100**, 325–335.

Sathe, A., J. Mann, J. Gottschall, and M. S. Courtney, 2011: Can wind lidars measure turbulence? *Journal of Atmospheric and Oceanic Technology*, **28**, 853?868.

Schäfer, K., S. M. Emeis, A. Rauch, C. Münkel, and S. Vogt, 2004: Determination of mixing layer heights from ceilometer data. *Remote Sensing of Clouds and the Atmosphere IX*, **5571**, 248–259.

Seibert, P., F. Beyrich, S.-E. Gryning, S. Joffre, A. Rasmussen, and P. Tercier, 1998: Mixing height determination for dispersion modelling. *COST Action 710 – Final report*, B. E. A. Fisher, J. J. Erbrink, S. Finardi, P. Jeannet, S. Joffre, M. G. Morselli, U. Pechinger, P. Seibert, and D. J. Thompson, Eds., European Commission.

Sinclair, V. A., S. Niemelä, and M. Leskinen, 2012: Structure of a narrow cold front in the boundary layer: Observations versus model simulation. *Monthly Weather Review*, **140**, 2497–2519.

Steyn, D. G., M. Baldi, and R. M. Hoff, 1999: The detection of mixed layer depth and entrainment zone thickness from lidar backscatter profiles. *Journal of Atmospheric and Oceanic Technology*, **16**, 953–959.

Stull, R., 2006: The atmospheric boundary layer. *Atmospheric Science: An Introductory Survey*, J. M. Wallace and P. V. Hobbs, Eds., Elsevier Science, International Geophysics Series, 2d ed., 375–412.

Stull, R. B., 1988: *An introduction to boundary layer Meteorology*. Springer, 666 pp., reprinted in 2009.

Vaisala User's Guide, 2004: *Vaisala Ceilometer CL31*. Vaisala Oyj.

Vickers, D. and L. Mahrt, 2004: Evaluating formulations of stable boundary layer height. *Journal of Applied Meteorology*, **43**, 1736–1749.

Werner, C., 2005: Doppler wind lidar. *Lidar*, C. Weitkamp, Ed., Springer Series in Optical Sciences, Vol. 102.

Wilks, D. S., 2011: *Statistical methods in the atmospheric sciences*. Academic Press.

Wyngaard, J. C., 2010: *Turbulence in the atmosphere*. Cambridge University Press.